Die approbierte Originalversion dieser Dissertation ist in der Hauptbibliothek der Technischen Universität Wien aufgestellt und zugänglich.
http://www.ub.tuwien.ac.at

The approved original version of this thesis is available at the main library of the Vienna University of Technology.
http://www.ub.tuwien.ac.at/eng

DISSERTATION

Electronic and optical properties of graphene and large-scale graphene nanodevices

ausgeführt zum Zwecke der Erlangung des akademischen Grades einer
Doktorin der technischen Wissenschaften unter der Leitung von

O.Univ.-Prof. Dipl.-Phys. Dr.rer.nat. Joachim Burgdörfer
und
Univ. Ass. Dipl.-Ing. Dr. techn. Florian Libisch
Institut für Theoretische Physik, E136

eingereicht an der Technischen Universität Wien
Fakultät für Physik

von

MPhys. Larisa A. Chizhova
Matrikelnummer 0929561
Mosergasse 14/15
A-1090 Wien
larisa.chizhova@tuwien.ac.at

Wien, Oktober 2015

"It doesn't matter how beautiful your theory is, it doesn't matter how smart you are. If it doesn't agree with experiment, it's wrong."

Richard P. Feynman

TU WIEN

Abstract

Institute for Theoretical Physics

Electronic and optical properties of graphene and large-scale graphene nanodevices

by Larisa A. Chizhova

Graphene, a one-atom thin honeycomb lattice of carbon, has exceptional electronic properties making it a prime candidate for future electronic applications. However, graphene has no band gap which is essential for building logical circuits, and electronic transport is highly sensitive to the edge or (substrate-induced) bulk disorder reducing carrier mobility. In an attempt to overcome these issues, new substrates such as hexagonal boron nitride have proven to reduce the bulk disorder in graphene and even to open a small band gap of 40 meV. Although new substrates help to reduce bulk disorder, electronic transport is still affected by edge roughness and the surrounding chemical environment.

The thesis aims to simulate realistic graphene devices and to provide a theoretical study of several recent experiments performed with graphene. It addresses: (i) electron transport properties of graphene nanoconstrictions; (ii) electronic and optical properties of graphene on hexagonal boron nitride; and (iii) the nonlinear optical response of graphene. In particular, we predict that the conductance of small graphene nanodevices can probe the physics at the edges of the device by extracting the density of localized or trapped edge states from the conductance trace measurements. We also show that new substrates may modify the bandstructure of graphene by opening a small band gap and by creating mini-gaps above and below the Dirac cone. The density of states of graphene with an additional substrate potential in the magnetic field can be probed by optical magneto-spectroscopy. Furthermore, due to its linear energy dispersion, graphene demonstrates strong nonlinear response in the THz range highlighting its importance for building THz lasers and detectors. We also prove that graphene can form high-harmonic generation (HHG) spectra under the application of THz laser pulses similar to the HHG in gases.

TU WIEN

Kurzfassung

Institut für Theoretische Physik

Elektronische und optische Eigenschaften von Graphen und Graphen-Nanostructuren

von Larisa A. Chizhova

Graphen, eine Monolage von Kohlenstoffatomen mit der Gitterstruktur einer Bienenwabe, hat außergewöhnliche elektronische Eigenschaften, die es für zukünftiger Elektronikanwendungen sehr interessant machen. Allerdings hat Graphen keine Bandlücke, die für die Anwendung in logischen Schaltungen entscheidend ist. Elektronentransport durch Graphen ist sehr empfindlich gegenüber Defekten der Kristallstruktur am Rand und im Inneren der Monolage. Diese reduzieren die Mobilität der Elektronen. Neue Substate, wie hexagonales Bornitrid, reduzieren die Anzahl der Defekte im Inneren von Graphen und induzieren auch eine Bandlücke von etwa 40 meV. Verbesserte Probenqualität und optimierte Substrate verringern Defecte im Inneren. Daher dominieren nun Randdefekte den Elektronentransport.

Diese Arbeit zielt darauf ab, realistische Graphen-Nanostructuren zu simulieren und theoretische Studien aktueller Experimente mit Graphen bereitzustellen. Wir untersuchen: (i) Eigenschaften des Elektronentransports durch Graphennanodevices; (ii) elektronische und optische Eigenschaften von Graphen auf hexagonalem Bornitrid; und (iii) nicht-lineare optische Eigenschaften von Graphen. Insbesondere finden wir, dass die Leitfähigkeit von Graphennanostrukturen die Physik an den Rändern der Strukturen widerspiegelt. Durch Messung der Leitfähigkeit kann die Zustandsdichte lokalisierter Randzustände gefunden werden. Wir zeigen auch, dass neue Substrate die Bandstruktur von Graphen ändern können. Die Substrate führen zu einer kleinen Bandlücke am Diracpunkt und zu Mini-Bandlücken oberhalb und unterhalb des Diracpunkts. Die Zustandsdichte von Graphen im Magnetfeld mit einem zusätzlichen Substratpotenzial kann durch optische Magnetospektroskopie analysiert werden. Darüberhinaus zeigt Graphen starke nichtlineare Effekte im THz Bereich aufgrund seiner linearen Energiedispersion. Diese Eigenschaften haben eine große Bedeutung für den Bau von THz Lasern und Detektoren. Wir zeigen, dass Graphen unter Belichtung mit THz Laserpulsen high-harmonic (HHG) Strahlung bilden kann. Die HHG Spektren von Graphen ähneln deren in Gasen.

Contents

Abstract iii

Kurzfassung iv

List of Figures vii

Abbreviations ix

Physical Constants x

1 Introduction 2

2 Graphene 8
- 2.1 Graphene geometry and bandstructure . . . 8
- 2.2 Dirac equation . . . 10
- 2.3 Tight-Binding Hamiltonian . . . 13
- 2.4 Graphene nanoribbons . . . 15
  - 2.4.1 The spectrum of graphene nanoribbons . . . 19
  - 2.4.2 Graphene nanoribbons as infinite waveguides . . . 22
- 2.5 Graphene in a perpendicular magnetic field . . . 23
  - 2.5.1 Graphene nanoribbons in a perpendicular magnetic field . . . 25
- 2.6 Lattice Green's function and its application to the transport problem . . . 27
  - 2.6.1 Transport problem . . . 29
  - 2.6.2 Green's function of a system with attached contacts . . . 30
  - 2.6.3 Transmission coefficients . . . 32
- 2.7 Transition between Fermi energy and back gate voltage . . . 33
- 2.8 Fast Fourier transform on a graphene lattice . . . 34

3 Observation of size quantization in graphene nanodevices: transition to Landau levels 38
- 3.1 Quantum transport and size quantization in nanoribbons and quantum point contacts . . . 39
- 3.2 Experimental evidence of the size quantization in graphene quantum point contacts . . . 43
  - 3.2.1 Localized edge states in QPC . . . 45
  - 3.2.2 Size quantization in QPC . . . 46

3.3 Quantum transport in graphene nanoribbons in the presence of a perpendicular magnetic field . . . 49
3.4 Graphene quantum point contact in the presence of a perpendicular magnetic field . . . 54

4 Graphene on hexagonal boron nitride 58
4.1 Graphene Model Hamiltonian . . . 60
4.2 Hofstadter Butterfly . . . 62
4.3 DOS and bandstructure simulations . . . 63
4.3.1 DOS of graphene on hBN: influence of disorder . . . 71
4.4 Magneto-optical response of graphene flakes . . . 72
4.4.1 Magneto-excitons in graphene flakes . . . 77
4.5 Commensurate to incommensurate transition . . . 82

5 Nonlinear optical response of graphene to a few cycles THz laser pulse 86
5.1 Classical motion of Dirac fermions in a laser field . . . 87
5.2 Time-dependent Dirac equation . . . 90
5.2.1 Single-electron currents in the TDDE . . . 91
5.2.2 Examples of single-electron currents . . . 94
5.3 Time-dependent tight-binding approximation . . . 97
5.3.1 Single-electron currents in the TDTB . . . 97
5.4 Simulation of the experiment: TDDE versus TDTB . . . 99
5.4.1 Influence of doping . . . 103
5.4.2 Influence of disorder . . . 105
5.5 High-harmonic generation in graphene . . . 108

6 Summary 117

A Windowed Fourier transform 123

B Short Iterative Lanczos propagator 124

Bibliography 126

Acknowledgements 134

List of Figures

2.1 Graphene lattice 9
2.2 Bandstructure of graphene 10
2.3 Bandstructure of graphene: tight-binding approximation 13
2.4 Graphene nanoribbons 16
2.5 Graphene nanoribbons: matrix elements 17
2.6 Bandstructure of graphene nanoribbons 21
2.7 Bandstructure of graphene nanoribbons in the perpendicular magnetic field 26
2.8 Cyclotron motion and local density of states of graphene in the presence of the magnetic field 27
2.9 Scattering problem 30
2.10 Fast Fourier transform on a graphene grid 36

3.1 Conductance of graphene and 2DEG quantum point contacts 41
3.2 Measured conductance through graphene quantum point contact 44
3.3 Calculated local density of states of a quantum point contact 46
3.4 Energy rescaling of the measured conductance 47
3.5 Fourier analysis of size quantization signatures 48
3.6 Finite bias and temperature dependence of quantized conductance 50
3.7 Magnetic field dependence of the size quantization in ZGNR 51
3.8 Magnetic field dependence of the size quantization in AGNR 52
3.9 Magnetic field dependence of the size quantization in graphene quantum point contacts 56

4.1 Moiré superlattice induced by graphene-hBN interaction 60
4.2 Bandstructure of graphene supercell with a moiré potential 64
4.3 Density of states of a large-scale graphene flake placed on top on hBN . . 66
4.4 Two-dimensional bandstructure of graphene supercell with an effective hBN potential 67
4.5 Calculated density of states versus measured magnetocapacitance 68
4.6 Two-dimensional bandstructure of graphene supercell with unrealistically large parameters of the moiré potential 69
4.7 Density of states of a large-scale graphene flake with unrealistically large parameters of the moiré potential 70
4.8 Example of eigenfunctions of graphene flake with hBN potential 71
4.9 Density of states of graphene flake with hBN potential and randomly distributed single vacancies 72
4.10 DOS and optical response of a pristine graphene flake 74
4.11 DOS and optical response of a graphene flake on top of hBN 76

4.12 Shift of optical absorption lines due to magneto-excitonic effect 79
4.13 Supercell potential for graphene on hBN accounting for the substrate-induced strain 83
4.14 Bandstructure of grpahene supercell with hBN potential: influence of strain 85

5.1 Schematic view of laser – graphene interaction 87
5.2 Schematic electron motion on the Dirac cone 92
5.3 Few cycle THz laser pulse 94
5.4 Examples of single-electron currents evaluated within TDDE 96
5.5 Eigenstates of a graphene flake and examples of single-electron currents evaluated within TDTB 97
5.6 Nonlinear far-field response: intraband response versus response evaluated within TDDE 100
5.7 Nonlinear far-field response: response evaluated within TDDE with a band gap versus TBTB 101
5.8 Evolution of the odd harmonics intensities with the laser field strength . . 102
5.9 Influence of finite doping on the harmonic spectra 103
5.10 Influence of short- and long-range disorder on the single-electron current . 106
5.11 Influence of short-range disorder on the integrated current 107
5.12 Influence of disorder on power spectrum of the nonlinear response of graphene 108
5.13 High-harmonic spectra of graphene 110
5.14 An example of trajectory producing the highest energy harmonics 112
5.15 Details of the high-harmonic spectra of graphene 113
5.16 High-harmonic spectra of graphene for different pulse parameters and Fermi velocity 116

6.1 Thesis summary 120

Abbreviations

GNR	**G**raphene **N**ano-**R**ibbon
ZGNR	**Z**igzag **G**raphene **N**ano-**R**ibbon
AGNR	**A**rmchair **G**raphene **N**ano-**R**ibbon
(L)DOS	(**L**ocal) **D**ensity **O**f **S**tates
hBN	**h**exagonal **B**oron **N**itride
DFT	**D**ensity **F**unctional **T**heory
L(S)DA	**L**ocal (**S**pin)-**D**ensity **A**pproximation
ARPES	**A**ngle-**R**esolved **P**hoto**E**mission **S**pectroscopy
STM	**S**canning **T**unneling **M**icroscopy
SEM	**S**canning **E**lectron **M**icroscopy
AFM	**A**tomic **F**orce **M**icroscopy
(1,2)DEG	**(1,2) D**imentional **E**lectron **G**as
CNP	**C**harge **N**eutrality **P**oint
QPC	**Q**uantum **P**oint **C**ontact
TRS	**T**ime **R**eversal **S**ymmetry
PCC	**P**erfectly **C**onducting **C**hannel
CVD	**C**hemical **V**apor **D**eposition
TDDE	**T**ime-**D**ependent **D**irac **E**quation
WFT	**W**indowed **F**ourier **T**ransform
TDTB	**T**ime-**D**ependent **T**ight-**B**inding
SIL	**S**hort **I**terative **L**anczos
HHG	**H**igh-**H**armonic **G**eneration
SHG	**S**econd-**H**armonic **G**eneration
ATI	**A**bove-**T**hreshold **I**onization

Physical Constants

Speed of Light	c	$=$	$2.99 \times 10^{8}\ \mathrm{ms}^{-\mathrm{S}}$
Charge of electron	$\lvert e \rvert$	$=$	$1.6 \times 10^{-19}\ \mathrm{C}$
Mass of electron	m_e	$=$	$9.109 \times 10^{-31}\ \mathrm{kg}$
Plank's constant	h	$=$	$6.63 \times 10^{-34}\ \mathrm{Js}$
	$\hbar = h/2\pi$	$=$	$1.055 \times 10^{-34}\ \mathrm{Js}$
Permittivity of free space	ϵ_0	$=$	$8.854 \times 10^{-12}\ \mathrm{Fm}^{-1}$
	$e/4\pi\epsilon_0$	$=$	$1.440\ \mathrm{V\ nm}$

Dedicated to my parents and Paul

Chapter 1

Introduction

Some decades ago people could not imagine that graphite, a material everyone uses to sketch, to write or to paint, would cause a breakthrough, establishing single-layer material science. In spite of the discovery of 0D fullerenes already in 1985 [1] and quasi-1D carbon nanotubes in 1991 [2][1], most scientists were certain that a 2D carbon material, i.e. a monolayer of graphite, cannot exist under ambient conditions and in fact should always fold into a nanotube. However, in the 2000s A. Geim and his team succeeded in finding stable monolayers of graphite: graphene. The technique they used, the micromechanical cleavage or the Scotch-tape method, was very well-known for removing the top most layers of a crystal before doing, for example, STM imaging of a surface. One day, instead of looking at the highly oriented graphite surface in STM, they looked at the Scotch-tape used in the surface preparation of the sample and found very thin graphite pieces [4]. The follow-up measurements of electronic properties of these thin films [5, 6] started a new era of science of monolayers.

Already the first series of experiments designed to investigate graphene demonstrated the unique behavior of electrons in this material [5, 6]. It was discovered that graphene is gapless and features a linear dispersion near the Fermi energy closely resembling a Dirac cone. As a result electrons in graphene have a constant group velocity and move across the layer at ”relativistic” speeds. With the progress in device fabrication, it is nowadays possible to achieve electron mobilities in graphene of the order of 10^6 cm^2/Vs [7, 8], which is much larger than electron mobilities in silicon used in modern computer technology. This makes graphene a very attractive candidate for building fast nanoelectronics. Moreover, its low dimensionality can help to improve the limit of Moore’s law: a prediction that the number of transistors on a computer chip should double every year increasing the efficiency of computer devices. Very soon we will approach a point, where further miniaturization of Si integrated circuits runs into the hard limit of atomic scale resolution, where quantum effects become important. Graphene is also expected to be an interesting material in terahertz optics and electronics: for building THz detectors [9] and THz lasers [10]. The state of the art THz technology experiences a limitation due to the so-called THz gap (0.1 to 10 THz) [11], i.e. efficient and practically usable (of a small size) detectors and emitters of THz radiation are still hard to find. The range of further possible applications of graphene is very broad. Besides being used in a new generation of faster and smaller electronic devices (single-electron transistors [12]), graphene is expected to be used in touch-screen devices, solar cells, conducting inks for printing electronics or 3D printing. The elastic properties of graphene allow for creation of flexible and non-brittle displays. Biomedical applications of graphene include drug delivery, cancer therapy, and new biosensors. New studies with novel ideas appear every day in journals, pre-prints, or proposals. More and more people become involved in graphene research in academia and industry.

---

[1] In fact, the first observation of carbon nanotubes (CNT) was made already in 1952 by Radushkevich and Lukyanovich [3], who published their work in the Journal of Physical Chemistry in Russian. But it was not untill the rediscovery of nanotubes in 1991 by Iijima [2] when the actual rise of the CNTs science begun.

There are several problems with graphene, though. It is a semimetal with no band gap and electronic transport is very sensitive to the device edges or bulk disorder. A band gap is essential for building transistors with large on/off ratio needed for logical circuts. In an attempt to overcome these issues, new graphene substrates were realized, such as hexagonal boron nitride (hBN), which proved to reduce bulk disorder [13, 14] and even to open a small band gap [15]. Graphene perfectly aligned on hBN features new physical properties as compared to the unaligned or pristine one. In particular, the periodic moiré pattern induced by the small lattice mismatch between the two materials influences the local density of states [16]. It creates satellite structures above and below the Dirac point observed in various experiments [16, 17]. In a magnetic field, the large periodicity ($\sim$ 14 nm) of the moiré superlattice allows for observation of the Hofstadter butterfly: a fractal structure emerging as a result of the competition between two electron length scales determined by the superlattice size and by the size of the magnetically confined electronic state. The observation of these phenomena in conventional crystals with small unit cells is not possible as it would require inaccessibly large magnetic fields. The large size of the moiré supercell, however, lowers the required value of the magnetic field to about 20 T, which allows for the observation of the Hofstadter butterfly in graphene on hBN [18, 19].

Although graphene is predicted to have exceptional nonlinear properties in the THz range which can be used to overcome the THz gap, the nonlinear response of a single layer is very difficult to measure. The problem here is that a graphene monolayer absorbs only 2.3 % of light [20], which is remarkably large for a single layer but very little for the experimental detection of its response. Nevertheless, in an experiment with 45-layer graphene [21], a clear trace of nonlinear harmonics (third and fifth) was detected. In nonlinear optics with gases [22–24] and other solid materials, for example ZiO or GaSe [25, 26], an important question is the spectral range accessible by harmonic radiation, i.e. what is the upper cut-off of the harmonic spectra. However, no prediction on the high-harmonic generation spectra has been given for graphene.

In this thesis we theoretically address several fundamental questions of the physics of graphene we briefly sketched above. In particular, we predict that the measured conductance of small graphene nanodevices [27] can be a tool for probing the physics at the device edges by extracting the density of localized or trapped edge states from conductance trace measurements. The nature of the moiré induced satellites and the Landau level spectra of graphene on hBN is another topic of this thesis. We compare our theoretical results to the density of states probed by addition spectroscopy as function of back gate voltage [18] and to the magneto-optical absorption spectra [15]. We also theoretically discuss the measured nonlinear response of graphene [21] to short THz laser pulses.

Outline

This thesis is organized as follows. In chapter 2 we introduce graphene and its main properties. We discuss the peculiarities of solving the Dirac equation and the Schrödinger equation within the third-nearest-neighbor tight-binding approach to approximate the behavior of graphene in various physical problems. We briefly discuss the Green's function formalism used for calculation of the transport properties of large-scale graphene nanostructures and of the local density of states.

Chapter 3, 4 and 5 contain the main results of the thesis and include applications of the method described in chapter 2. In chapter 3 we examine the transport properties of graphene quantum point contacts (QPC) based on the experimental investigations by Terrés et al. [27]. The measured conductance exhibit signatures of size quantization, which we discuss in detail.

In chapter 4 we examine the change in the density of states of graphene alligned on hBN and, therefore, featuring the periodic moré patterns. In particular, we observe the formation of satellites and study their evolution with the magnetic field; we also observe a Hofstadter butterfly on top of each Landau level; and we develop a way to directly compare our results obtained as a function of Fermi energy with experiment, where the DOS was measured as a function of back gate voltage. We also show that magneto-optical absorption measurements can be a complementary tool for probing the energy dependence of the various structures in the density of states.

In the last chapter 5 we provide a study of the nonlinear optical response of graphene. We calculate the nonlinear harmonic generation in graphene due to the laser field by solving the time-dependent Dirac equation and Schrödinger equation within the tight-binding approximation. Our observations are in a good agreement with experiment [21]. We also discuss the role of doping and disorder on the low-energy harmonics as well as the behaviour of the high energy harmonics and their origin.

We conclude with a summary of the presented results and point to future extensions of this work.

Several results of this thesis have in part been published or are in the preparation process of being published.

Transport in graphene quantum point contacts (chapter 3)

1. B. Terres, L.A. Chizhova, F. Libisch, D. Jörger, S. Engels, A. Girschik, K. Watanabe, T. Taniguchi, S.V. Rotkin, J. Burgdörfer, and C. Stampfer.
   Size quantization of Dirac fermions in graphene quantum point contacts
   submitted to Nature Communications.

Graphene quantum dots on hexagonal boron nitride (chapter 4)

1. L.A. Chizhova, F. Libisch, and J. Burgdörfer.
   Graphene quantum dot on boron nitride: Dirac cone replica and Hofstadter butterfly
   Phys. Rev. B **90**, 165404 (2014).
2. L.A. Chizhova, J. Burgdörfer, and F. Libisch.
   Magneto-optical response of graphene: probing substrate interactions
   Phys. Rev. B **92**, 125411 (2015).

Nonlinear response of graphene (chapter 5)

1. L.A. Chizhova, F. Libisch, and J. Burgdörfer.
   Nonlinear response of graphene to a few cycle THz laser pulse: role of doping and disorder
   in preparation.

Other topics

1. L.A. Chizhova, S. Rotter, T. Jenke, G. Cronenberg, P. Geltenbort, G. Wautischer, H. Filter, H. Abele, and J. Burgdörfer
   Vectorial velocity filter for ultracold neutrons based on a surface-disordered mirror system
   Phys. Rev. E **89**, 032907 (2014).

2. T. Jenke, G. Cronenberg, J. Burgdörfer, L.A. Chizhova, P. Geltenbort, A.N. Ivanov, T. Lauer, T. Lins, S. Rotter, H. Saul, U. Schmidt, and H. Abele
   Gravity Resonance Spectroscopy Constrains Dark Energy and Dark Matter Scenarios
   Phys. Rev. Lett. **112**, 151105 (2014).

Chapter 2

Graphene

After its first experimental realization a decade ago and a milestone paper by K. Novoselov and A. Geim [5], graphene still keeps researchers' attention in different areas ranging from nanoelectronics and optics to biophysics and medicine. The first reported atomically thin graphitic films [5] were stable and highly conductive at ambient conditions with a reported room temperature mobility of 10^5 cm^2 /Vs, which is approximately two hundred times that of silicon widely used in computer technology. It was later demonstrated that the charge carriers in graphene closely resemble two-dimensional massless Dirac fermions [6]. This unique behavior of charge carriers led to the observation of unique electronic and optical properties: Klein tunneling, weak antilocalization, observation of Dirac Landau levels, unconventional integer and fractional quantum Hall effects, a nonlinear optical response to THz fields, etc.

Besides the considerable academic interest in graphene, also the IT companies (e.g., Samsung, LG Electronics, Apple etc) have joined in trying to transform fundamental studies to technological applications.

In this introductory chapter we discuss: (1) the main properties of graphene and graphene nanoribbons; (2) the theoretical description of graphene using the Dirac equation and the tight-binding approximation; and (3) theoretical aspects of the electron transport and the scattering problem in graphene nanodevices.

2.1 Graphene geometry and bandstructure

The carbon atoms in graphene form a honeycomb lattice (or interleaved trigonal lattices) with a unit cell containing two atoms, which form two so-called A and B sublattices.

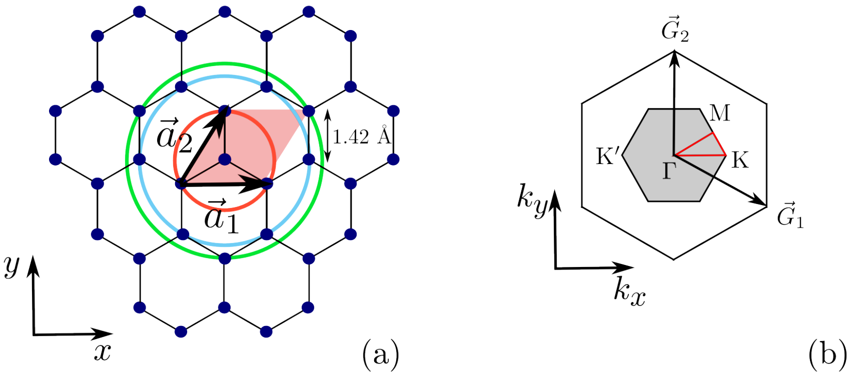

FIGURE 2.1: (a) Hexagonal lattice of graphene with lattice vectors $\vec{a}_1$ and $\vec{a}_2$. Red area shows a unit cell with two carbon atoms. The carbon-carbon distance is 1.42 Å. Atoms lying on the orange, blue and green circles correspond to the position of 1st, 2nd and 3rd nearest neighbors for an atom in the middle. (b) Reciprocal lattice of graphene with lattice vectors $\vec{G}_1$ and $\vec{G}_2$. Gray area displays the first Brillouin zone. The Dirac cones appear at the corners of the hexagonal Brillouin zone, i.e. at the Dirac points K and K'. Red trace show a path Γ-K-M-Γ used for bandstructure calculations.

The lattice vectors are [Fig.2.1(a)]

$$\vec{a}_1 = a(\sqrt{3}, 0), \;\; \vec{a}_2 = \frac{a}{2}(\sqrt{3}, 3), \tag{2.1}$$

where $a \approx 1.42$ Å is the carbon-carbon distance. The reciprocal lattice is also hexagonal with the lattice vectors [Fig.2.1(b)]:

$$\vec{G}_1 = \frac{2\pi}{3a}(\sqrt{3}, -1), \;\; \vec{G}_2 = \frac{2\pi}{3a}(0, 2). \tag{2.2}$$

The graphene Brillouin zone [shown as gray area in Fig.2.1(b)] has two special non-equivalent points K and K' at the corners which are called Dirac points. Near these points two bands with p_z-like character cross [Fig.2.2(a) bold curves] exactly at the Fermi energy in undoped graphene. This makes the material a semimetal. We have calculated the bandstructure [Fig.2.2(a)] using density functional theory (DFT) within the local density approximation (LDA) along the path Γ-K-M-Γ [see red trace in Fig.2.1(b)]. The energy dispersion of electrons near the Fermi energy ($E_F = 0$) can be approximated by a double cone structure [Fig.2.2(b)] which is similar to the solution of the massless Dirac equation

$$E_K = \pm v_F |\vec{k}|, \tag{2.3}$$

where v_F is the Fermi velocity. The particles in graphene, therefore, move with a constant velocity independent of their energy. The numerical value of v_F, which is about 10^6 m/s, can slightly vary in different systems depending on the substrate graphene is placed on [15, 28]. Moreover, it was observed that many-body interactions can effectively "reshape" the Dirac cone in suspended graphene leading to a varying Fermi velocity as

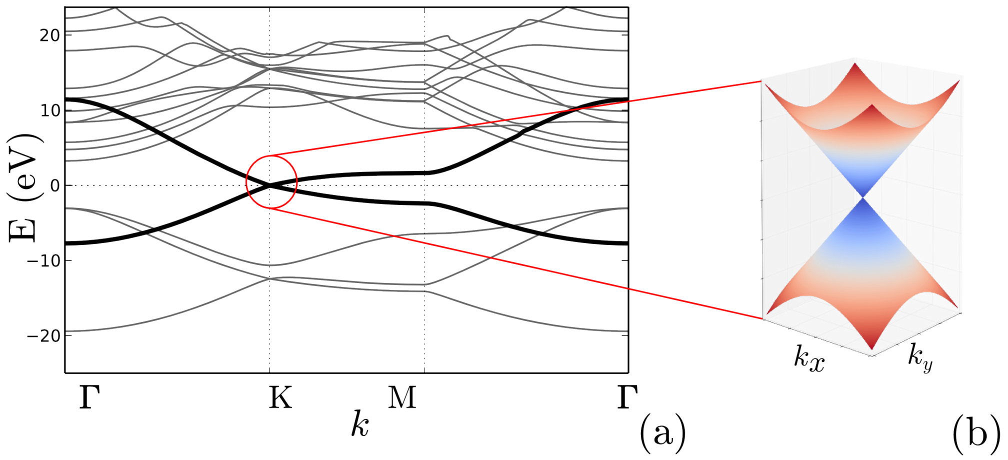

FIGURE 2.2: (a) Bandstructure of graphene calculated using density functional theory in the local density approximation (using ABINIT-LDA package). Bold lines correspond to the states with p_z-like character crossing at the Dirac point exactly at the Fermi energy ($E_F = 0$). These states, thus, determine the electronic properties of graphene. (b) Low-energy approximation to the bandstructure near the K and K' points corresponding to the solution of the massless Dirac equation, so-called double-cone dispersion.

function of charge carrier density close to the Dirac point [29]. We, however, neglect this effect and consider a constant Fermi velocity.

2.2 Dirac equation

To describe the electronic properties of graphene we first discuss a continuous low-energy approximation in terms of an effective massless Dirac Hamiltonian [30, 31]

$$H_D = v_F \begin{pmatrix} 0 & \hat{p}_x - i\hat{p}_y \\ \hat{p}_x + i\hat{p}_y & 0 \end{pmatrix} = v_F \left(\hat{p}_x \sigma_x + \hat{p}_y \sigma_y\right) = v_F \hat{\vec{p}} \cdot \vec{\sigma}, \tag{2.4}$$

where $\sigma_{x,y}$ are Pauli matrices acting on the spinor (ψ_A, ψ_B) related to the sublattice degree of freedom, the so-called pseudospin. Although pristine graphene is gapless, the interaction with a substrate can, in general, lead to a band gap at the Dirac point. For example, the interaction of graphene with a hexagonal boron nitride substrate, which we discuss extensively in chapter 4, produces a bandgap of the order of several meV. The gap opening can be described by an additional σ_z term, which is proportional to a non-zero mass m acquired by the Dirac electrons in the interacting system. In this case the stationary Dirac equation is

$$v_F \begin{pmatrix} mv_F & pe^{-i\theta_{\vec{p}}} \\ pe^{i\theta_{\vec{p}}} & -mv_F \end{pmatrix} \psi(\vec{p}) = E\psi(\vec{p}), \tag{2.5}$$

and band gap is $E_g = 2mv_F^2$. Here we eliminate the spatial degrees of freedom by using a Bloch ansatz $\psi = \psi(\vec{p})e^{i\vec{r}\vec{p}/\hbar}$, and we introduce a directional angle of momentum, $\theta_{\vec{p}}$, satisfying the equation: $\theta_{\vec{p}} = \arctan(p_x/p_y)$. The Dirac equation [Eq.(2.5)] provides two solutions $E = \pm v_F\sqrt{\Delta^2 + p^2}$ for the conduction (+) and valence (-) bands where we used the notation $\Delta = mv_F$. The particle momentum in a band with index $\xi = \pm 1$ is $p_\xi = \xi\sqrt{\Delta^2 + p^2}$. We search for the solution $\psi(\vec{p})$ of the Dirac equation [Eq.(2.5)] in the following form:

$$\psi(\vec{p}) = \begin{pmatrix} a(\vec{p}) \\ b(\vec{p}) \end{pmatrix}. \tag{2.6}$$

We then rewrite Eq.(2.5) as a system of equations for the spinor components $a(\vec{p})$ and $b(\vec{p})$ for each index ξ:

$$\begin{cases} pe^{-i\theta_{\vec{p}}}b_\xi(\vec{p}) & = (p_\xi - \Delta)\, a_\xi(\vec{p}), \\ pe^{i\theta_{\vec{p}}}a_\xi(\vec{p}) & = (p_\xi + \Delta)\, b_\xi(\vec{p}). \end{cases} \tag{2.7}$$

From the first equation we obtain

$$a_\xi(\vec{p}) = \frac{p}{p_\xi - \Delta} e^{-i\theta_{\vec{p}}} b_\xi(\vec{p}), \tag{2.8}$$

and, therefore, the solution of the Dirac equation [Eq.(2.5)] is

$$\psi_\xi(\vec{p}) = C_\xi(\vec{p}) \begin{pmatrix} \frac{p}{p_\xi - \Delta} e^{-i\theta_{\vec{p}}/2} \\ e^{-i\theta_{\vec{p}}/2} \end{pmatrix}, \tag{2.9}$$

where $C_\xi(\vec{p})$ can be found from the normalization of the wave function

$$C_\xi = \sqrt{\frac{p_\xi - \Delta}{2p_\xi}}. \tag{2.10}$$

As a results the wave function in momentum space is

$$\psi_\xi(\vec{p}) = \sqrt{\frac{p_\xi - \Delta}{2p_\xi}} \begin{pmatrix} \frac{p}{p_\xi - \Delta} e^{-i\theta_{\vec{p}}/2} \\ e^{i\theta_{\vec{p}}/2} \end{pmatrix}. \tag{2.11}$$

From this general solution it is easy to obtain the solution for massless Dirac fermions by setting $\Delta = mv_F = 0$, which is a good approximation for graphene with no band gap. In this case the wave function is

$$\psi_\xi(\vec{p}) = \frac{1}{\sqrt{2}} \begin{pmatrix} e^{-i\theta_{\vec{p}}/2} \\ \xi e^{i\theta_{\vec{p}}/2} \end{pmatrix}, \tag{2.12}$$

where $\xi = \pm 1$ corresponds to two energy branches $E = \pm v_F|\vec{p}| = \pm\hbar v_F|\vec{k}|$ for conduction and valence electrons. Interestingly, the state ψ_ξ is an eigenstates of a helicity operator $\hat{h} = \sigma \cdot \hat{\vec{p}}/|\vec{p}|$ [30], which projects the pseudospin onto the direction of the particle momentum $\vec{p}$:

$$\hat{h}\psi_\xi = \xi\psi_\xi. \tag{2.13}$$

The eigenvalues of the operator, equal to $\xi = \pm 1$, imply that the pseudospin is oriented along or against the direction of $\vec{p}$. In the Dirac approximation the helicity (or chirality) is a good quantum number which, in general, prevents backscattering and leads to Klein tunneling [30, 32] - the unhindered transmission of relativistic particles through a potential barrier for a wide range of incident angles. The helicity is well defined only within the Dirac approximation. Any deviations of the bandstructure from the ideal Dirac cone would destroy it.

The Dirac equation, however, is a low energy approximation and valid only in the vicinity of the Dirac points K or K'. The non-equivalent cones (valleys) located at K and K' create an additional K-K' degeneracy. This allows us to present the wave function near the Fermi energy as a four-component spinor $|\psi\rangle = (\psi_A^{(K)}, \psi_B^{(K)}, \psi_A^{(K')}, \psi_B^{(K')})$, which accounts for both valleys. For a four-component spinor the Dirac equation reads:

$$H_D = v_F \left(\hat{\vec{p}} \cdot \vec{\sigma}\right) \otimes \tau_1 + v_F \left(\hat{\vec{p}} \cdot \vec{\sigma}^*\right) \otimes \tau_2, \tag{2.14}$$

where $\tau_{1,2} = (\tau_0 \pm \tau_z)/2$ and $\tau_{0,x,y,z}$ are Pauli matrices acting on the K-K' degree of freedom. If there is no interaction between the K and K', the valley degree of freedom is separable and we can write a wave function in momentum space for each valley similar to [Eq.(2.12)] as

$$\psi_{\xi,\vec{K}}(\vec{k}) = \frac{1}{\sqrt{2}} \begin{pmatrix} e^{-i\theta_{\vec{k}}/2} \\ \xi e^{i\theta_{\vec{k}}/2} \end{pmatrix}, \quad \psi_{\xi,\vec{K}'}(\vec{k}) = \frac{1}{\sqrt{2}} \begin{pmatrix} e^{i\theta_{\vec{k}}/2} \\ \xi e^{-i\theta_{\vec{k}}/2} \end{pmatrix} \tag{2.15}$$

with the corresponding Dirac energy dispersion near each independent cone $E_{K,K'} = \xi\hbar v_F|\vec{k}|$ [30, 31]. As a result, the total four-component spinor wave function is

$$|\psi_\xi\rangle = |\psi_{\xi,\vec{K}}\rangle \otimes |\psi_{\xi,\vec{K}'}\rangle. \tag{2.16}$$

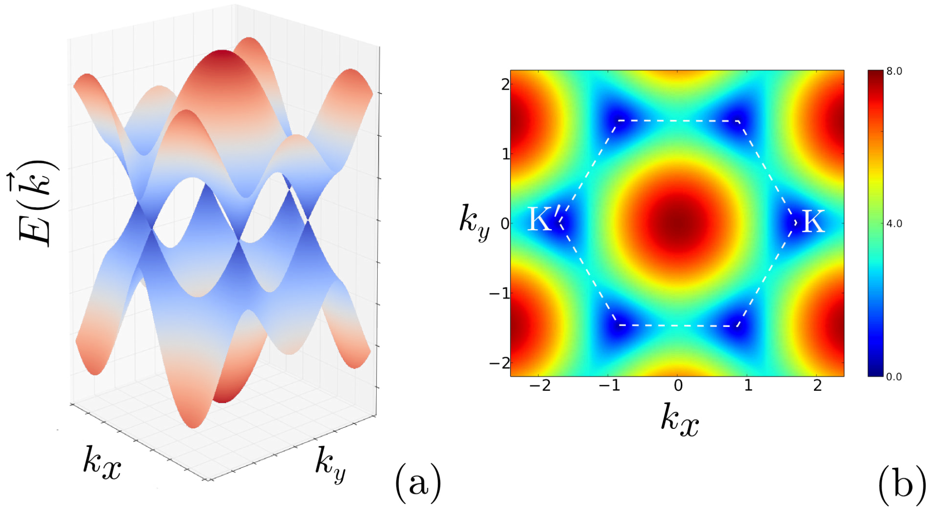

FIGURE 2.3: (a) Bandstructure of graphene calculated using tight-binding approximation [33] (b) The colormap of the upper band reveals the hexagonal symmetry with minima corresponding to the Dirac points at K and K' as well as trigonal distortion of each Dirac cone, the trigonal warping.

The analytical solution of the massless (and massive) Dirac equation is very useful in many cases and is often used to approximate the physics of graphene.

2.3 Tight-Binding Hamiltonian

The Dirac equation approximates the graphene bandstructure near the K and K' points only in the low-energy limit (up to $|E| \approx 0.5$ eV). At higher energies the double-cone bandstructure does not account for the trigonal deformation of the circular cross-section of the cones called trigonal warping, for the electron-hole asymmetry and for the connection between the K and K' cones at even higher energies present in graphene. In this chapter we briefly discuss the tight-binding approximation, which allows us to capture these bandstructure deformations to some extent. Due to the sp^2 hybridization of carbon atoms in graphene the electron transport and electronic structure of graphene near the Fermi energy is determined by the p_z carbon orbitals. Within the tight-binding description this means that it is sufficient to consider only the p_z orbital centered at each carbon atom. The tight-binding Hamiltonian which includes interaction between the nearest-neighbor atoms reads

$$H = \epsilon_0 a_i^\dagger a_i + t_1 a_i^\dagger b_i, \tag{2.17}$$

where ϵ_0 is the on-site energy t_1 is the hopping amplitude between neighboring atoms, $a_i/a_i^\dagger$ ($b_i/b_i^\dagger$) is annihilation/creation operator on site i of sublattice A (B). The calculated bandstructure within the first nearest-neighbor tight-binding approximation clearly displays a hexagonal Brillouin zone with two inequivalent cones and trigonal warping [Fig.2.3(a,b)]. However, to account for the electron-hole asymmetry it is necessary to include overlap integrals between higher order neighbors. This provides a better approximation, since the p_z orbital is delocalized over the graphene hexagon leading to significant interactions with more remote neighbors. The tight-binding Hamiltonian which includes hopping up to third nearest neighbor reads

$$H = \epsilon_0 a_i^\dagger a_i + t_1 a_i^\dagger b_i + t_2 \sum a_i^\dagger a_{i+1} + t_3 \sum a_i^\dagger b_{i+1}, \tag{2.18}$$

where t_2 and t_3 are the hopping amplitudes between second and third neighbors [for the position of 1^{st}, 2^{nd} and 3^{rd} nearest neighbors see Fig.2.1(a)]. The hopping parameters represent the interaction between the adjacent sites and are extracted from a fit of the resulting tight-binding bandstructure to the DFT-LDA calculations [34]. Throughout the thesis we use the following tight-binding parameters (if not explicitly stated otherwise):

$$\epsilon_0 = -0.126 \text{ eV}, \; t_1 = -3.145 \text{ eV}, \; t_2 = -0.042 \text{ eV}, \; t_3 = -0.35 \text{ eV}.$$

These tight-binding parameters produce a cone-like dispersion with a Fermi velocity $v_F^0 = 0.78 \cdot 10^6$ m/s, which is slightly smaller than the values measured in experiments. For instance, angle-resolved photoemission spectroscopy (ARPES) [35], magneto-transport measurements [36], scanning tunneling microscopy (STM) [37], and cyclotron resonance studies [38] give Fermi velocities ranging from $v_F^{\text{exp}} \approx 1.0 \cdot 10^6$ m/s to $1.1 \cdot 10^6$ m/s. This enhanced values of the velocity is due to many-body effects, such as nonlocal electron-electron and electron-phonon interactions, which are missing in LDA [39].

The tight-binding approach is very efficient for simulating electronic transport or for calculating optical response of graphene nanostructures and nanodevices, such as graphene flakes, graphene ribbons, graphene quantum point contacts. The size of the Hamiltonian matrix [Eq.(2.18)] is N×N, where N is the total number of atoms in the nanodevice. This matrix is sparse which enables us to calculate the electronic and optical properties for nanostructures with up to 10^7 atoms.

To illustrate how to create the Hamiltonian matrix [in Eq.(2.18)] for finite size structures, let us consider a piece of a honeycomb lattice or a graphene quantum dot [Fig.2.4(a)]. The dot can be assembled by a repetition of supercells [outlined by a red box in Fig.2.4(a)]. Such a building block, i.e. a supercell, creates a small piece of a matrix which we will call H_0. The elements of this matrix $H_0[i,j]$ correspond to the tight-binding parameters between two atoms i and j within the supercell. The interaction between the supercell and its neighboring supercell to the right [outlined by a red dashed box in Fig.2.4(a)] is described by the matrix H_I (or $H_I^\dagger$ for its neighboring supercell to the left). The matrix element $H_I[i,j]$ is equal to the tight-binding parameter between the atom i of the supercell and the atom j of its neighboring supercell. The full Hamiltonian matrix for any nanostructure has a block-diagonal form consisting of repeating blocks of H_0, H_I and $H_I^\dagger$:

$$H = \begin{pmatrix} \ddots & & & & & & & \\ & H_0 & H_I & 0 & 0 & 0 & 0 & \\ & H_I^\dagger & H_0 & H_I & 0 & 0 & 0 & \\ & 0 & H_I^\dagger & H_0 & H_I & 0 & 0 & \\ & 0 & 0 & H_I^\dagger & H_0 & H_I & 0 & \\ & 0 & 0 & 0 & H_I^\dagger & H_0 & H_I & \\ & 0 & 0 & 0 & 0 & H_I^\dagger & H_0 & \\ & & & & & & & \ddots \end{pmatrix}. \tag{2.19}$$

The size of the matrix H_0 describing the supercell and that of the interaction matrix H_I between the adjacent cells is determined by the number of atoms N_y within the cell multiplied by the number of tight-binding orbitals per atom. One can generalize the problem even further by considering a nanostructure with nanoblocks of different size. In this case, the interaction matrix H_I is no longer quadratic, but has a size $\mathrm{N}_k \times \mathrm{N}_m$ with N_k and N_m atoms in the neighboring supercells k and m.

The diagonal elements of the matrix H are on-site energies related to each atom. Therefore, an additional spatially varying potential affects only the on-site energies and can be easily taken into account by adding this potential to the diagonal elements of the matrix H. Similarly, short-ranged disorder, such as single and double vacancies can be taken into account by adding large energy values to some diagonal elements of the matrix H corresponding to the positions of the missing atoms. Moreover, the tight-binding method allows for inclusion of strain or lattice deformations, which lead to the modification of the on-site and hopping parameters in the matrix H for the appropriate atoms.

2.4 Graphene nanoribbons

Repeating the supercell in Fig.2.4(a) ad infinitum creates an infinite graphene nanoribbon. The properties of the ribbon depend on the type of its edges: zigzag [see Fig.2.4(a)] or armchair [see Fig.2.4(b)]. In the experiment, however, the edge is often ill-defined. Its termination is neither zigzag nor armchair, as graphene is etched to the shape of the

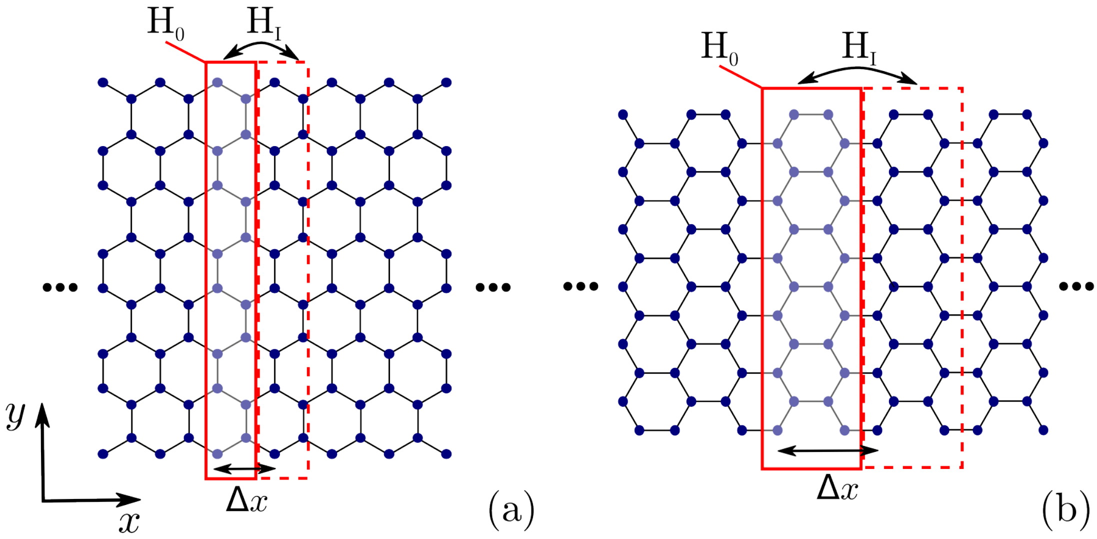

FIGURE 2.4: (a) A zigzag and (b) an armchair graphene nanoribbons with a unit cell outlined by red box and with a neighboring cell outlined by dashed red box. Each unit cell is described by H_0 matrix. The interaction between the adjacent unit cells is given by H_I.

ribbon in any arbitrary lattice direction. Because of the fabrication process, the edge also has a high amount of disorder. Nevertheless, general properties of nanoribbons can be found for the zigzag and armchair types. Moreover, it is expected that the advances in methods of fabrication of narrow graphene nanoribbons with atomically precise edges [40, 41] will allow for experimental investigation of the transport properties theoretically predicted for ideal ZGNRs and AGNRs in the near future.

Graphene nanoribbons (GNR) allows for investigating many phenomena of mesoscopic systems previously observed in 2D electron gases (2DEG): ballistic transport, size quantization, Coulomb blockade etc. GNRs are also promising for band gap engineering [42]. The band gap is required for building computer electronics, where one needs to account for two logical values, i.e. true/false, by being able to switch transistors on and off.

Using the notations introduced in section 2.3 zigzag graphene nanoribbons (ZGNR) have the following supercell [confined in red in Fig.2.4(a)] Hamiltonian

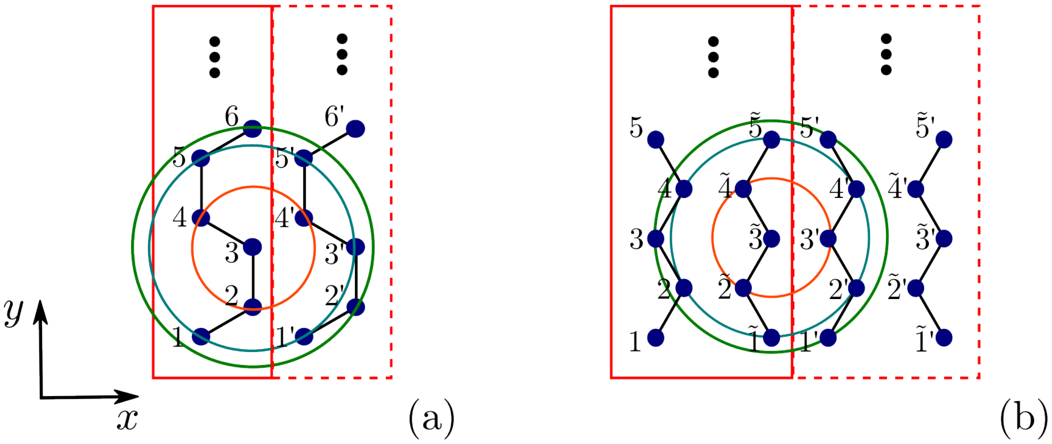

FIGURE 2.5: (a) Part of a zigzag and (b) part of an armchair graphene nanoribbon (GNR) shown in Fig.2.4 with a unit cell outlined by red box and with a neighboring cell outlined by dashed red box. An example of interaction of an atom a_3 for zigzag GNR and $a_{\tilde{3}}$ for armchair GNR with all neighboring atoms is demonstrated. The position of 1st, 2nd and 3rd nearest neighbors of a_3 and $a_{\tilde{3}}$ are depicted by the orange, blue and green circles.

$$H_0 = \left(\begin{array}{c|ccccccc} & a_1 & a_2 & a_3 & a_4 & a_5 & a_6 & \dots \\ \hline a_1 & \epsilon_0 & t_1 & t_2 & t_3 & 0 & 0 & \\ a_2 & t_1 & \epsilon_0 & t_1 & t_2 & 0 & 0 & \\ a_3 & t_2 & t_1 & \epsilon_0 & t_1 & t_2 & t_3 & \dots \\ a_4 & t_3 & t_2 & t_1 & \epsilon_0 & t_1 & t_2 & \\ a_5 & 0 & 0 & t_2 & t_1 & \epsilon_0 & t_1 & \\ a_6 & 0 & 0 & t_3 & t_2 & t_1 & \epsilon_0 & \\ \vdots & & & \vdots & & & & \ddots \end{array}\right) \tag{2.20}$$

and the following interaction Hamiltonian between adjacent supercells

$$H_I = \left(\begin{array}{c|ccccccc} & a'_1 & a'_2 & a'_3 & a'_4 & a'_5 & a'_6 & \dots \\ \hline a_1 & t_2 & 0 & 0 & 0 & 0 & 0 & \\ a_2 & t_1 & t_2 & t_3 & t_2 & 0 & 0 & \\ a_3 & t_2 & t_3 & t_2 & t_1 & t_2 & 0 & \dots \\ a_4 & 0 & 0 & 0 & t_2 & t_3 & 0 & \\ a_5 & 0 & 0 & 0 & t_3 & t_2 & 0 & \\ a_6 & 0 & 0 & 0 & t_2 & t_1 & t_2 & \\ \vdots & & & & & & & \ddots \end{array}\right). \tag{2.21}$$

Red boxes outline the matrix elements corresponding to the interaction of atom a_3 with all other atoms a_i in the unit cell and atoms a'_i of the neighboring unit cell [see also

Fig. 2.5(a) for the position of the atom a_3 and its nearest neighbors]. The nearest-neighbor terms are colored by orange, blue and green consistent with Fig. 2.5(a).

For armchair graphene nanoribbons (AGNR) the unit cell [shown in Fig.2.4(b)] consists of two carbon chains and has a size of $2N_y$. Each chain can be viewed separately, which means that both H_0 and H_I for AGNR have an additional block structure. For H_0 the two diagonal sub-matrices describe the chains themselves and off-diagonal sub-blocks describe the interaction between the chains. In the third-nearest-neighbor tight-binding approximation, the H_I matrix has only one off-diagonal matrix being non-zero, which is responsible for the interaction of the nearest-neighbor chains between the supercells. H_0 and H_I have the following forms:

$$H_0 = \left(\begin{array}{c|cccccc|cccccc}
 & a_1 & a_2 & a_3 & a_4 & a_5 & \dots & \tilde{a}_1 & \tilde{a}_2 & \tilde{a}_3 & \tilde{a}_4 & \tilde{a}_5 & \dots \\
\hline
a_1 & \epsilon_0 & t_1 & t_2 & 0 & 0 & & t_3 & t_2 & 0 & 0 & 0 & \\
a_2 & t_1 & \epsilon_0 & t_1 & t_2 & 0 & & t_2 & t_1 & t_2 & t_3 & 0 & \\
a_3 & t_2 & t_1 & \epsilon_0 & t_1 & t_2 & & 0 & t_2 & t_3 & t_2 & 0 & \\
a_4 & 0 & t_2 & t_1 & \epsilon_0 & t_1 & & 0 & t_3 & t_2 & t_1 & t_2 & \\
a_5 & 0 & 0 & t_2 & t_1 & \epsilon_0 & & 0 & 0 & 0 & t_2 & t_3 & \\
\vdots & & & & & & \ddots & & & \vdots & & & \ddots \\
\hline
\tilde{a}_1 & t_3 & t_2 & 0 & 0 & 0 & & \epsilon_0 & t_1 & t_2 & 0 & 0 & \\
\tilde{a}_2 & t_2 & t_1 & t_2 & t_3 & 0 & & t_1 & \epsilon_0 & t_1 & t_2 & 0 & \\
\tilde{a}_3 & 0 & t_2 & t_3 & t_2 & 0 & \dots & t_2 & t_1 & \epsilon_0 & t_1 & t_2 & \dots \\
\tilde{a}_4 & 0 & t_3 & t_2 & t_1 & t_2 & & 0 & t_2 & t_1 & \epsilon_0 & t_1 & \\
\tilde{a}_5 & 0 & 0 & 0 & t_2 & t_3 & & 0 & 0 & t_2 & t_1 & \epsilon_0 & \\
\vdots & & & & & & \ddots & & & \vdots & & & \ddots
\end{array}\right), \qquad (2.22)$$

$$H_I = \left(\begin{array}{c|cccccc|cccccc}
 & a'_1 & a'_2 & a'_3 & a'_4 & a'_5 & \dots & \tilde{a}'_1 & \tilde{a}'_2 & \tilde{a}'_3 & \tilde{a}'_4 & \tilde{a}'_5 & \dots \\
\hline
a_1 & & & & & & & & & & & & \\
a_2 & & & & & & & & & & & & \\
a_3 & & & & & & & & & & & & \\
a_4 & & & & & & & & & & & & \\
a_5 & & & & & 0 & & 0 & & & & & \\
\vdots & & & & & & & & & & & & \\
\hline
\tilde{a}_1 & t_1 & t_2 & t_3 & 0 & 0 & & & & & & & \\
\tilde{a}_2 & t_2 & t_3 & t_2 & 0 & 0 & & & & & & & \\
\tilde{a}_3 & t_3 & t_2 & t_1 & t_2 & t_3 & \dots & 0 & 0 & 0 & 0 & 0 & \dots \\
\tilde{a}_4 & 0 & 0 & t_2 & t_3 & t_2 & & & & & & & \\
\tilde{a}_5 & 0 & 0 & t_3 & t_2 & t_1 & & & & & & & \\
\vdots & & & & & & & & & & & & \ddots
\end{array}\right). \tag{2.23}$$

The block structure of the matrices is separated by vertical and horizontal lines in the center. The example of interaction between the atom $\tilde{a}_3$ in the left chain of the unit cell with all other atoms, i.e. with atoms a_i and $\tilde{a}_i$ in the same unit cell as well as with atoms a'_i and $\tilde{a}'_i$ in the neighboring unit cell, are outlined by red boxes and are illustrated in Fig. 2.5(b) similar to the ZGNR case.

2.4.1 The spectrum of graphene nanoribbons

For many applications it is necessary to know the energy spectrum (bandstructure) of infinitely extended graphene nanoribbons due to the presence of transverse confinement. In this case the spectrum in transverse direction y is discrete and consists of subbands with energies E_n. The electron energy of such a ribbon is given by the sum of the energy in longitudinal x-direction and the quantized energy due to the transverse confinement. An electron at the Fermi energy E_F traveling through the ribbon occupies only the allowed subbands below E_F and, therefore, acquires a discrete longitudinal momentum k_x^n according to the conservation of energy:

$$E_F = E_n + E(k_x^n) \tag{2.24}$$

Thus, the bandstructure $E(k_x)$ can be viewed as a set of cross-sections of the Dirac cone by E_n planes in k_y direction. To calculate the bandstructure of an infinite ribbon, we have to solve the Schrödinger equation $H|\psi\rangle = E|\psi\rangle$ with the Hamiltonian given by Eq.(2.19). The assumption of an infinite ribbon allows us to apply Bloch's theorem in the longitudinal x-direction:

$$|\psi\rangle = \begin{pmatrix} \vdots \\ |\psi_{j-1}\rangle \\ |\psi_j\rangle \\ |\psi_{j+1}\rangle \\ \vdots \end{pmatrix} = \begin{pmatrix} \vdots \\ e^{-ik_x \Delta x} \\ 1 \\ e^{ik_x \Delta x} \\ \vdots \end{pmatrix} |\chi\rangle \tag{2.25}$$

where Δx is the periodicity of the supercell, and $|\psi_j\rangle$ is the wave function within the j^{th} supercell. Inserting this ansatz into the Schrödinger equation gives rise to the following eigenvalue problem [34]:

$$\hat{H}_\chi |\chi\rangle = E|\chi\rangle, \tag{2.26a}$$

where

$$\hat{H}_\chi = H_0 + e^{ik_x \Delta x} H_I + e^{-ik_x \Delta x} H_I^\dagger. \tag{2.26b}$$

The solution of this eigenvalue problem for a given k_x allows us to obtain the bandstructure of the nanoribbon [Fig.(2.6)(a) and (b) for ZGNR and AGNR respectively]. The bandstructure of ZGNR has a band near $E = 0$ [outlined by a green box in Fig.(2.6)(a)], which correspond to edge states. This band is dispersionless within the first-nearest-neighbor tight-binding approximation which preserves electron-hole symmetry, but it acquires a nonzero curvature if interaction with more neighbors is considered. The edge states are absent for AGNR and its bandstructure reveals a band gap. We note parenthetically, that more detailed DFT calculations (within LSDA) show that the edge states of ZGNR have magnetic order with an antiferromagnetic ground state and a small band gap [43]. However, calculations based on the Hubbard model and experimental measurements of narrow zigzag ribbons showed a change of magnetic order (from antiferromagnetic to ferromagnetic) of the edges as a function of the ribbon width; and a semiconductor to metal transition was observed [44]. We do not account for edge magnetism within our single-particle picture as we are generally interested in large-scale systems with ill-defined edges, where the edge-induced magnetism is negligible.

An alternative approach to obtain the bandstructure of a nanoribbon is to solve the Dirac equation with the Hamiltonian defined in Eq.(2.4), including the additional confinement potential

$$V(y) = \begin{cases} \infty, & \text{if } y < 0 \text{ or } y > W \\ 0, & \text{if } 0 \leq y \leq W, \end{cases} \tag{2.27}$$

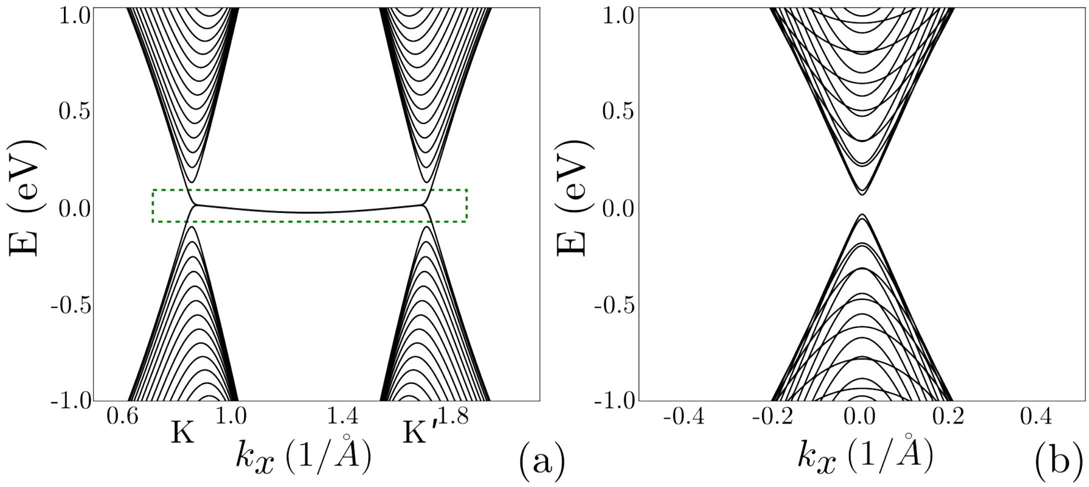

FIGURE 2.6: Bandstructure $E(k_x^n)$ of (a) a 22 nm wide zigzag graphene nanoribbon and of (b) a 12 nm wide armchair graphene nanoribbon. The subbands can be viewed as crossings of the Dirac cone by planes E_n corresponding to size quantization energies in k_y direction. The green dashed box highlights the dispersion of the edge states in the zigzag GNR.

where W is the width of the ribbon. In this case one can separate x and y variables and search for a wave function of the form:

$$\psi(\vec{r}) = e^{ik_x x} \begin{pmatrix} \phi_A(y) \\ \phi_B(y) \end{pmatrix}, \tag{2.28}$$

where $\phi_{A(B)}$ is a wave function defined on the A(B) sublattice. After substituting this wave function into the Dirac equation $H_D\psi(\vec{r}) = E\psi(\vec{r})$, one obtains the following system of equations:

$$\begin{cases} \left(k_x - \frac{\partial}{\partial y}\right) \phi_B(y) = \epsilon\phi_A(y) \\ \left(k_x + \frac{\partial}{\partial y}\right) \phi_A(y) = \epsilon\phi_B(y), \end{cases} \tag{2.29}$$

where $\epsilon = E/\hbar v_F$. Substituting the second equation into the first one, allows us to find ϕ_A and, consequently, ϕ_B:

$$\begin{aligned} \phi_A(y) &= C_1 e^{\lambda y} + C_2 e^{-\lambda y} \\ \phi_B(y) &= \frac{1}{\epsilon}\left((k_x + \lambda)\, C_1 e^{\lambda y} + (k_x - \lambda)\, C_2 e^{-\lambda y}\right), \end{aligned} \tag{2.30}$$

where $\lambda = \sqrt{k_x^2 - \epsilon^2}$, and $C_{1,2}$ are the constants of integration. To find the spectrum of a ribbon, i.e. $\epsilon(k_x)$, we apply the hard wall boundary conditions describing the edges. Considering a ZGNR of width W with an even number of atoms in the supercell [Fig.2.4(a)], which has A and B atoms terminating the opposite edges, the boundary conditions take the form: $\phi_A(y = W) = \phi'_A(y = W) = \phi_B(y = 0) = \phi'_B(y = 0) = 0$. Applying these boundary conditions lead to the following equation for the bandstructure [30]:

$$e^{-2\lambda W} = \frac{k_x - \lambda}{k_x + \lambda}. \tag{2.31}$$

Eq.(2.31) does not have an analytic solution and is solved numerically. However, the simple analytic solution exists for the case of $k_x = 0$, which is very useful for the quick estimate of the number of open modes in the transport problem, and yields:

$$E_n = \pm \frac{\hbar v_F \pi}{W} \left(n + \frac{1}{2} \right). \tag{2.32}$$

2.4.2 Graphene nanoribbons as infinite waveguides

In all transport calculations one requires the knowledge of the electronic states in the infinite waveguide, which serves as a contact or a lead. For example, in our numerical simulations infinite graphene nanoribbons of width W act as conducting contacts. To find electronic states in the waveguide with N_y atoms in y direction, we need to find k_x for the given electron (Fermi) energy E_F while solving Eq.(2.26), which we rewrite as

$$\beta (H_I^\dagger)^{-1} \left(E_F - H_0 \right) |\chi\rangle - (H_I^\dagger)^{-1} H_I |\chi\rangle = \beta^2 |\chi\rangle, \tag{2.33}$$

where $\beta = e^{-ik_x \Delta x}$. This equation can be solved by doubling the dimensions of the problem, i.e. by introducing a new vector $|\eta\rangle = \beta|\chi\rangle$ [34]:

$$\begin{cases} |\eta\rangle & = \beta|\chi\rangle \\ (H_I^\dagger)^{-1} \left(E_F - H_0 \right) |\eta\rangle - (H_I^\dagger)^{-1} H_I |\chi\rangle & = \beta|\chi\rangle, \end{cases} \tag{2.34}$$

which is a standard eigenvalue problem of the form $\hat{A}\vec{X} = a\vec{X}$. The solution gives $2N_y$ values of k_x^i, which can be separated into the right- and left-moving waves according to the sign of the group velocity:

$$\begin{aligned} v^i = \frac{\partial}{\partial k} \langle \chi^i | \hat{H}_\chi | \chi^i \rangle = \\ = i\Delta x \langle \chi^i | \left(H_I e^{ik_x^i \Delta x} + H_I^\dagger e^{-ik_x^i \Delta x} \right) | \chi^i \rangle. \end{aligned} \tag{2.35}$$

Real eigenvalues among $\{k_x^i\}$ correspond to propagating modes and imaginary eigenvalues correspond to exponentially decaying (or evanescent) modes.

Finding the open modes (or all possible k_x^i) in the lead for the electron energy E_F using Eq.(2.34) is possible only if the matrix $(H_I^\dagger)^{-1}$ exists. This requires that the matrix H_I is not degenerate, i.e. all eigenvalues of H_I are non-zero. This is true for ZGNR, but not for AGNR, where half of the eigenvalues are zero [see Eq.(2.23)]. Therefore, Eq.(2.34) can not be applied to AGNR. This problem, however, can be solved in two ways. (i) We can include interactions with the fourth and fifth nearest neighbors resulting in a non-degenerate matrix H_I. The drawback of the method is, however, the introduction of new elements into the sparse matrix, which brings us to stricter size limitations compared to ZGNR. (ii) Alternatively, still within the third-nearest-neighbor approximation we can rewrite Eq.(2.26) without multiplying by $(H_I^\dagger)^{-1}$ and acquire the new set of equations:

$$\begin{cases} |\eta\rangle & = \beta|\chi\rangle \\ (E_F - H_0)\,|\eta\rangle - H_I|\chi\rangle & = \beta H_I^\dagger|\chi\rangle, \end{cases} \tag{2.36}$$

which is a generalized eigenvalue problem $\hat{A}\vec{X} = a\hat{B}\vec{X}$. Its numerical solution does not pose any difficulty.

2.5 Graphene in a perpendicular magnetic field

In the presence of a homogeneous magnetic field $\vec{B} = \vec{\nabla} \times \vec{A}$ perpendicular to the graphene plane the Dirac Hamiltonian reads

$$H_D = v_F \begin{pmatrix} 0 & p_x - ip_y - e\vec{A} \\ p_x + ip_y - e\vec{A} & 0 \end{pmatrix} = v_F \vec{\sigma} \cdot \left(\hat{\vec{p}} - e\vec{A}\right). \tag{2.37}$$

Using the Landau gauge $\vec{A} = B(-y, 0)$ and the wave function of the form of Eq.(2.28) [30], the Dirac equation becomes

$$\begin{cases} \left(k_x - \frac{eB}{\hbar}y - \frac{\partial}{\partial y}\right)\phi_B(y) = \epsilon\phi_A(y) \\ \left(k_x - \frac{eB}{\hbar}y + \frac{\partial}{\partial y}\right)\phi_A(y) = \epsilon\phi_B(y), \end{cases} \tag{2.38}$$

here we use a notation $\epsilon = E/\hbar v_F$. The magnetic field gives rise to a new magnetic length scale $l_B = \sqrt{\hbar/eB} = 25.5/\sqrt{B[T]}$[nm]. Substituting the second equation into the first one gives

$$\frac{\partial^2\phi_A(y)}{\partial y^2} - \left(k_x - \frac{y}{l_B^2}\right)^2 \phi_A(y) + \epsilon^2\phi_A(y) = 0, \tag{2.39}$$

which is similar to the equation of a linear oscillator. The solution of this equation can be found by introducing a new variable $\xi = (\frac{y}{l_B} - l_B k_x)$ and a new energy $\epsilon^2 l_B^2 = 2N$ similar to the harmonic oscillator problem [45]. Therefore,

$$\epsilon_N = l_B\sqrt{2N}. \tag{2.40}$$

Consequently, the Landau level spectrum of Dirac fermions is [46]

$$E_N^D(B) = \operatorname{sgn}(N)\sqrt{2|e|\hbar v_F^2 |N| B}, \quad N \in Z_0, \tag{2.41}$$

This spectrum has three prominent features: (i) the existence of a 0^{th} Landau level ($N = 0$), which does not depend on the magnetic field; (ii) a square-root dependence of all $N \neq 0$ Landau levels on the magnetic field; and (iii) a graphene-specific degeneracy of the Landau levels due to the valley symmetry. The non-equidistant energy spacing provides a clear-cut distinction to the equidistant level spacing of non-relativistic Schrödinger electrons where the Landau level spectrum takes on the form of a harmonic oscillator [45] with the energy spectrum

$$E_N^S(B) = \hbar\omega_B(N + 1/2) \tag{2.42}$$

proportional to the cyclotron frequency $\omega_B = |e|B/m_e$. The Landau levels were experimentally observed in graphene in, for example, [47] and [36]. The wave functions of bulk graphene in the magnetic field are pseudospinors of the form [30, 48]

$$\Psi_{N,K} = \begin{pmatrix} \operatorname{sgn}(N)\psi_{|N|-1}(\xi) \\ \psi_{|N|}(\xi) \end{pmatrix}, \Psi_{N,K'} = \begin{pmatrix} \psi_{|N|}(\xi) \\ \operatorname{sgn}(N)\psi_{|N|-1}(\xi) \end{pmatrix}, \tag{2.43}$$

where $\psi_N(\xi) = 2^{-N/2}(N!)^{-1/2}\exp[-\xi^2/2]H_N(\xi)$ with Hermite polynomial $H_N(\xi)$ are the wave functions of a harmonic oscillator [30].

Any additional potential $\propto E_g\hat{\sigma}_z/2$ leading to the opening of a band gap E_g modifies the Landau levels Eq.(2.41) as

$$E_N^D(B) = \begin{cases} \operatorname{sgn}(N)\sqrt{2|e|\hbar v_F^2|N|B + (E_g/2)^2} & : N \neq 0, \\ \pm E_g/2 & : N = 0. \end{cases} \tag{2.44}$$

Consequently, for massive Dirac fermions [see section 2.2] the valley degeneracy of the zeroth Landau level is lifted by the presence of a gap. These states we denote as 0^+ and 0^- corresponding to energies $\pm E_g/2$ Eq.(2.44).

The spin degeneracy is lifted by the Zeeman effect and the Zeeman splitting between the spin up and down states is

$$\Delta E_Z = g\mu_B B = 0.12B[\mathrm{T}]\mathrm{meV}, \tag{2.45}$$

where μ_B is a Bohr magneton and $g \simeq 2$ is the gyromagnetic ratio for graphene [31]. In the simulations described in the following chapters this term is not included unless stated otherwise.

Within the tight-binding description the magnetic field is introduced through the Peierls phase factor [49, 50]

$$H_{nm} = H_{nm} \cdot \exp\left[i \frac{e}{\hbar} \int_{\vec{r}_n}^{\vec{r}_m} \vec{A} \cdot \mathrm{d}\vec{r} \right], \tag{2.46}$$

which corresponds to the phase an electron accumulates on the path from $\vec{r}_n$ to $\vec{r}_m$. This approach allows to account for both time-independent and time-dependent vector potentials. For example, in chapter 5 we will discuss the behavior of graphene under a short intense teraherz laser pulse, where we solve the time-dependent problem with the pulse included through its vector potential using the Peierls phase.

For the gauge $\vec{A} = B(-y, 0)$ the integral in Eq.(2.46) is given by

$$\int_{\vec{r}_n}^{\vec{r}_m} \vec{A} \cdot \mathrm{d}\vec{r} = -(x_m - x_n)(y_m + y_n)\frac{B}{2}. \tag{2.47}$$

For the gauge $\vec{A} = B(0, x)$ the result is

$$\int_{\vec{r}_n}^{\vec{r}_m} \vec{A} \cdot \mathrm{d}\vec{r} = -(y_m - y_n)(x_m + x_n)\frac{B}{2}. \tag{2.48}$$

2.5.1 Graphene nanoribbons in a perpendicular magnetic field

The solution of the Dirac equation in the presence of a homogeneous, perpendicular magnetic field [Eq.(2.37)] gets more complicated if one applies transverse confining potential [Eq.(2.27)] to describe a graphene nanoribbon in the presence of a magnetic field perpendicular to the ribbon. In this case, the Dirac equation does not have an analytic solution and the problem must be solved numerically. We can predict, however, that at $B \to 0$, the spectrum is determined by the size quantization of the ribbon and for high magnetic fields $B \to \infty$ when $l_B \ll W$, the spectrum should follow the Landau-level quantization [Eq.(2.41)]. Therefore, in general, the spectrum of the ribbon for $B \neq 0$ is a mixture of two effects: the size quantization and the Landau-level quantization.

Although the Dirac equation provides eigenstates of a ribbon in the magnetic field, for further applications (for example, while studying magneto-transport properties of disordered ribbons - see chapter 3) it is more convenient to use the tight-binding approximation and find eigenstates of a Hamiltonian matrix [Eq.(2.19)] with the magnetic Peierls phase [Eq.(2.46)] using the method discussed in subsection 2.4.1.

The bandstructure of graphene nanoribbons [Fig.2.6] becomes modified under the influence of the magnetic field [Fig.2.7]. In particular, we observe the appearance of flat parts in the subbands. These flat energy bands are assigned to the Landau level quantization of bulk graphene [Eq.(2.41)]. Such states have zero group velocity and, therefore, do not

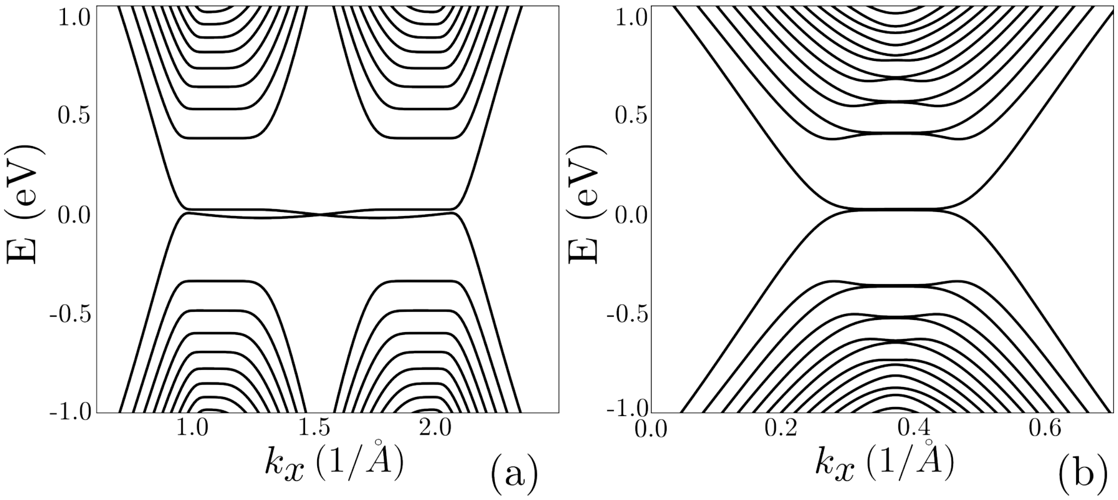

FIGURE 2.7: Bandstructure of (a) a 22 nm wide zigzag graphene nanoribbon and of (b) a 12 nm wide armchair graphene nanoribbon (AGNR) in the presence of a perpendicular magnetic field.

propagate. Classically, this means that electrons are confined within the ribbon by the magnetic field on circular cyclotron orbits [see Fig.2.8(a)]. The radius R of the classical orbit is proportional to the magnetic length $l_B \sim 1/\sqrt{B}$ and can be deduced from energy conservation

$$E_N = v_F p, \tag{2.49}$$

i.e. the energy of a confined Landau level state should be equal to the energy of a relativistic electron with a classical momentum p determined by the Lorentz force

$$\sqrt{2e\hbar v_F^2 NB} = v_F|e|BR. \tag{2.50}$$

Therefore, the state-dependent radius R_N of the classical trajectory is

$$R_N = \sqrt{2N} l_B. \tag{2.51}$$

In terms of quantum mechanics the electron has a wave function of the Hermite polynomial form, which is localized inside the ribbon [see, for example, local density of states (LDOS) of the 0^{th} Landau level Fig.2.8(b)]. The bands feature flat regions only if the characteristic size of the Landau level state, estimated as twice the radius [Eq.(2.51)] of the classical cyclotron trajectory, becomes smaller than the width W of the ribbon, i.e. $2R_N \lesssim W$. In this case, the circular electron trajectory fits into the ribbon and gets localized. The critical magnetic field needed to form the 1^{st} Landau level is

$$B_{\text{crit}} \gtrsim \frac{8\hbar}{eW^2}. \tag{2.52}$$

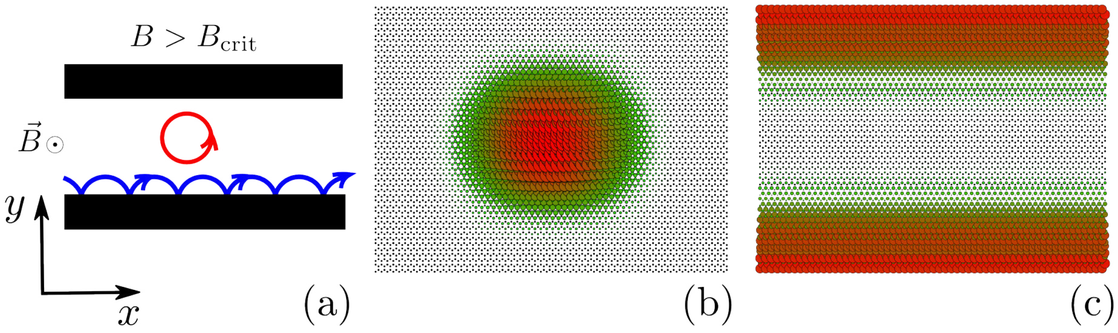

FIGURE 2.8: (a) Classical motion of the particle in the magnetic field $B > B_{\text{crit}}$. Red trajectory shows an orbit confined by the magnetic field. The blue trajectory represents a propagating edge state. (b) Local density of states (LDOS) of the 0^{th} Landau level for a zigzag GNR. (c) LDOS of the edge state formed by the magnetic field for a ZGNR.

To observe higher Landau levels, the magnetic field should be further increased. According to Eq.(2.51), the effective size of the wave function of the Landau level state N scales with the square root of the states number $\sqrt{N}$. Therefore, to resolve the N^{th} Landau level, one needs a magnetic field

$$B \gtrsim N B_{\text{crit}}. \tag{2.53}$$

For small magnetic fields ($B < B_{\text{crit}}$), the classical electron trajectory scatters off the edges of the ribbon before completing a circle. In this case, the electron is not confined by the magnetic field and its wave function is delocalized. The quantized electron energy spectrum in this magnetic field range is determined by the interplay between the size and magnetic field quantizations.

At high magnetic fields ($B > B_{\text{crit}}$), the propagation of electrons through the ribbon is still possible along the edges. Classically, electrons scatter at the edges and, thus, continue their motion [Fig.2.8(a)]. The wave function of such an electron becomes localized along the edges [see, for example, LDOS of an edge magnetic states of a ZGNR in Fig.2.8(c)]. Notably, due to the magnetic field electrons at the opposite sides of the ribbon propagate in opposite directions.

2.6 Lattice Green's function and its application to the transport problem

The lattice Green's function method is a powerful numerical tool for solving the single-particle Schrödinger equation. This approach allows the calculation of transmission, reflection and, thus, the scattering matrix of various scattering systems. The transmission coefficient or, likewise, the conductance within the Landauer-Büttiker formalism [50–52] is an important characteristic of the system. In particular, it allows for studying the size quantization in nanoribbons or quantum point contacts as well as the effects of disorder and interferences. By definition the Green's function contains information on the response of the whole system, when a "delta"-like excitation is applied to any of its points. Moreover, it can be used to calculate the local density of states and total charge densities at a given energy. Although the Green's function formalism also allows for inclusion of many-body effects (e.g., electron-electron or electron-phonon scattering), we restrict ourselves to the single-electron approximation, which is well justified for many experimental results.

The formal definition of the Green's function $G(E)$ [50, 51] is

$$G = \frac{1}{\hat{H} - E}, \tag{2.54}$$

where $\hat{H}$ is a Hamiltonian of the system. $G(E)$ is defined everywhere except at $E = E_n$, where E_n are eigenstates of the Hamiltonian $\hat{H}$. To avoid this singularity one can introduce a small imaginary shift η as

$$G^{\pm} = \lim_{\eta \to 0} \frac{1}{\hat{H} - E \pm i\eta}, \tag{2.55}$$

which is necessary for the evaluation of the Fourier transform of the Green's function. The two ($\pm$) Green's functions correspond to two different ways of avoiding the singularities while finding a Green's function in time domain. These Green's functions are usually called the retarded $G^R(t, t') = G^+(t, t')$ and the advanced $G^A(t, t') = G^-(t, t')$ Green's functions. They are responsible for the propagation (or evolution) of state in opposite direction of time from the point of excitation at $t = t'$ and can be thought of as outgoing and incoming waves [51].

Within the tight-binding approximation, the Green's function [Eq.(2.55)] is a finite size matrix, which corresponds to the inverted tight-binding Hamiltonian matrix [Eq.(2.19)] with modified on-site energies $\epsilon = \epsilon_0 - E \pm \eta$. This matrix connects together different sites and can be written for the case of 2D graphene in terms of lattice site representation

$$G^{\pm}(\vec{r}, \vec{r}'; E) = G^{\pm}(i, i'; E), \tag{2.56}$$

using the lattice site indices $\vec{r} = \vec{r_i} = \{i\}$.

It can be shown that the local density of states (LDOS), measured in scanning tunneling microscopy (STM) experiments, is given by the imaginary part of the Green's function

[51]

$$\rho(\vec{r}; E) = -\frac{1}{\pi}\text{Im}\left[G^{+}(\vec{r}, \vec{r}; E)\right]. \tag{2.57}$$

The LDOS provides an insight on the spatial distribution of electronic states within the nanodevice at a certain energy E. In particular, the LDOS allows for analyzing the behavior of different states upon the application of magnetic fields.

2.6.1 Transport problem

We now briefly discuss the scattering problem and the algorithm for finding the scattering matrix using the Green's function. We consider the following scattering problem: two half-infinite waveguides (or leads) are attached to a scattering region (or device) of a given shape [see Fig.2.9(a)]. The leads are modeled as semi-infinite ideal ribbons [see section 2.4] and are characterized by the number of open modes at the electron (Fermi) energy E_F. We find the lead solution, i.e. open and evanescent modes, using Eq. 2.34. For an electron with energy E_F injected from the left lead the transmission/reflection (T/R) probability to the right/left lead is calculated. The incoming and outgoing electrons are modeled as a superposition of lead states in the confinement direction and plane waves in the propagation direction [50, 51]. The relation between incoming and outgoing waves for a coherent conductor is given by the scattering matrix, which has a block structure

$$S = \left(\begin{array}{c|c} r^L & t^R \\ \hline t^L & r^R \end{array}\right) \tag{2.58}$$

where $r^L(r^R)$ and $t^L(t^R)$ are reflection and transmission coefficient through the device from the left (right) lead. For instance, for the system shown in Fig.2.9(a) with two open modes in the left lead and one in the right lead, the scattering matrix connects the appropriate incoming (a_i with i corresponding to the mode index) and outgoing (similarly b_i) amplitudes of the wave functions in the following way [51]:

$$\begin{pmatrix} b_1 \\ b_2 \\ b_3 \end{pmatrix} = \left(\begin{array}{cc|c} s_{11} & s_{12} & s_{13} \\ s_{21} & s_{22} & s_{23} \\ \hline s_{31} & s_{32} & s_{33} \end{array}\right) \begin{pmatrix} a_1 \\ a_2 \\ a_3 \end{pmatrix}, \tag{2.59}$$

where horizontal and vertical lines outline the block structure of the scattering matrix in accord with Eq.(2.58).

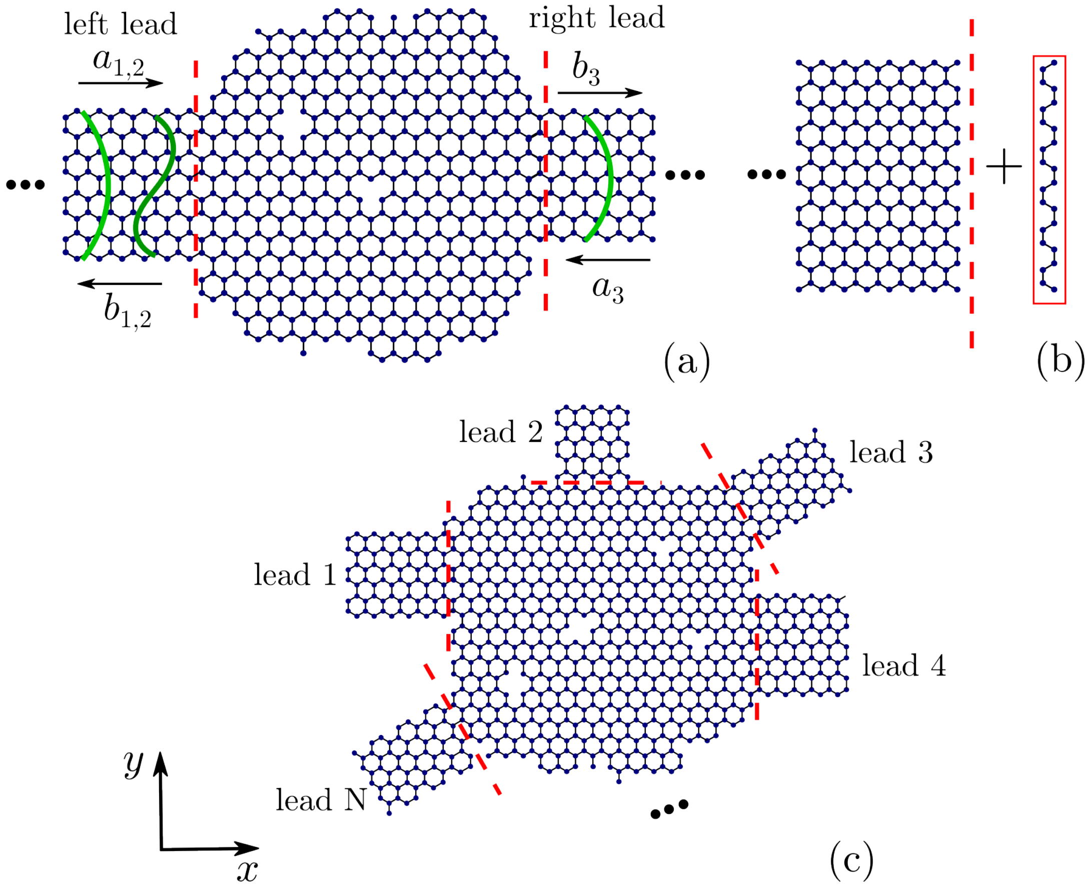

FIGURE 2.9: (a) Schematic representation of the scattering problem with two leads attached. In the case shown in figure, the electron energy is such that two and one modes are opened in the left and the right lead. The wave functions of the open modes are depicted in green. (b) The lead - single slice (or unit supercell) interface for a semi-infinite zigzag GNR. (c) Schematic representation of the scattering problem in the multi-lead case. In (a-c), the red dashed lines denote the lead-device interfaces.

2.6.2 Green's function of a system with attached contacts

The S-matrix can be evaluated using the Green's function method [34, 50, 51]. The Green's function matrix of the scattering region G^S is given by the inversion of the appropriate tight-binding Hamiltonian H^S [Eq.(2.55)]. The size of G^S is determined by the total number of atoms in the device. In the same way, we may formally write a Green's function G^{total} of a system with attached semi-infinite leads, which serve as contacts in our simulations [Fig.2.9(a)]. The matrix G^{total} has infinite dimension since the leads are semi-infinite. However, the coupling between the isolated device and the lead in the tight-binding approximation is non-zero only for adjacent grid points, which allows us to truncate the matrix to a finite size as will be shown below. The coupling matrix describing a device $-$ lead interface can be viewed as an interaction matrix H_I between the adjacent slices or supercells [see section 2.4 and Eq.(2.21) or Eq.(2.23)].

For simplicity, consider, first, a device with only one attached contact. The total Green's function of such a device can be found using Dyson's equation [34, 51]:

$$G^{\text{total}} = G^S + G^S H_I^\dagger g^L H_I G^{\text{total}}, \tag{2.60}$$

where g^L is the surface Green's function of the left semi-infinite lead (it is an infinite matrix). This equation can be rewritten as

$$G^{\text{total}} = \left[H^S - E_F I - H_I^\dagger g^L H_I\right]^{-1}, \tag{2.61}$$

where we used the definition of $G^S = [H^S - E_F I]^{-1}$ (I is the unity matrix) and we seek for a solution at the Fermi level E_F. The total Green's function G^{total} is different from the Green's function of an isolated device G^S only by the term called self-energy [51, 52]

$$\Sigma^L = H_I^\dagger g^L H_I. \tag{2.62}$$

The self-energy takes into account the interaction between the device and the contact. If now we attach a second contact on the right of the device, we can similarly find the self-energy for the right lead:

$$\Sigma^R = H_I g^R H_I^\dagger, \tag{2.63}$$

with the Green's function of the right lead g^R. As a result we can write the total Green's function for a device with two leads as

$$G^{\text{total}} = \left[H^S - E_F I - \Sigma^L - \Sigma^R\right]^{-1}. \tag{2.64}$$

In general, just by adding the corresponding self-energies in the denominator of the total Green's function it is possible to account for any number of contacts – leads [Fig.2.9(c)].

The only question remaining is how to find the Green's function matrices g^L and g^R of semi-infinite leads. This can be done if we consider the following system: we connect a semi-infinite lead with a single supercell of the same width as the lead [see Fig.2.9(b)]. Then the single slice plays the role of a scattering region described by G^S connected to a semi-infinite lead from the left. Therefore, the total Green's function G^{total} of a single supercell with only one lead attached can be found from Eq.(2.61). However, adding a single stripe does not change the semi-infinite lead and the total Green's function G^{total} in Eq.(2.61) must be identical to the Green's function of the lead g^L, i.e. $G^{\text{total}} = g^L$. As a result, Eq.(2.61), after multiplying by $(G^S)^{-1}$, yields

$$(H^S - E_F)g^L = I + H_I^\dagger g^L H_I g^L. \tag{2.65}$$

It can be shown [34] that if $g^L H_I$ is expressed in terms of an eigenvalue expansion of left moving Bloch states $|\chi^i\rangle$ in the lead

$$g^L H_I = \sum_{i=1}^{N} |\chi^i\rangle e^{ik_x^i \Delta x} \langle \chi^i|, \tag{2.66}$$

Eq.(2.65) is identical to Eq.(2.33). The size of this object is equal to the number of grid points at the device-lead interface. It is also depends on the electron energy E_F due to the expansion over the states of the infinite ribbon evaluated at the Fermi energy E_F. The same is, likewise, true for the right lead

$$g^R H_I^\dagger = \sum_{i'=1}^{N'} |\chi^{i'}\rangle e^{ik_x^{i'} \Delta x} \langle \chi^{i'}|, \tag{2.67}$$

with eigenvalue expansion of right moving Bloch states $|\chi^{i'}\rangle$. Therefore, the electronic states of the infinite waveguides calculated in subsection 2.4.2 are used to build a physical real space representation of the Green's functions describing the contacts.

2.6.3 Transmission coefficients

The Green's function allows us to find the S-matrix and, therefore, the transmission and reflection amplitudes. The elements of the scattering matrix are given by the Fisher-Lee relation [51, 53], which corresponds to the projection of the Green's function onto the propagating modes in the leads:

$$s_{nm} = -\delta_{nm} + i\hbar\sqrt{v_n v_m} \int\int \chi_n(y_p) G^{\text{total}}(x_p, y_p; x_q, y_q) \chi_m(y_q) dy_p dy_q \tag{2.68}$$

where $G^{\text{total}}(x_p, y_p; x_q, y_q)$ is the Green's function between the leads q and p, $(x_p,\ y_p)$ and $(x_q,\ y_q)$ are coordinates of the corresponding lead-device interface. The indices n and m are in $[1, N_{\text{total}}]$, where $N_{\text{total}} = N_L + N_R$ is the total number of propagating modes in both leads. The reflection coefficients $r_{nm} = s_{nm}$ correspond to the set of $(n,\ m)$ belonging to the same lead (and, therefore, $p = q$), whereas the transmission coefficients $t_{nm} = s_{nm}$ are determined by $(n,\ m)$ of different leads [and, therefore, $p \neq q$], i.e. $n \in [1, N_L]$ and $m \in [N_L + 1, N_L + N_R]$ or vice versa. The transmission probability is given by the absolute square of the corresponding transmission coefficient:

$$T_{nm} = |t_{nm}|^2 . \tag{2.69}$$

The total transmission is obtained through summation of T_{nm} over all open modes n and m available in the leads at the given energy E [51]. For example, the total transmission from left to right is

$$T = \sum_{n=1}^{N_L} \sum_{m=N_L}^{N_L+N_R} |t_{nm}|^2 . \tag{2.70}$$

Notably, to determine the total transmission, or the total S-matrix, it is not necessary to calculate the whole Green's function matrix by direct inversion. Calculating only certain element of the matrix $G^{\text{total}}(x_p, y_p; x_q, y_q)$ is enough, which substantially reduces the computational time.

In the experiment the macroscopic property related to the transmission is the conductance, which is determined as proportionality coefficient between measured current and applied voltage: $I = GV$. Within the Landauer-Büttiker formalism [50–52], the conductance G of a coherent device is directly proportional to the total transmission

$$G = \frac{2e^2}{h} T. \tag{2.71}$$

The factor 2 accounts for the spin multiplicity in spin-independent calculations.

The formalism above can be easily generalized to any number of leads [see Fig.2.9(c)]. In the experiment a multi-contact regime (or multi-lead regime) is preferable, as it lowers the residual resistance of the contacts and allows for better resolution of the signal (current).

The single-electron approximation we apply is valid only for coherent transport when the dephasing or the decoherence time due to inelastic scattering is large. This means that we neglect inelastic processes, such as electron-phonon or electron-electron scattering. However, we do treat elastic scattering at short-range lattice defects [54], long-range charge puddles [55], or rough edges [56].

2.7 Transition between Fermi energy and back gate voltage

Transport measurements are often done as a function of back gate voltage (V_{bg}), which tunes the amount of charge carriers in the graphene layer through capacitive coupling. Therefore, a change of V_{bg} allows for control of the Fermi level in the graphene sheet. However, theoretical predictions are usually determined as a function of electron (Fermi) energy E_F. From this perspective it is necessary to understand the functional correspondence between V_{bg} and E_F which we derive here.

The number of charge carriers N in graphene layer is given by the capacitive gate coupling α

$$N = \alpha V_{\mathrm{bg}}, \tag{2.72}$$

where α is usually of the order of $7 \cdot 10^{10}$ cm^{-2}V^{-1} and can be determined experimentally from the lever-arm of Coulomb diamonds for graphene dots [57] or from high magnetic field Landau level measurements for bulk graphene [27]. On the other hand, the number of charge carriers N in general is given by the integration of the density of states $\rho(E)$ from the Dirac point up to the Fermi level (for the hole side the integration limits are flipped):

$$N = \int_0^{E_F} \rho(E) dE. \tag{2.73}$$

Due to the linear dispersion of Dirac fermions, the integral in Eq.(2.73) leads to a square root dependence between E_F and N and similarly between E_F and V_{bg} by taking into account Eq.(2.72),

$$E_F = \hbar v_F \sqrt{\pi \alpha V_{\mathrm{bg}}}. \tag{2.74}$$

Notably, for a density of states with nonlinear behavior, the functional dependence between E_F and V_{bg} can still be found through the integration of Eq.(2.73), however, the result will differ from Eq.(2.74).

2.8 Fast Fourier transform on a graphene lattice

Fourier transform of a real space wave function allows for analyzing its momentum distribution. In the tight-binding approximation, a wave function is a vector $|\phi\rangle$ with elements ϕ_i computed on a graphene lattice for each lattice point i described by the position vector $\vec{r}_i$. To obtain a real space wave function $\Psi(\vec{r})$ one needs to multiply the tight-binding wave function with the real space representation of the p_z orbital $\Psi_{p_z}(\vec{r})$ of the valence electrons in graphene at each lattice site:

$$\Psi(\vec{r}) = \sum_i \Psi_{p_z}(\vec{r} - \vec{r}_i) \cdot \phi_i, \tag{2.75}$$

where the summation extends over the whole structure. As soon as $\Psi(\vec{r})$ is known it is straight-forward to obtain its Fourier transform $\mathcal{F}[\Psi(\vec{r})]$. Computationally, the wave function $\Psi(\vec{r})$ is represented on a Cartesian grid, which must adequately describe $\Psi(\vec{r})$ in the real space. Consequently, the grid size usually is much larger than the number of atoms in the device. It is, thus, challenging, e.g., to store or to Fourier transform the real space representation $\Psi(\vec{r})$ of the wave function if the number of atoms in the system is large. Instead of evaluating the Fourier transform of the wave function directly, we note that it can be calculated using the convolution theorem as

$$\begin{aligned}\mathcal{F}[\Psi(\vec{r})] &= \sum_i \int \Psi_{p_z}(\vec{r}-\vec{r}_i)\cdot\phi_i e^{-i\vec{k}\vec{r}}d\vec{r} = \\ &= \sum_i \phi_i e^{-i\vec{k}\vec{r}_i}\int \Psi_{p_z}(\vec{r}-\vec{r}_i)e^{-i\vec{k}(\vec{r}-\vec{r}_i)}d\vec{r} = \\ &= \mathcal{F}[\Psi_{p_z}(\vec{r})]\cdot\mathcal{F}[\phi].\end{aligned} \tag{2.76}$$

In other words, the Fourier transform of the wave function is the product of the p_z orbital Fourier transform $\mathcal{F}[\Psi_{p_z}(\vec{r})]$ and the discrete Fourier transform of the tight-binding wave function $\mathcal{F}[\phi]$. As a result, the computation of the Fourier transform is limited only by the total number of lattice sites, because there is no difficulty to find $\mathcal{F}[\Psi_{p_z}(\vec{r})]$ for a given orbital representation. A localized real space orbital gives a broad contribution to the total Fourier spectrum; however, the detailed structure of the Fourier spectrum is governed by $\mathcal{F}[\phi]$. Notably, if $\phi_i = 1$, its Fourier transform $\mathcal{F}[\phi] = \sum_i e^{-i\vec{k}\vec{r}_i}$ coincides with the structure factor $S_{\text{struct}}(\vec{k})$ used to characterize the elastic scattering of particles off a crystal [58].

Evaluating $\mathcal{F}[\phi]$ can be further optimized for rectangular graphene flakes.[1] The graphene lattice for flakes with zigzag and armchair termination can be viewed as a superposition of four orthogonal lattices with lattice vectors $\vec{a}_1 = (\sqrt{3}a, 0)$ and $\vec{a}_2 = (0, 3a)$ shifted with respect to each other [see Fig.2.10(a), where lattice sites marked with the same color belong to one orthogonal sublattice]. Their relative displacements are (0, 0), ($a_{1x}/2$, $a_{2y}/6$), ($a_{1x}/2$, $a_{2y}/2$) and (0, $2a_{2y}/3$). We can, thus, find a discrete Fourier transform of the wave functions determined on different sublattices [which we denote as $\phi^{(1)}$, $\phi^{(2)}$, $\phi^{(3)}$ and $\phi^{(4)}$] independently and combine them with an appropriate phase shift due to the finite displacement of the sublattices with respect to the origin. The proof of the last statement is based on the definition of the discrete Fourier transform:

$$\begin{aligned}\mathcal{F}[\phi]_{k_x,k_y} = &\sum_{j=0}^{Nx\cdot Ny/4} \phi_j^{(1)}e^{-i(k_x x_j + k_y y_j)} + \phi_j^{(2)}e^{-i(k_x(x_j+a_{1x}/2)+k_y(y_j+a_{2y}/6))}+ \\ &\phi_j^{(3)}e^{-i(k_x(x_j+a_{1x}/2)+k_y(y_j+a_{2y}/2))} + \phi_j^{(4)}e^{-i(k_x x_j + k_y(y_j+2a_{2y}/3))} = \\ &= \mathcal{F}[\phi^{(1)}]_{k_x,k_y} + \mathcal{F}[\phi^{(2)}]_{k_x,k_y}e^{-i(k_x a_{1x}+k_y a_{2y}/3)/2}+ \\ &\mathcal{F}[\phi^{(3)}]_{k_x,k_y}e^{-i(k_x a_{1x}+k_y a_{2y})/2} + \mathcal{F}[\phi^{(4)}]_{k_x,k_y}e^{-ik_y 2a_{2y}/3},\end{aligned} \tag{2.77}$$

where j are the lattice site indices of the orthogonal sublattice. Since optimized algorithms exist for Cartesian grids (e.g., fast Fourier transform), this approach greatly speeds up the calculation time.

---

[1] Other device geometries can be modeled by applying a step-like potential following the specific shape of the nanostructure.

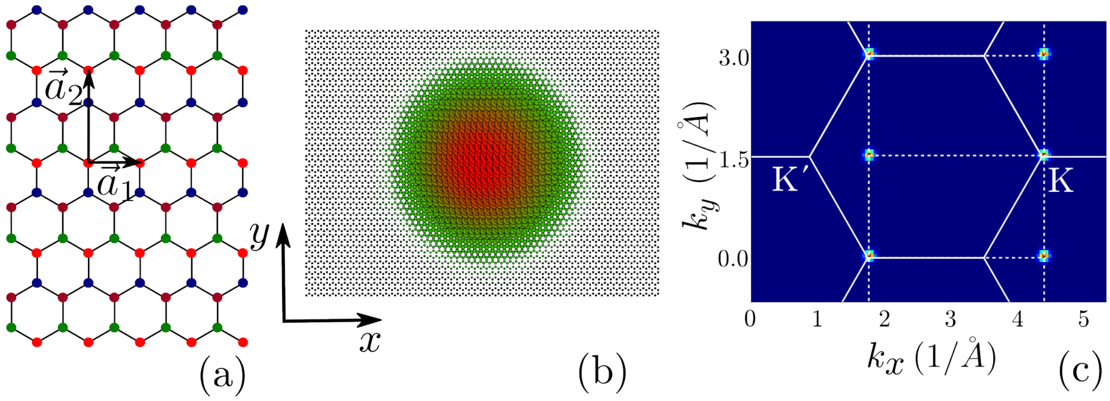

Figure 2.10: (a) Graphene lattice consists of four orthogonal sublattices shown by orange, green, brown and blue atoms. The lattice vectors of these sublattices are $\vec{a}_1$ and $\vec{a}_2$. (b) The real space wave function in the form of a Gaussian with an initial momentum near the K point $\vec{k} = (1.7, 0)$ Å^{-1} on a rectangular graphene flake. (c) A Fourier transform showing the momentum space representation of the wave packet in (b). The Fourier transform is calculated using Eq.(2.77). It features Gaussians localized at the K points as well as Gaussians located off the K or K' points. The centers of the Gaussians form an orthogonal lattice shown by white dashed lines, which coincides with the reciprocal lattice of the orthogonal sublattices depicted in (a).

Let us now consider an example of a tight-binding wave function ϕ in the form of a Gaussian wave packed defined on a graphene flake of size $L_x \times L_y = 25 \times 15$ nm^2 with an initial momentum near the K point $\vec{k} = (1.7, 0)$ Å^{-1} [see Fig.2.10(b)]. Indeed, by evaluating the Fourier transform of ϕ using Eq.(2.77), we find Gaussians located exactly at the Dirac K points [see Fig.2.10(c), the Brillouin zone is shown in white]. In addition we find Gaussians located off the K or K' points [see Fig.2.10(c), where some of the Gaussians are located inside the hexagonal Brillouin zones]. Interestingly, the centers of the Gaussians form a rectangular lattice in reciprocal space [shown by white dashed lines in Fig.2.10(c)]. This additional symmetry is an artifact arising from the the presence of the four orthogonal sublattices [see Fig.2.10(a)] in a rectangular flake, which we employed to derive Eq.(2.77). The reciprocal lattice of these orthogonal sublattices coincides with the position of the Gaussians.

Chapter 3

Observation of size quantization in graphene nanodevices: transition to Landau levels

The ability to probe ballistic transport in graphene strongly depends on the amount of disorder in a graphene device. The roughness of the substrate material induces corrugation of the graphene monolayer [59], charge puddles [55], and charge traps [30] leading to diffusive transport behavior and dramatically lowering the mobility. Reducing substrate-induced disorder is critical for achieving higher carrier mobility especially in transport applications. The advances in fabrication of graphene nanostructures made it possible to realize well-known phenomena of mesoscopic systems in application to graphene. For example, the study of ballistic transport through graphene nanoribbons grown on SiC [60] led to the discovery of an exceptional temperature independent single spin mode which remains unexplained by theory. The size quantization due to confinement of Dirac fermions first measured on suspended graphene nanoribbons [61] is very sensitive to disorder and is much more challenging to observe in experiment than in a two-dimensional electron gas (2DEG) in GaAs-AlGaAs heterostructures [62]. Further reduction of bulk disorder was achieved in nanodevices built on top of an atomically flat hexagonal boron nitride substrate [13, 14, 63] or in graphene - hexagonal boron nitride (hBN) sandwiches [27]. Although the bulk disorder in such devices is reduced, scattering at the edge still can play a crucial role. For example, in a recent study [64] the observation of unconventional Coulomb blockade in nanoribbons attached to wide leads was attributed to the charging of localized states at the edges. In an experiment by Terres et al. [27], which we discuss in this chapter, the size quantization was observed in small-size ballistic quantum point contacts (QPCs) which are narrow constrictions with comparable width and length confined between large conducting areas. The deviation of the conductance signal from the theoretical expectations allowed us to make a link to the density of localized states at the edges of the device. These findings highlight the important role of trapped edge states on transport measurements as a function of back gate voltage.

In this chapter we focus on the theoretical aspects of ballistic transport through graphene nanodevices using the Green's function formalism described in section 2.6. In particular, we study size quantization in nanoribbons and quantum point contacts. Our tight-binding calculations allow us to explain the main features observed in experiment [27] and to directly compare the size quantization in a 2DEG and graphene quantum point contacts. We also investigate the evolution of size quantization with the magnetic field and the transition to Landau levels in confined systems with and without disorder.

3.1 Quantum transport and size quantization in nanoribbons and quantum point contacts

In an ideal ballistic nanoribbon geometry with perfect edges the conductance as a function of energy is a staircase function. It increases by e^2/h each time a new size quantization channel becomes available to the charge carriers as their energy increase. Therefore, the conductance [Eq.(2.71)] can be written as a sum of occupied open modes at a given Fermi level E_F:

$$G = \frac{2e^2}{h} \sum_{n=1}^{\infty} \Theta\left(E_F - E_n\right), \tag{3.1}$$

where the factor 2 accounts for the spin multiplicity and E_n stands for the energy of the subbands due to size quantization. Using Eq.(2.32), which estimates the number of open modes in graphene nanoribbons, the conductance can be rewritten as

$$G = \frac{4e^2}{h} \sum_{i=1}^{\infty} \Theta\left(\frac{WE_F}{\pi\hbar v_F} - i\right) = \frac{4e^2}{h} \sum_{i=1}^{\infty} \Theta\left(\frac{Wk_F}{\pi} - i\right), \tag{3.2}$$

where the additional factor of 2 accounts for valley degeneracy, the Fermi wave vector $k_F = E_F/\hbar v_F$ for graphene, and we neglect the phase factor 1/2 arising from the zigzag edge. The conductance of graphene nanoribbons calculated using Green's function method [section 2.6] as function of Fermi energy E_F reproduces this staircase behavior [see Fig.3.1(a) green and red traces].

The Fourier expansion of Eq.(3.2) yields

$$G = \frac{4e^2}{h}\left(\frac{Wk_F}{\pi}c_0 + \sum_{j=1}^{\infty} c_j \sin\left(2\pi j \frac{Wk_F}{\pi}\right)\right) \tag{3.3}$$

with $c_0 = 1$ and $c_j = 1/(j\pi)$. The first term

$$G^{(0)} = \frac{4e^2}{h}\frac{Wk_F}{\pi}c_0 = \frac{4e^2}{h}\frac{W}{\pi}c_0\sqrt{\pi\alpha V_{\rm bg}} \tag{3.4}$$

describes an average increase of conductance. It is proportional to the square root of $V_{\rm bg}$ according to Eq.(2.74). In the presence of disorder, i.e. bulk or edge disorder, the average conductance decreases due to enhanced backscattering in the ribbon and, therefore, the coefficient c_0 drops in magnitude. The higher Fourier components in Eq.(3.3) form the sharp steps. In a realistic nanoribbon the amplitude of these harmonics c_j is expected to decay faster than $1/j$ and to acquire an additional phase due to random scattering processes in a disordered nanoribbon. Consequently, the sharp quantization steps turn into modulations on top of the average conductance $G^{(0)}$.

Size quantization plateaus in the conductance were observed for the first time in a high-mobility ($\mu \sim 10^6$ cm^2/Vs) two-dimensional electron gas (2DEG) created in GaAs-AlGaAs heterostructures [62]. The device was shaped in a form of a quantum point contact (QPC), which is a narrow constriction with similar width and length confined between two wide conducting regions [see Fig.3.1(c, d)]. The quantum point contact in semiconductor heterostructures was realized by applying a voltage between two side gates shaping a narrow region with smooth boundaries in between, forming an effectively one-dimensional electron gas (1DEG). The transverse confinement of the electrons led to quantization of conductance in a similar way as in waveguides [Eq.(3.1)]. The size quantization in the 2DEG confined to a narrow region of width W is

$$E_n = \frac{\hbar^2\pi^2}{2m^*W^2}n^2, \tag{3.5}$$

where m^* is the effective electron mass. In the adiabatic transport model the conductance through a QPC with smooth boundaries approximated by a parabolic function αx^2 [50] can be written as a sum of Fermi-like functions:

$$G = \frac{2e^2}{h}\sum_n \frac{1}{1+e^{-\beta_n[E_F-E_n]}}, \tag{3.6}$$

where

$$\beta_n = \sqrt{\frac{2m^*}{\alpha\hbar^2 E_n}}. \tag{3.7}$$

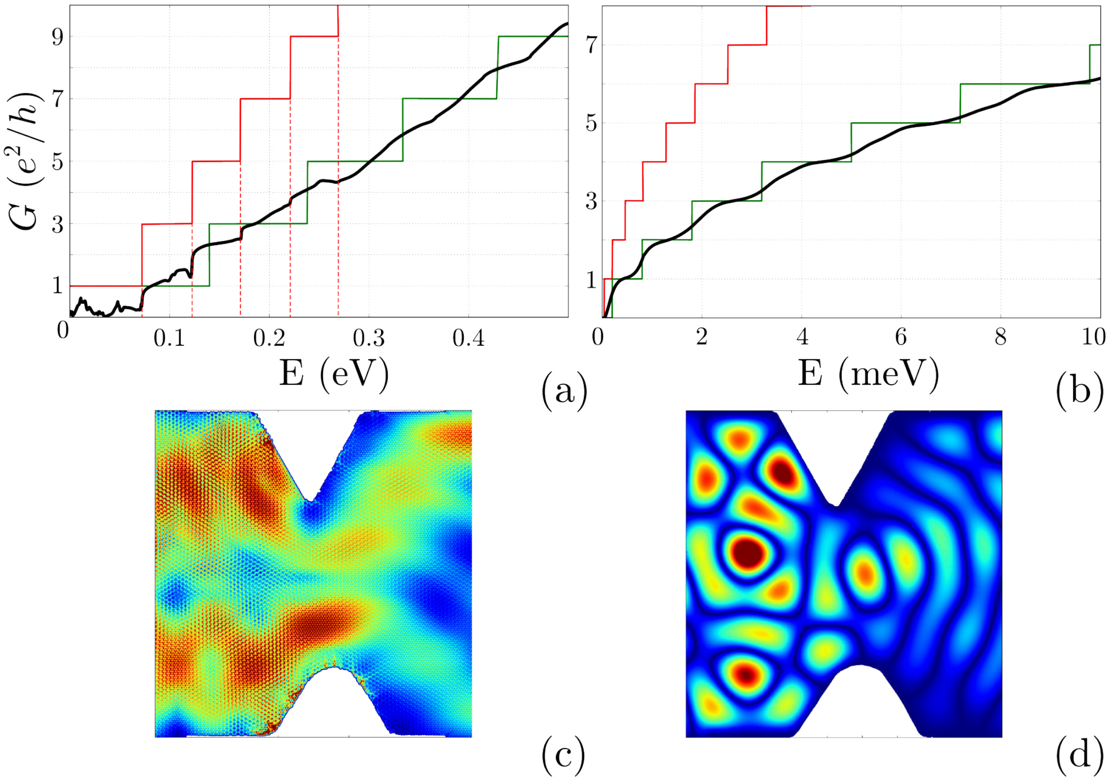

Figure 3.1: Calculated conductance (black traces) of (a) graphene and (b) 2DEG quantum point contacts as a function of electron energy. Green steps show the quantized conductance of an ideal ribbon of the QPC width. Red steps are the quantized conductance of the leads. In (a) red dashed lines correspond to the onset of the mode openings in the leads (red steps). For low energies these lines coincide with the positions of the step-like increase in the conductance (black curve). Examples of a wave function in (c) graphene and (d) 2DEG QPCs.

If $\alpha = 0$, i.e. in the limit of an infinite waveguide, we recover conductance given by Eq.(3.1). For long constrictions with small α (and large β_n) well-defined steps are expected, whereas for a sharp QPC with large α the steps are smoothed out. In other words, the amplitude c_j of higher Fourier components in Eq.(3.3), where for 2DEG $k_F = \sqrt{2m^* E_F}$ and prefactor is $2e^2/h$, decays faster for shorter constrictions. In addition, the adiabatic approximation implies that c_j does not acquire a (substantial) random phase during the transport process due to scattering at impurities or boundaries.

In a 2DEG the electron wave length near the Γ point is very long and cannot resolve disorder on sub-nanometer scale. Therefore, for short QPCs the adiabatic approximation is valid and smooth steps are observed [62]. However, the effect of impurities or edge roughness (which is of the order of several nanometers) scattering becomes important as the length of the quantum point contact increases. Back scattering enhances the randomization of transmission, breaking the adiabatic approximation and restricting the observation of sharp steps in the conductance in the experiment. In contrast to a 2DEG, the conducting electrons in graphene have a momentum near the K (or K') point and, therefore, a much shorter wave length. As a result, scattering at atomically rough edges has a substantial impact on transport even for short quantum point contacts. This sensitivity of electrons in graphene to atomic roughness is most probably responsible for the difficulties in observing clear confinement quantization effects in graphene nanodevices [61, 65].

To corroborate this discussion, we perform tight-binding transport simulations for graphene and a 2DEG in the same quantum point contact geometry[1] with two infinite leads attached [see example of scattering wave functions in graphene and a 2DEG QPCs in Fig.3.1(c) and (d)]. We chose this geometry of the QPC from an experiment [27] discussed in section 3.2. In our calculations the width of the QPC is $W = 16.5$ nm. The width of the leads is $2W$. Graphene and 2DEG quantum point contacts have no bulk disorder and only edge roughness on the atomic scale due to the shape of the constriction. It is evident that the calculated conductance as function of electron energy behaves differently for graphene and a 2DEG [compare black traces in Fig.3.1(a) for graphene and (b) for the 2DEG]. In particular, for the 2DEG we observe a smooth conductance signal [black trace in Fig.3.1(b)], which follows the size quantization steps of an infinite waveguide of width W [green trace in Fig.3.1(b)]. The smoothed steps can be described by a sum of smooth Fermi-like functions [Eq.(3.6)] within the adiabatic approximation. By contrast, the calculated conductance of the graphene QPC as function of electron energy is more complex [black trace in Fig.3.1(a)]. Especially at small energies $E \lesssim 0.25$ eV the conductance is modulated not by the size quantization corresponding to the narrowest region of width W [green steps in Fig.3.1(a)], but by the size quantization of the leads of width $2W$ [red steps in Fig.3.1(a)]. This is a consequence of the conservation of the electron chirality ($\hat{h} = \vec{\sigma} \cdot \vec{p}/2|\vec{p}|$ introduced in section 2.2) near the Dirac point, which implies the conservation of the propagating direction. Although the conservation of helicity or chirality is partially destroyed by the QPC boundaries, it still can enhance the transport near the Dirac point, where the Dirac cone approximation is accurate. This additional integral of motion does not exist for Schrödinger electrons in 2DEG and, therefore, no enhanced transmission is observed close to the Γ point. The mean of the calculated transmission $G^{(0)}$ for graphene, however, follows Eq.(3.4) if we assume the QPC width W. At higher energies, where the helicity is destroyed due to the deviations of the bandstructure from the idealized Dirac cone, the size and height of the modulations start to follow the conductance determined by the width W of the QPC [see green steps in Fig.3.1(a)] rather than that of the leads in accord with the traces we observe for the 2DEG.

---

[1] The tight-biding transport simulation for 2DEG were performed in the same way as for graphene, however, on a square lattice. In the case of parabolic dispersion of 2DEG H_0 matrix is tri-diagonal with on-site energies $\epsilon_0 = 4\hbar^2/2m^*a^2$ and first-nearest-neighbor coupling $t_1 = -\hbar^2/2m^*a^2$, where a is the lattice spacing and m^* is an effective electron mass in the semiconductor. The interaction matrix H_I is diagonal with elements equal to t_1.

Our calculations suggest that a smooth quantized conductance can be observed in graphene QPC with smooth edges. Adding a small edge roughness (of about 1% of the QPC width) leads to random fluctuations in the conductance, which destroy the smooth modulations due to the size quantization in the constriction region. Unfortunately, current state of the art experimental patterning techniques usually produce rough edges and the parameters of the roughness are unknown. However, evidence of quantized conductance can still be found in experiments as discussed in the following section.

3.2 Experimental evidence of the size quantization in graphene quantum point contacts

The observation of quantum confinement was reported by Terrés et al. [27], who investigated the transport through high-mobility graphene-hBN sandwich devices patterned in the shape of a quantum point contact with widths ranging from $W \approx 230$ to 850 nm. Unlike the 2DEG QPCs, it is not possible to confine electrons in graphene by applying a side gate voltage and, therefore, the shape of the constriction has to be patterned by removing graphene atoms. The measurements were performed in a four-terminal configuration to avoid residual contact resistances. In this configuration the conductance is

$$G = \frac{I_{13}}{V_{24}} \tag{3.8}$$

with the small bias voltage V_{24} applied between the diagonal contacts 2 and 4, and the current I_{13} measured between the other two contacts 1 and 3 [for the device geometry see inset in Fig.3.2(a)]. The conductance was measured as a function of back gate voltage V_{bg}, which allows for changing the Fermi energy [see section 2.7]. In this section we discuss the conductance traces for two different cool-downs [Fig.3.2(a, b)] of the same device of width $W \approx 230$ nm. The width is determined from scanning electron microscopy (SEM) images.

Away from the Dirac point, the measured transmission curves in graphene QPCs [black and blue curves in Fig.3.2(a, b)], indeed, follow the theoretical prediction of $G^{(0)}$ given by Eq.(3.4) [red curves in Fig.3.2(a, b)]. From the best fit of Eq.(3.4) to the experimental data we can extract the zeroth order Fourier amplitude c_0 of around 0.56, which is substantially smaller than 1 due to reflections influenced by the device geometry and the edge roughness. From the reduction of c_0 under the assumption of no bulk disorder, we can estimate the edge disorder amplitude ΔW defined for each edge as a difference between the geometrical width W and the reduced width $c_0 W$ divided by the number of edges, i.e.

$$\Delta W = (1 - c_0)W/2 \approx 0.2W. \tag{3.9}$$

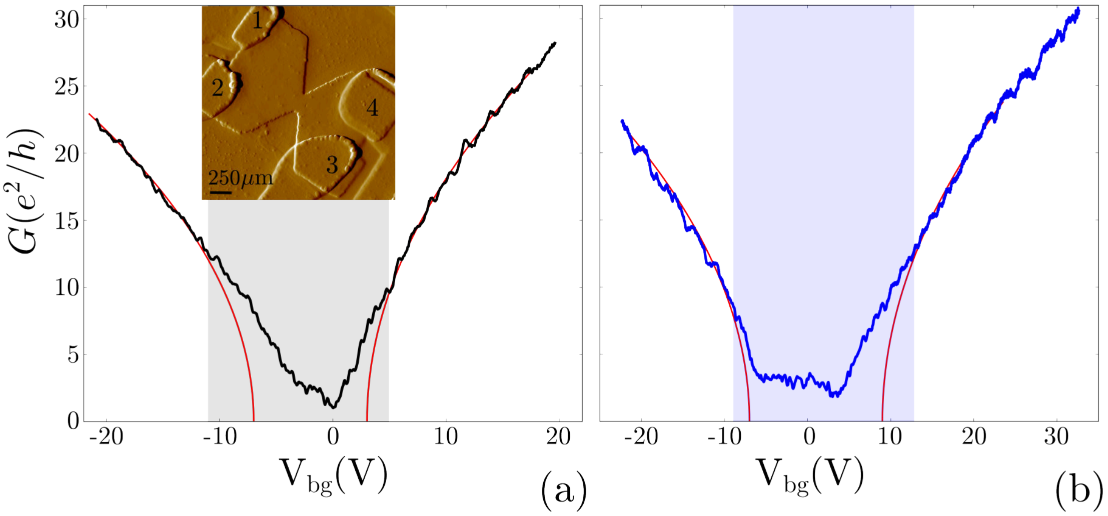

FIGURE 3.2: (a,b) Measured back gate voltage dependence of the conductance for two cool-downs shown in black and blue. Red curves correspond to the best fit of the average conductance $G^{(0)}$ [Eq.(3.4)] to the experiment. The shaded areas mark the regions, where the conductance traces substantially deviate from the expected average conductance $G^{(0)}$. The atomic force microscope (AFM) image of the device geometry is shown in the inset of (a).

Such a large disorder at the edges could possibly arise due to the formation of microcracks during the etching of the constriction. The rough edges dramatically increase the scattering, leading to rapid decay and additional random phase of high Fourier components c_j [Eq.(3.3)]. For this reason the observation of perfect quantization steps in the conductance is impossible. Indeed, the conductance traces only show some quasi-periodic modulations, "kinks", on top of $G^{(0)}$. We discuss these modulations in more details in subsection 3.2.2.

To fit the experimental data and to extract W, we use the lever arm $\alpha = 7.2{\cdot}10^{10}$ cm^{-2}V^{-1} for the first cool-down [shown in Fig.3.2(a)] and $\alpha = 6.2 \cdot 10^{10}$ cm^{-2}V^{-1} for the second cool-down [shown in Fig.3.2(b)]. In the experiment these capacitive couplings were obtained independently through Landau level fan measurements for each cool-down. The Landau levels [Eq.(2.41)] on the V_{bg} - B plane are

$$V_{\mathrm{bg}}^{N} = \frac{2|e|N}{\pi\alpha\hbar}B, \quad N \in Z_0, \tag{3.10}$$

and α is extracted from the slopes of these linear Landau levels. The difference in α between two cool-downs can be explained by a change of the chemical composition of the edges while the device was brought to room temperature and subsequently cooled down again [see also subsection 3.2.1 for more discussion]. The additional charge traps acquired by the edges as well as the additional charge contamination of the substrate during cool-down processes slightly modifies the capacitive coupling resulting in a cool-down dependent α.

3.2.1 Localized edge states in QPC

Surprisingly, the measured conductance deviates from the square root behavior or average conductance $G^{(0)}$ near the Dirac point in both cool-downs [see shaded regions in Fig.3.2(a,b)]. As we discussed in section 2.7, the square root dependence of E_F on $V_{\rm bg}$ assumes a linear density of states as a function of energy. However, rough edges or bulk disorder will modify the density of states (DOS), as the localized states at the rough edges give a prominent contribution to the density of states near the Dirac point [64, 66]. Although these states do not contribute to transport, they modify the total number of charge carriers on the device

$$N = \int_0^{E_F} \rho(E)dE = \int_0^{E_F} \rho^D(E)dE + \int_0^{E_F} \rho^T(E)dE, \tag{3.11}$$

where $\rho^D(E)$ is the linear DOS of conducting Dirac fermions and $\rho^T(E)$ is the DOS of the trapped and localized states. The connection between N and the back gate voltage is given by Eq.(2.72). We, therefore, write

$$\alpha V_{\rm bg} = \pi^{-1}\left(\frac{E_F}{\hbar v_F}\right)^2 + N^T(V_{\rm bg}), \tag{3.12}$$

where $N^T(V_{\rm bg})$ is the amount of the trapped charge. Our tight-binding density of states calculations for the real device geometry [see Fig.3.3(a,b)] confirms the presence of the trapped states at the edges. Their energies lie close to the Dirac point [see green trace in Fig.3.3(c)] leading to the deviation of the DOS from the expected linear behavior of Dirac fermions [see red trace in Fig.3.3(c)]. Away from the Dirac point, the density of localized states decreases and the second term in Eq.(3.12) becomes a constant equal to the total amount of trapped charge. Consequently, the expected square root dependence of the conductance on $V_{\rm bg}$ [Eq.(3.4)] is restored with a constant shift proportional to the total number of trapped charge given by $N^T = \int_0^\infty \rho^T(E)dE$ for the electron side and by $N^T = \int_{-\infty}^0 \rho^T(E)dE$ for the hole side.

We therefore propose that in the experiment deviations of the conductance from the square root behavior near the Dirac point [shaded areas in Fig.(3.2)] is governed by the charging of the trapped states. We extract the DOS of the localized states using this deviation. Substituting E_F determined by Eq.(3.12) in Eq.(3.4) we find:

$$G = \frac{4e^2}{h}\frac{WE_F}{\hbar\pi v_F} = \frac{4e^2}{h}\frac{W}{\pi}k_F = \frac{4e^2}{h}\frac{W}{\pi}\sqrt{\pi\alpha V_{\rm bg} - N^T(V_{\rm bg})}. \tag{3.13}$$

We approximate DOS of the trapped states $\rho^T(E)$ by a Gaussian to preserve the small-scale oscillations of the measured conductance. From the fit of the theoretical estimate

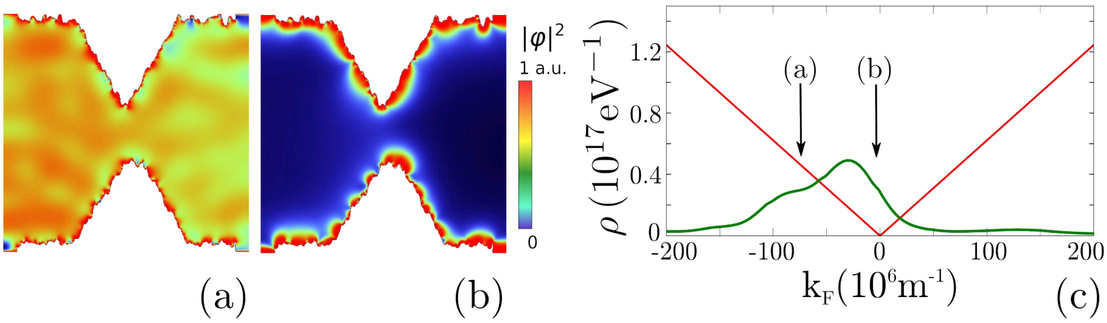

FIGURE 3.3: (a,b) The calculated local density of states for the device geometry corresponding to the experiment features edge localized states. (c) Calculated density of states (DOS) of the trapped/localized states (green) in the device geometry shown in (a,b). Red lines are the expected linear DOS of Dirac fermions.

[Eq.(3.13)] to the measured conductance traces [Fig.3.2] we extract the parameters of the Gaussian DOS, $\rho^T(E)$, i.e. the position of the center, width and height of the Gaussian [Fig.(3.4)(c) and (d)]. The shift of the Gaussian relative to the Dirac point is linked to the asymmetry of the transmission traces [Fig.(3.2)] near the charge neutrality point or $V_{\text{bg}} = 0$. The area of the Gaussian determines the effective number of trapped states. In particular, we extract a wider Gaussian for the second cool-down (of the same device), which supports our previous discussion of changing of the chemical composition of the edges, i.e. the increasing edge contamination, between two cool-downs. The chemical contamination of the edges affects the capacitive coupling α and the transmission measurements.

The estimate of $\rho^T(E)$ together with the linear DOS of Dirac fermions allows us to establish a connection between the back gate voltage and the Fermi energy. The conductance traces as a function of energy feature linear behavior in the whole energy range as predicted by Eq.(3.4) [black and blue traces in Fig.3.4(a, b)]. Notably, if we do not include the trapped states ($\rho^T(E)$=0) and use only the square root energy-voltage correspondence [Eq.(2.74)], the conductance traces substantially deviate from the linear behavior near $E_F \sim k_F \approx 0$ [red traces in Fig.3.4(a, b)]. This further supports our argument of the influence of the localized edge states on the experimental signal.

3.2.2 Size quantization in QPC

We discussed so far the effect of localized states on the average conductance. However, besides the overall linear (as a function of $E_F \sim k_F$) behavior of the conductance traces, we observe also modulations ("kinks") of the signal [Fig.3.4(a, b)]. These modulations, according to the Fourier expansion of an ideal conductance [Eq.(3.3)], should be a consequence of the size quantization in the quantum point contact. The Fourier analysis of the conductance after subtracting the zeroth-order Fourier component $G^{(0)} \sim k_F$,

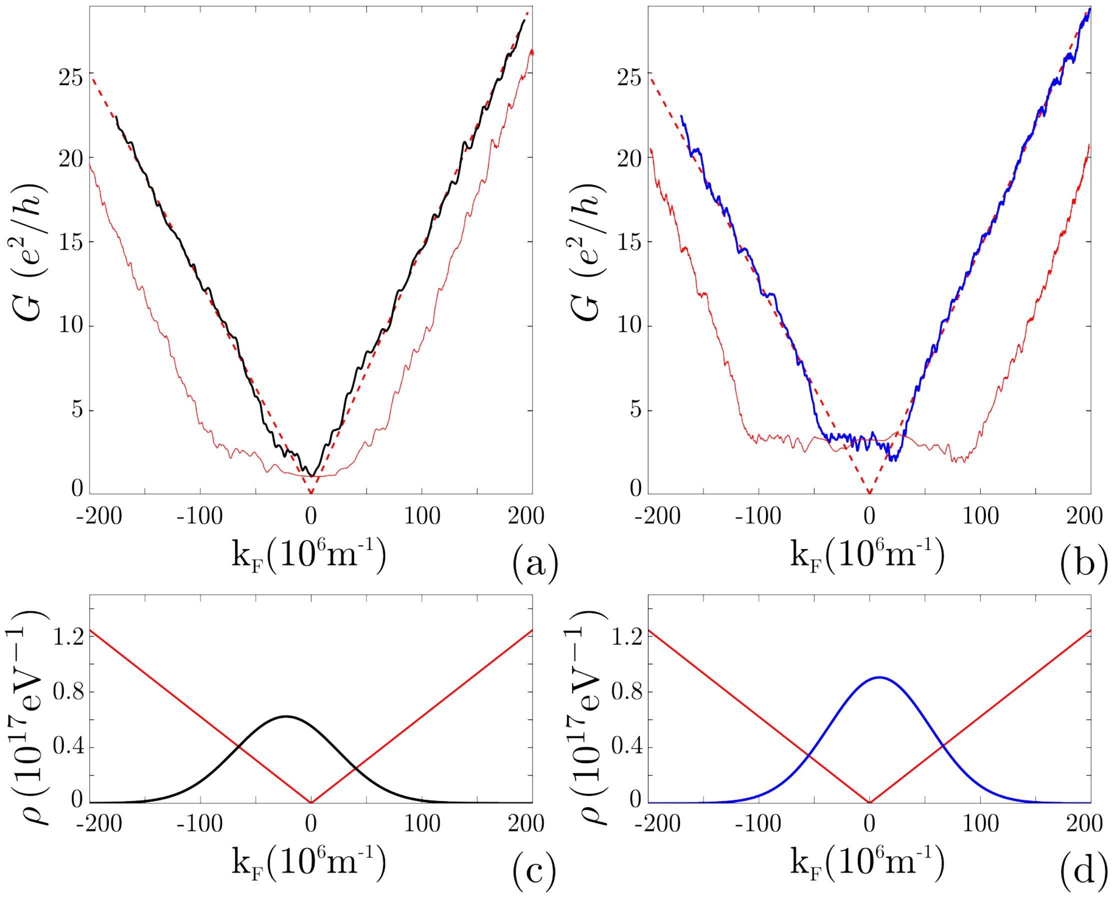

Figure 3.4: (a,b) Black and blue trances are the measured conductances as a function of k_F ($\sim E_F$) for the two cool-downs. The transition from back gate voltage to energy (or k_F) scale includes the density of localized edge states shown in (c,d). Red dashed lines correspond to the average conductance $G^{(0)}$ [Eq.(3.4)]. Neglecting the trapped/localized states leads to significant changes in conductance shown by red traces. (c,d) Black and blue Gaussian are the DOS of trapped states obtained from the deviations of the measured conductance near the Dirac point from the square root dependence on V_{bg}. Red lines are the expected DOS of the Dirac fermions.

i.e. $\delta G = G - G^{(0)}$, allows us to determine the length scales in the system influencing the signal. In particular, we observe a pronounced peak of the first order harmonic at approximately 230 nm [see black curves in Fig.3.5(c)], which is consistent with the width W of the device extracted from SEM. By contrast, the zeroth order Fourier component, i.e. average conductance, yields lower value of an effective width $c_0 W \approx 130$ nm. Therefore, the analysis of the Fourier spectra allows us to attribute the reduction in transmission to edge scattering.

To further support the discussion above we perform transport simulations through a graphene nanoconstriction using the Green's function method discussed in section 2.6. We simulate a four-terminal device with a constriction geometry provided by the AFM image [see inset Fig.3.2(a)], however, with narrower lead regions [Fig.3.5(b)]. To obtain a numerically feasible problem size we scale down the constriction geometry by a factor of

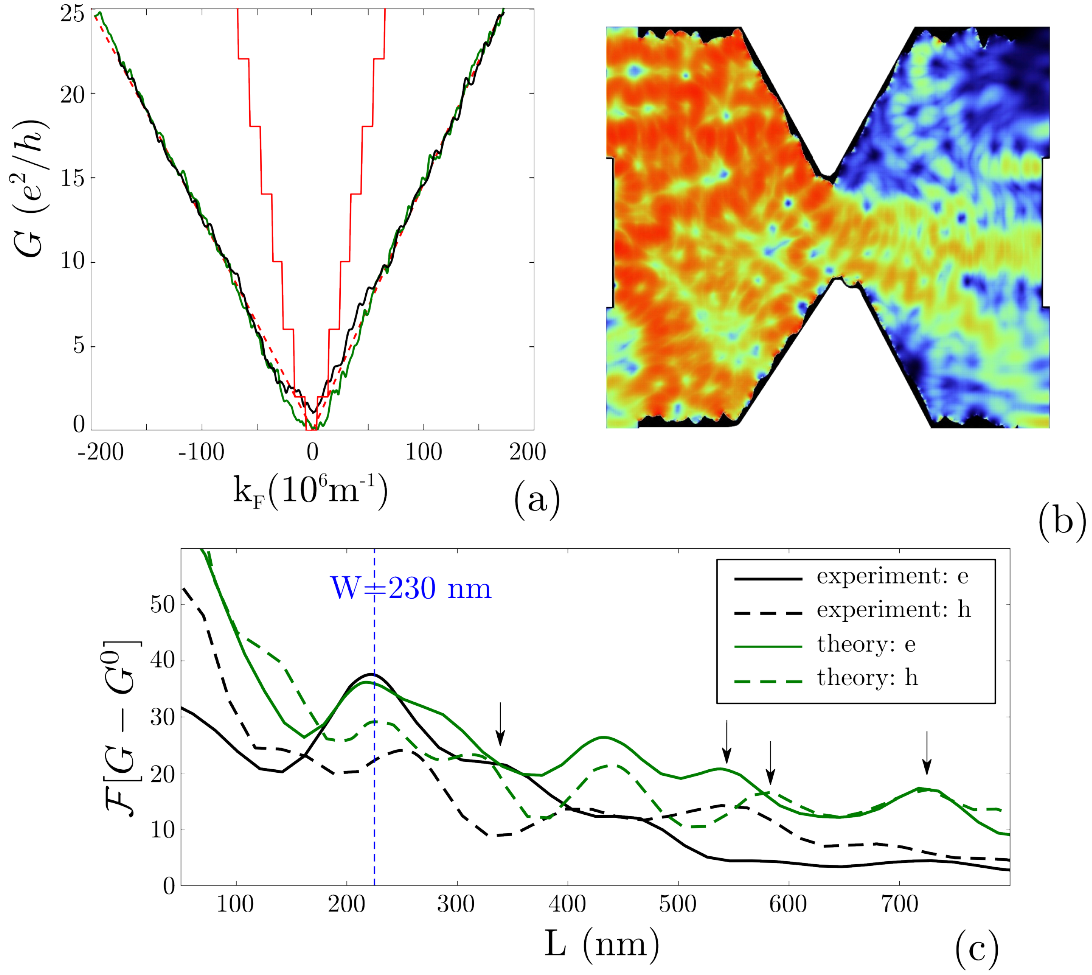

FIGURE 3.5: (a) Conductance as a function of k_F: experiment (black trace) versus theoretical calculations (green trace). Red steps follow the quantized conductance of an ideal zigzag graphene nanoribbon of the QPC width W. Red dashed lines correspond to the average conductance $G^{(0)}$ [Eq.(3.4)]. (b) An example of a wave function in the four-terminal geometry used for the transport calculations. (c) Fourier transform of the conductance signal away from the Dirac point for both experiment (black traces) and theory (green traces) evaluated separately for electron (solid traces) and hole (dashed traces) sides.

four. We also account for edge disorder with an amplitude of $0.2W$ in the range predicted for the experiment [Eq.(3.9)]. Theory and experiment show similar smooth, irregular modulations [compare green and black curves in Fig.3.5(a) corresponding to measured and calculated conductance]. The presence of these irregular modulations or ”kinks” in the conductance instead of sharp quantization steps reflects the strong scattering at the rough edges of the device. Our single-particle transport calculations include only elastic edge-disorder scattering but neglect other scattering mechanisms, e.g., electron-electron or electron-phonon scattering present in the experiment. Therefore, the good agreement between theory and experiment suggests that the edge scattering controls the formation of the ”kinks”. Furthermore, the Fourier analysis of the theoretical trace shows a pronounced peak at approximately 230 nm taking into account the scaling of the device size [see green curves in Fig.3.5(c)] correctly reproducing the position of the peak in the corresponding Fourier transform of the measured conductance [compare to black curves in Fig.3.5(c)]. In both theory and experiment this peak is more pronounced on the electron side than on the hole side [Fig.3.5(c)] due to the slightly asymmetric energy distribution of the trapped states [see Fig.3.3(c) and Fig.3.4(c)]. Although we included the same amount of disorder in our simulations, the harmonics in the experiment decay faster than predicted by theory. This effect can be attributed to the presence of decoherence or inelastic scattering processes in the real device, which are neglected in our model. Even though the higher Fourier components are suppressed, we observe harmonics at different length scales, which are not multiples of W, probably corresponding to the size quantization in the lead regions [e.g., see position of arrows in Fig.3.5(c)]. In addition, the scattering at the rough edges introduces a nonzero broadening to the otherwise sharp spectral lines [according to Eq.(3.3)]. As a result, the edge-disorder scattering is strong enough to destroy the quantization steps in the conductance signal.

Bias spectroscopy measurements [Fig.3.6(a)], i.e. conductance measurements as a function of source-drain voltage for different back gate voltages in a range from 0.5 V to 4.6 V in steps of 30 mV, offer a way to estimate the energy scale of the size quantization. The energy difference between the adjacent subbands $\Delta E = E_i - E_{i-1}$ is directly given by the bias voltage range where the plateaus or "kinks" [dense regions in Fig.3.6(a)] disappear and is about ≈14 eV. We can estimate the Fermi velocity v_F near the Dirac point using the energy of first few subbands given by Eq.(2.32) as

$$v_F = \frac{W\Delta E}{\pi\hbar}. \tag{3.14}$$

Taking the geometrical width $W = 230$ nm we estimate $v_F \approx 1.6 \cdot 10^6$ m/s, which is significantly larger than in bulk graphene. This is a signature of the Fermi velocity renormalization near the charge neutrality point in graphene nanodevices related to electron-electron interactions [29]. Moreover, the extracted energy scales are consistent with the weak temperature dependence of the quantized conductance [see arrows in Fig.3.6(b)].

3.3 Quantum transport in graphene nanoribbons in the presence of a perpendicular magnetic field

We now move to the investigation of quantum transport through graphene nanoribbons in the presence of a perpendicular magnetic field. We then apply the results of this

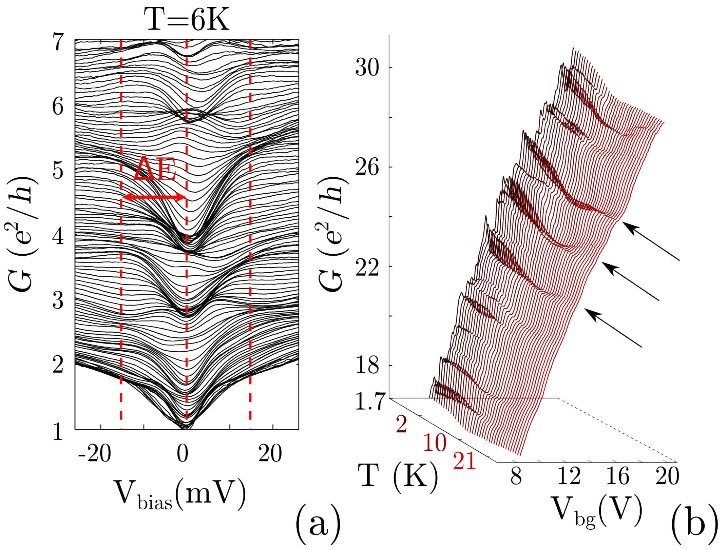

FIGURE 3.6: (a) Conductance as function of bias voltage V_{bias} at $B = 0$ T and $T = 6$ K. Each line resolves V_{bg} voltage in a range from 0.5 V to 4.6 V in steps of 30 mV. (b) Conductance traces as function of temperature and V_{bg}. (Adapted from [27])

section to the measured magnetic field evolution of the conductance through graphene QPC. Consider an ideal 50 nm wide zigzag graphene nanoribbon (ZGNR) in a perpendicular magnetic field. Our tight-binding calculation demonstrates a step-like quantized conductance [Fig.3.7(a)]. All the steps have a height of $2e^2/h$ due to the valley degeneracy, except for the nondegenerate edge state of ZGNR, which contributes e^2/h to the conductance (we do not include the physical spin degree of freedom which would double the conductance) in line with bandstructure calculations [see subsection 2.5.1]. The evolution of the quantization steps with the magnetic field can be traced by evaluating the first derivative of the conductance with respect to the electron energy $G_E = \partial G/\partial E$ [Fig.3.7(b)]. The derivative is non-zero only at the onset of steps, which corresponds to the opening of new propagating channels in the ribbon as a function of energy and field. As we discuss in subsection 2.5.1, we observe size quantization of the ribbon at $B \to 0$, which evolves to Landau levels at higher fields [see black dashed parabolas following Landau level quantization in Fig.3.7(b) and its insert which coincide with non-zero values of G_E at high fields]. Each Landau level N contributes to the transport through the coupling to the edges, which becomes a dominant process at fields $B \gtrsim NB_{\text{crit}}$ [Eq.(2.53)]. We can estimate the onset of the quantum Hall regime (or of the Landau levels regime) in the GNR using a geometrical argument [Eq.(2.51) and Eq.(2.53)]: the effective Landau level state size determined by the magnetic length l_B should be smaller than the width of the ribbon W. To derive the onset on the E-B plane, we express the Landau level state index N from Eq.(2.41) as:

$$N = \frac{E^2}{2|e|\hbar v_F^2 B}, \tag{3.15}$$

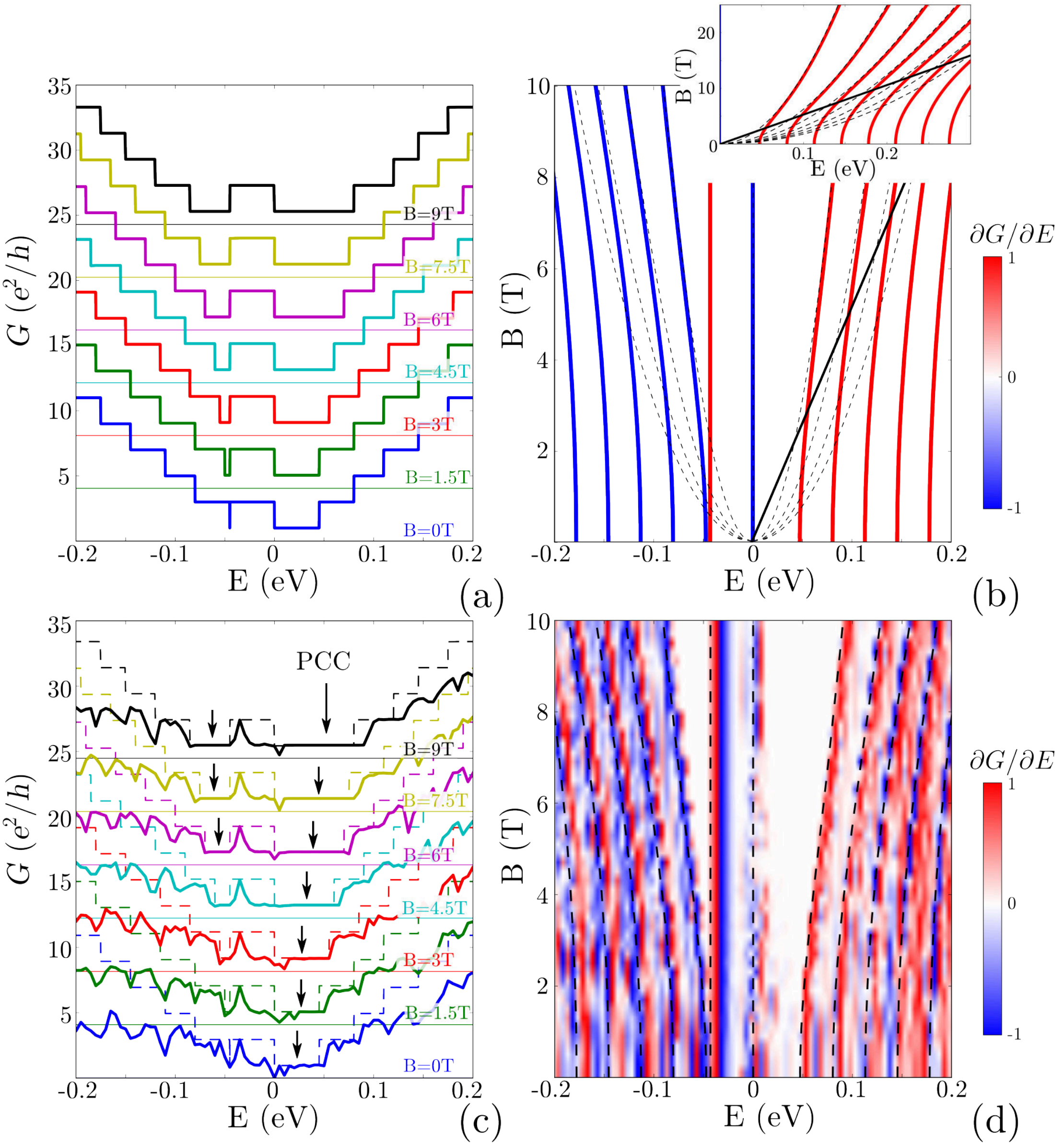

FIGURE 3.7: (a) Conductance and (b) its first derivative with respect to energy for a 50 nm wide ideal ZGNR in the presence of a perpendicular magnetic field. In (a) conductance traces at different magnetic fields are shifted for clarity. In (b) black dashed parabolas follow the Landau level quantization of Dirac fermions [Eq.(2.41)]; black solid line corresponds to the estimate of the onset of the quantum Hall regime in the ribbons $\tilde{E}(B)$ [Eq.(3.16)]; inset shows the evolution at higher B-fields. (c) Conductance and (d) its first derivative with respect to energy of a 50 nm wide and 50 nm long ZGNR in the presence of single vacancies with a density of $n = 1.2 \cdot 10^{-4}$ Å^{-2}. Dashed lines correspond to the conductance and the positions of maxima and minima of its first derivative for an ideal 50 nm wide ZGNR. Near the Dirac point conductance feature a perfectly conducting channel marked by arrows in (c).

and substitute it into Eq.(2.53). Consequently, the onset of Landau levels is at

$$\tilde{E} = \frac{W}{2} v_F e B. \tag{3.16}$$

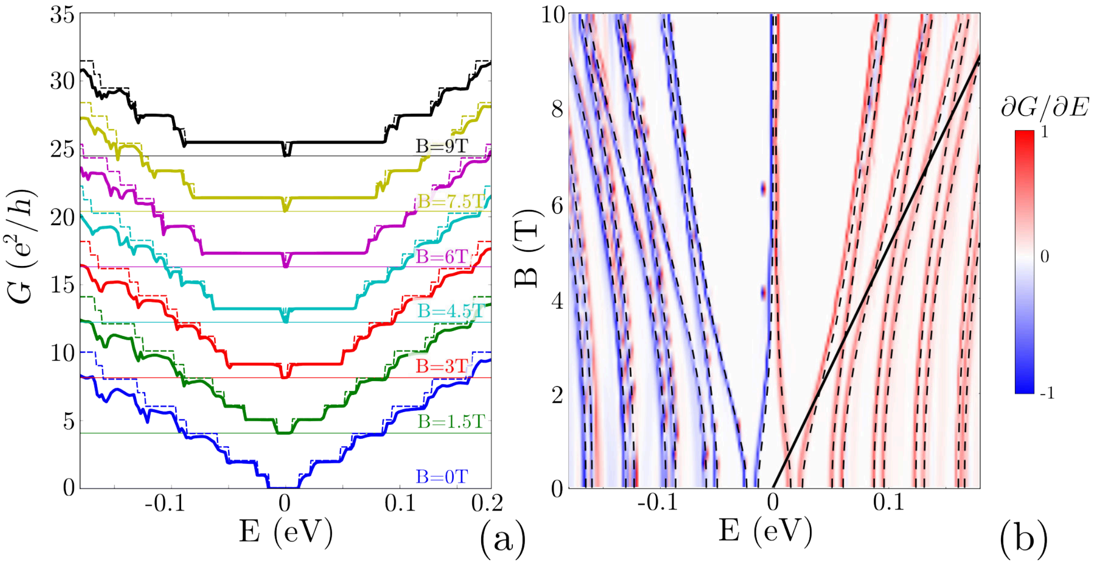

FIGURE 3.8: (a) Conductance and (b) its first derivative with respect to energy for a 40 nm wide and 50 nm long AGNR in a presence of the magnetic field and single vacancies with a density of $n = 1.2 \cdot 10^{-4}$ Å^{-2}. In (b) black solid line corresponds to the estimate of the onset of the Landau level quantization in the ribbons $\tilde{E}(B)$ [Eq.(3.16)]. Dashed lines correspond to the conductance and the positions of maxima and minima of its first derivative for an ideal 40 nm wide AGNR.

This simple estimate is in good agreement with our calculations [see black solid lines in Fig.3.7(b) and its inset]. At fixed B the quantization is a mixture of size and Landau level quantizations for E_F below $\tilde{E}(B)$.

To determine the effect of disorder on the conductance of ZGNR we introduce single vacancies by applying a large on-site potential at random lattice sites with a density of $n = 1.2 \cdot 10^{-4}$ Å^{-2} in a 50 nm long and 50 nm wide nanoribbon. The quantization steps in the conductance are destroyed by the strong back scattering [Fig.3.7(c)], which is a consequence of the strong K-K' scattering at the single vacancies in ZGNRs. However, steps emerge as the magnetic field increases, because propagating states become more confined to the edges of the device, and their spatial extent into the bulk decreases. As a result, at high fields the edge states are only weakly perturbed by bulk disorder. By contrast, the presence of rough edges destroys the steps even at high fields. Interestingly, there is a state near the Dirac point, which contributes to the conductance of e^2/h with increasing magnetic field even if the edge is rough [see marked by arrow plateaus in Fig.3.7(c)]. This conducting channel, which is also called perfectly conducting channel (PCC) [67, 68], is formed by the edge band of ZGNR [see Fig.2.6(a)]. The PCC was theoretically discussed in [67, 68] for ZGNRs with long-range disorder at $B = 0$. It exists for the following reason. The edge band of ZGNR is shared by both (K and K') valleys [see Fig.2.6(a) at B=0T] in contrast to other quantized subbands. Near the K valley the edge state contributes to a left-going mode (negative group velocity), whereas near the

K' valley it contributes to a right-going mode (positive group velocity). Since near each valley only one (edge) mode with well-defined moving direction exist, this edge state is robust to any kind of disorder, which does not induce intervalley scattering. In all other subbands each valley has both right- and left-moving states, which allows also for intravalley scattering. Therefore, at B=0T the edge state survives in contrast to higher subbands if only long-range disorder is present. However, the edge state can be destroyed by short-range disorder, which enhances the K-K' valley scattering. In other words the left- and right-going edge states belonging to opposite edges of the ribbon become coupled through the short-range disorder scattering. For increasing magnetic field, the coupling between the states propagating along the different edges (or near the different valleys) decreases suppressing intervalley scattering. Essentially, if an electron belonging to an edge band and moving along one edge would scatter off an impurity, it would be pushed back to the same edge by the magnetic field. Therefore, the disorder-induced intervalley scattering between the states located at the opposite edges of the nanoribbon decreases for stronger magnetic fields, and the observation of the PCC becomes possible again even in the presence of short range bulk and edge disorder [see plateaus marked by arrows near the Dirac point in Fig.3.7(c)].

Even though the conductance does not show clear steps and for low fields the steps are even untraceable, its first derivative G_E [Fig.3.7(d)] demonstrates a characteristic evolution of states in agreement with G_E of an ideal ribbon [see Fig.3.7(b) and black dashed line in Fig.3.7(d)]. This means that even in systems with irregular behavior of conductance, the parametric magnetic field evolution of the conductance can provide an additional insight on the size quantization in the system.

Remarkably, single vacancies do not have such a substantial impact on the electron transport through armchair graphene nanoribbons (AGNR). In particular, our calculations for a 40 nm wide and 50 nm long nanoribbon show that the quantization steps can be observed even at small magnetic fields [Fig.3.8(a)]. Moreover, the first derivative G_E [Fig.3.8(b)] shows a well-pronounced evolution of the quantized states in the ribbon as a function of energy and magnetic field, which coincides with the evolution of states in an ideal AGNR [black dashed curves in Fig.3.8(b)]. This effect can be explained with the help of the bandstructure [see Fig.2.6(b)]. The conducting electrons in AGNRs in both Dirac cones have momenta in the propagating direction (k_x) near zero, i.e. Γ point, and, therefore, have large wave lengths. The short-range disorder producing high Fourier components in k space does not induce the scattering between the cones located at the same point in k_x in contrast to ZGNRs with well separated K and K' cones. As a result, the electrons in AGNRs are only weakly perturbed by the atomically sharp disorder. The behavior of AGNRs and ZGNRs is, therefore, qualitatively similar to the respective behavior of a 2D electron gas and Dirac fermions in quantum point contacts discussed in the previous section.

Another interesting feature of AGNRs is the evolution of the quantized states with the B-field. In ZGNRs each quantum state is valley degenerate except for the zigzag edge state, which evolves to the zeroth Landau level upon the application of a magnetic field. Each non-zero valley degenerate Landau level, therefore, emerges from a single size quantization state. In AGNRs the valley degeneracy is weakly lifted and the edge band is missing. As a result, the zeroth Landau level at $E = 0$ is formed from the two lowest size quantization states from the electron and the hole sides corresponding to two different valleys in attempt to restore the valley degeneracy of the zeroth Landau level. Analogously, all other non-zero Landau levels are formed from the two neighboring size quantized states corresponding to different valleys [see Fig.3.8(b)].

3.4 Graphene quantum point contact in the presence of a perpendicular magnetic field

As we observed for GNRs, the magnetic field evolution of the conductance contains the signatures of conductance quantization even in the presence of disorder. Coming back to the conductance measurements in quantum point contacts, we can probe the parametric evolution of the observed ”kinks” with the magnetic field to further confirm their origin [Fig.3.9(a)]. The first derivative $G_V = \partial G/\partial V_{\rm bg}$ and the second derivative $G_{VB} = \partial^2 G/\partial V_{\rm bg}\partial B$ of the measured conductance show traces of the transition from size quantization to Landau level quantization [Fig.3.9(b,c)]. In particular, we observe that ”kinks” directly evolve to the Landau levels with increasing field strength. We theoretically estimate the observed magnetic field evolution of the conductance quantization by performing bandstructure calculations of a 230 nm (to be consistent with the extracted from SEM geometrical size W) wide zigzag nanoribbon without adjustable parameters. The transmission increases each time a new quantized band becomes energetically available for conducting electrons with increasing energy. We, therefore, calculate the energy minimum of each band as a function of magnetic field. The estimate we obtain [black solid curves in Fig.3.9(b,c,d)] follows the states' evolution in the experiment [maxima of G_V or G_{VB} in Fig.3.9(b,c,d)]. The onset of the quantum Hall regime [Eq.(3.16)] coincides with the estimate derived for the ribbons [see black dashed curve in Fig.3.9(b,c)]. At higher fields the Landau levels are distinct, whereas for lower fields on top of the magnetic evolution of the subbands more complex structures emerge. We notice a slight tilt of the additional structures [marked by black circles in Fig.3.9(d)], which is consistent with bulk Landau level quantization. However, in this energy window the states in the constriction are still strongly influenced by boundaries and we do not expect pure Landau levels to form. Therefore, we assign these additional patterns to Landau levels formed in the wider contact regions of the device. According to Eq.(3.16), for wider ribbons Landau levels are formed at lower magnetic fields. The minima of subbands in our bandstructure calculations for a 640 nm wide nanoribbon agree well with the trends of the additional structures [see black dashed curves in Fig.3.9(d)]. The details of the pattern are governed by avoided crossings between the bulk Landau levels of the wide contract areas and the subbands due to size-quantization in the constriction.

To conclude, magnetic field resolved measurements and their analysis allow us to support our notion of the conductance "kinks" observed at $B = 0$ being the signatures of size quantization of the constriction. We also observe that other length scales can influence the transmission leading to complex irregular structures on top of the simple evolution of the quantization at the quantum point contact. This finding is in line with our Fourier analysis of the $B = 0$ traces, where we observed harmonics at lengths different from $W = 230$ nm.

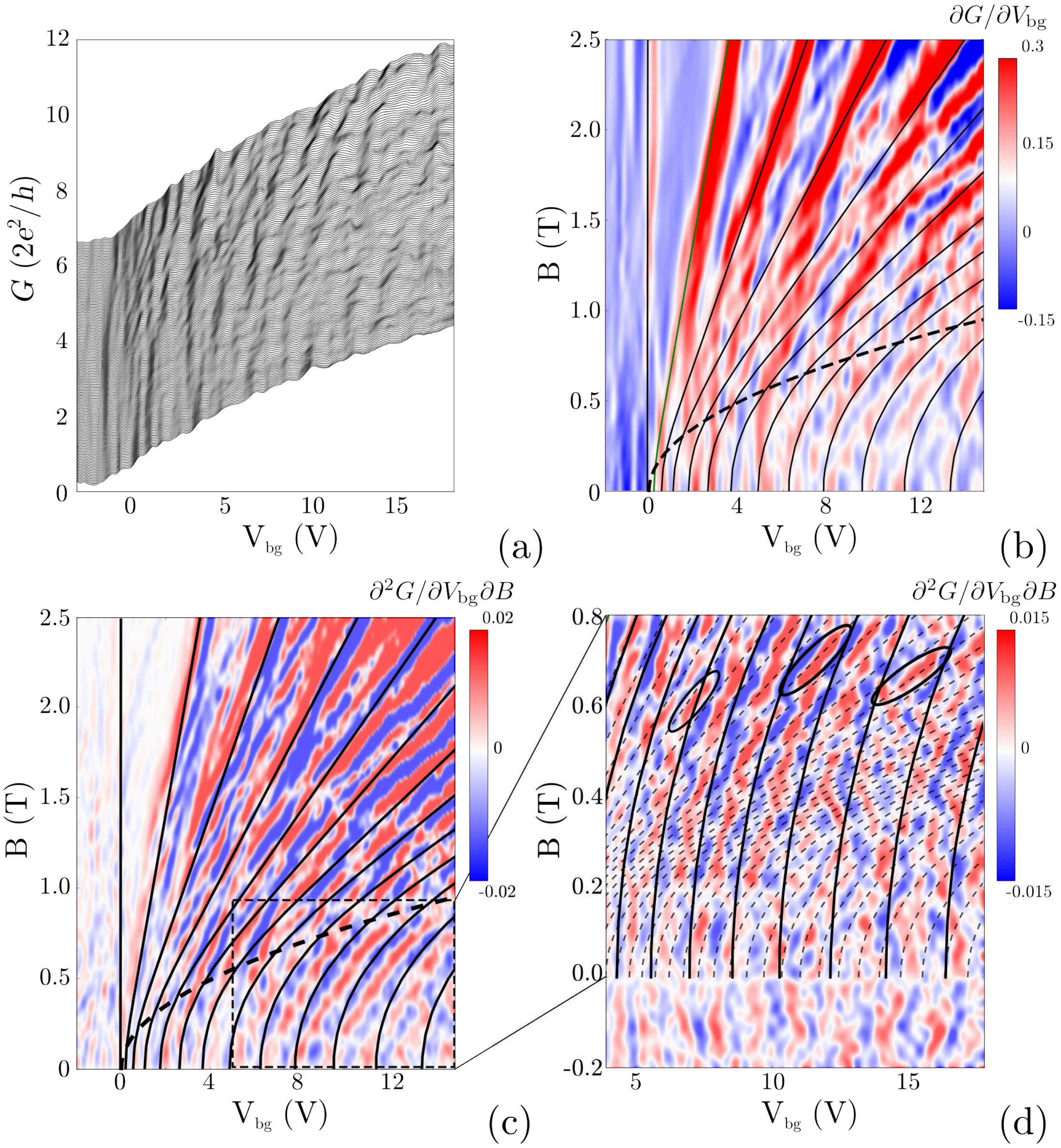

FIGURE 3.9: (a) The measured conductance through a graphene quantum point contact as a function of back gate voltage in the presence of the magnetic field. The conductance traces at different magnetic fields are shifted for clarity. (b,c) First G_V and second G_{VB} derivatives of the conductance traces in (a). (d) Close up of G_{VB} shown in (c). (b-d) The black solid curves correspond to the calculated magnetic field evolution of the subbands minima in the bandstructure of a 250 nm wide ZGNR. (b-c) The black dashed curves mark the onset of the quantum Hall regime in the QPC [Eq.(3.16)]. The black dashed lines in (d) follow the calculated magnetic field evolution of the subbands minima in the bandstructure of a 640 nm wide ZGNR, which enters the Landau level regime at fields where the QPC still exhibits the intermediate mixture of size and Landau level quantizations. The modulations (for example, marked by black circles) on top of the quantized conductance of the QPC are governed by the Landau levels formed outside of the QPC region.

Chapter 4

Graphene on hexagonal boron nitride

To achieve a high mobility of charge carriers in graphene it is necessary to reduce substrate induced disorder. In comparison to the conventional SiO_2 substrate, new substrates such as a hexagonal boron nitride (hBN) [13, 14] - a wide band gap insulator, dramatically improve the electronic and transport properties of graphene. Using hBN-graphene sandwich structures made the observation of size quantization of spatially confined electrons feasible [see chapter 3]. Graphene on clean transition metal surfaces (e.g., iridium (Ir) [69, 70] or ruthenium [71]) or on graphite [72] has also been shown to feature reduced disorder [73, 74].

However, the substrate can substantially modify the physical properties of graphene itself. For example, perfectly aligned graphene on hBN reveals a periodic superlattice, or so-called moiré pattern, due to the small lattice mismatch between the two materials [13, 14, 16]. This superlattice induces an additional periodic potential on a scale much larger than the lattice periodicity of graphene through the van der Waals type graphene-substrate interaction. The moiré pattern of graphene on hBN with an alignment angle $\phi = 0^\circ$ has a periodicity $a^S = 13.8$ nm ($a^S/a \gtrsim 50$, where a is the periodicity of graphene lattice). Moiré patterns were also observed in graphene with a grid of electron-beam deposited adatoms [75, 76] and in twisted bilayer graphene due to the misalignment between the layers [77, 78]. The presence of a new length scale induces new properties to the graphene devices [75]. In particular, the superlattice potential caused by hBN leads to the opening of a gap at the Dirac cone and Brillouin zone folding resulting in additional satellite band gaps energetically above and below the main Dirac cone. Note, however, that the graphene-hBN sandwich devices discussed in the previous chapter were not aligned, which allowed us to neglect the modification of the graphene Brillouin zone and bandstructure due to the substrate.

In the presence of a perpendicular magnetic field, the large superlattice unit cell allows for one entire magnetic flux quantum $\Phi = h/e$ passing through the supercell at laboratory magnetic field strength of the order of twenty Tesla. Consequently, the observation of fractal Hofstadter butterfly structures on top of each Landau level becomes possible [17–19]. These structures have been inaccessible in pristine graphene due to the small unit cell size (of ≈ 2 Å), which would require unrealistically large magnetic fields. The satellite band gaps evolve into secondary Landau level satellite structures as a function of perpendicular magnetic field. In the experiment [17–19], the satellites were attributed to additional Dirac-cones caused by the moiré pattern of the superlattice. However, a zeroth Landau level, the hallmark of Dirac-like Landau level structures [46] is clearly missing [18, 19].

In this chapter we simulate large-scale graphene nanoflakes interacting with an hBN substrate [Fig. 4.1]. The moiré pattern is included through the effective potential with parameters based on recent ab-initio DFT calculations [79, 80]. We benchmark our description by reproducing characteristic features of graphene on hBN in a magnetic field, i.e. the Hofstadter butterfly [81, 82] as well as the experimentally observed satellite structures [17, 19]. Our density of states and bandstructure calculations suggest that these satellites are caused by parabolic extremal points in the bandstructure giving rise to Schrödinger-like Landau levels rather than replica of Dirac cones. It appears that interpretation of the satellites as secondary Dirac points [83] is an artifact of measuring as function of back gate voltage: both Dirac- and Schrödinger-like dispersion relations give rise to linear Landau level structures when plotted as a function of V_{bg}. The distinguishing feature turns out to be the presence (or absence) of a zeroth Landau level. We show that only when employing an unrealistically strong superlattice potential true Dirac-cone like satellite structures, that include a zeroth Landau level, emerge close to the main Dirac point. We also demonstrate that the magneto-optical response of the graphene flakes subject to an effective hBN potential can provide energy resolved information on the electronic structure in the experiment. It can be used for probing the energy dependence of Landau levels of the satellites. In addition we include magneto-excitonic effects, which provide an explanation for the recently observed Landau-level dependent renormalization of the Fermi velocity [15, 28, 84, 85].

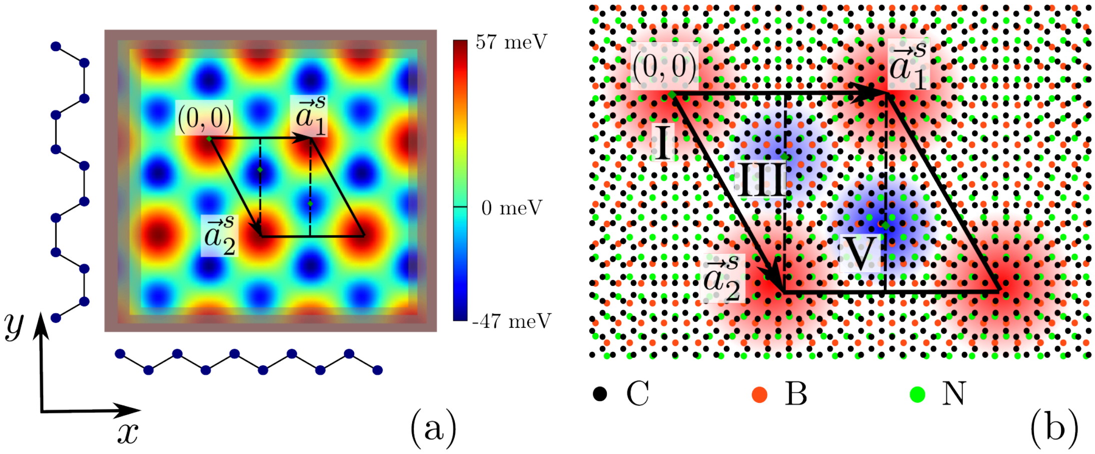

FIGURE 4.1: (a) Schematic view of a graphene flake with the superlattice potential landscape. (b) Superlattice unit cell for graphene on hBN with carbon (black), boron (orange) and nitrogen (green) atoms. We follow the numbering of areas with different chemical composition, i.e. *I* (red), *III* and *V* (blue), from Ref. [79]

4.1 Graphene Model Hamiltonian

We first aim to construct a model Hamiltonian of graphene with an additional periodic potential due to hBN. The effective Dirac Hamiltonian for a four-component spinor [Eq.(2.14)] in the presence of the homogeneous magnetic field $\vec{B} = \vec{\nabla} \times \vec{A}$ perpendicular to the graphene plane as well as an external electrostatic potential reads

$$\begin{aligned} H_D = v_F \vec{\sigma} \cdot (\hat{\vec{p}} - \frac{e}{c}\vec{A}) \otimes \tau_1 + v_F \vec{\sigma}^* \cdot (\hat{\vec{p}} - \frac{e}{c}\vec{A}) \otimes \tau_2 \\ + V(\vec{r}) \cdot \mathbb{1} \otimes \tau_0 + W(\vec{r}) \cdot \sigma_z \otimes \tau_0. \end{aligned} \tag{4.1}$$

In Eq. (4.1) we have distinguished two different classes of potentials: (1) the slowly varying potential $V(\vec{r})$ (represented by a $\mathbb{1}$ in sublattice space) breaking the particle-hole symmetry; and (2) the short range potential $W(\vec{r})$ (represented by σ_z in sublattice space) breaking sublattice symmetry. $W(\vec{r})$ introduces a finite "mass" and, therefore, a band gap at the Dirac point [86]. A wide variety of substrate effects can be effectively modeled by these two potentials.

Graphene on a hBN substrate features a moiré pattern with $a^S = 13.8$ nm periodicity for $\phi \approx 0°$ alignment. The resulting hexagonal superlattice vectors are $\vec{a}_1^S = (13.8, 0)$ nm and $\vec{a}_2^S = (6.9, 11.9)$ nm [see Fig. 4.1(b)]. The supercell has three main regions with different local alignment of the graphene and hBN top layer [here, we follow the numbering from Ref. [79], see also labels in Fig. 4.1(b)]: (*I*) the carbon atoms of one sublattice A are on top of boron and the carbon atoms of the other sublattice B on top of nitrogen; (*III*) the carbon atoms of A on top of the nitrogen atoms and the atoms of B are in the middle of a hBN hexagon; (*V*) the carbon atoms of A are on top of boron atoms while now the B atoms are located off the hBN hexagons. The regions (II) and (IV) feature intermediate stacking.

We obtain the realistic potential parameters from recent ab-initio DFT calculations discussed in [79, 80]. These ab-initio studies reveal sublattice symmetry breaking potentials $W(\vec{r})$ which feature broad maxima and minima at the centers of the regions I, III and V. We therefore expand $W(\vec{r})$ in Gaussians centered in these three main regions according to

$$W(\vec{r}) = \sum_{i=I,III,V} W_i \exp\left(-\frac{(\vec{r}-\vec{R}_i)^2}{2w_i^2}\right) \tag{4.2}$$

with amplitudes $W_I = 57$ meV, $W_{III} = -34$ meV, $W_V = -47$ meV taken from Sachs et al. [79] and widths $0.63 \cdot w_I = w_{III} = w_V = 7$ nm from geometrical considerations. Local doping by, e.g., charge traps may lead to further local potential variations in the experiment. The potential $W(\vec{r})$ opens a band gap near the Dirac point, which modifies the Landau levels according to Eq.(2.44). These spectrum reveals two zeroth Landau levels with energies $E^D_{\pm 0} = \pm E_g/2$, which correspond to the lifting of the valley degeneracy.

The experimental data, however, also reveals a pronounced electron-hole asymmetry between the electron and hole satellites [18]. Note that the Dirac picture we consider here is electron-hole symmetric and the electron-hole asymmetry in the third-nearest-neighbor tight-binding approximation, which we use for the DOS calculations, is too weak to explain the experiment. Therefore, it is the graphene-substrate interaction described by the potential $V(\vec{r})$, which breaks the electron-hole symmetry. This potential, however, is difficult to determine from ab-initio calculations. DFT calculations of the adhesion energy of graphene on hBN predict 20 meV stronger binding in region V compared to the other regions [79]. As we verified numerically, this value is too small to explain the experimental observations. From second-order perturbation theory Yankowitz et al. [16] estimate the variation of $V(\vec{r})$ to be of the order of 120 meV. We account for the stronger binding in region V by a potential $V(\vec{r})$, which we approximate by a Gaussian [similar to Eq.(4.2)] as

$$V(\vec{r}) = V_V \exp\left(-\frac{(\vec{r}-\vec{R}_i)^2}{2w_V^2}\right) \tag{4.3}$$

with the amplitude $V_V \approx -100$ meV corresponding to a potential minimum at the site of the strongest adhesion.

The potential $W(\vec{r})$ lifts the valley degeneracy but does not affect physical spin. The experiment, however, indicates a complete lifting of the four-fold degeneracy of the zeroth Landau level. The Zeeman contribution [Eq.(2.45)] splits the spin degree of freedom. However, the measurements of quantum Hall states as a function of magnetic field [87] suggest an enhanced effective gyromagnetic ratio compare to the gyromagnetic ratio for graphene $g_0 = 2$ due to many-body interactions. Furthermore, a linear increase of valley splitting Δ_V with magnetic field is measured. This effect is attributed to the exchange interaction related to the energy cost of a spin reversal relative to adjacent (polarized) spins [87]. The magnetic field dependence of Δ_V related to many-body interactions is currently not fully understood theoretically. Two alternative theoretical models have been previously proposed to explain this observation. (i) One model, based on the continuous Dirac model in the Hartree-Fock approximation, predicts a $\sqrt{B}$ scaling of the valley splitting [88, 89]. While this scaling differs from the linear scaling observed in experiment, the resulting numerical values for the valley splitting resemble those of the experiment within the range of investigated magnetic field strengths. (ii) The second model, based on the effect of lattice distortion and the interaction with the substrate, predicts linear scaling of valley splitting with B but underestimates the strength of the splitting by an order of magnitude [90]. We account for this valley splitting within our single-particle description by adding a phenomenological correction

$$W_{\mathrm{MB}}(\vec{r}) = \alpha \cdot B e^{-r^2/2w_I^2}, \tag{4.4}$$

to the potential $W(\vec{r})$ that scales linearly in B with $\alpha = 8$ meV/T in accord with the experiment [87]. The spin splitting is included through the Zeeman effect [Eq.(2.45)] with the enhanced gyromagnetic ratio g_{eff}.

4.2 Hofstadter Butterfly

In 1976 Hofstadter [82] showed that Bloch electrons on a 2D square lattice subject to a perpendicular magnetic field acquire a fractal pattern in the Landau level energy spectrum as function of magnetic field field. The solution of Harper's equation, which was used as a model to describe the behavior of electrons, reveal a competition of two length scales: the lattice periodicity and the magnetic periodicity due to the circular motion of electrons in the magnetic field. When the two length scales are commensurate, a regularly repeating structure develops on top of each Landau level. In other words, when the ratio of magnetic flux Φ through the area A of one unit cell of the spatially periodic lattice [81, 82, 91] to the magnetic flux quantum $\Phi_0 = h/e$ is a rational number

$$\frac{\Phi}{\Phi_0} = \frac{p}{q}, \text{ where } \{p, q\} \in \mathbb{Z}, \tag{4.5}$$

each Landau level splits into q bands which are p-fold degenerate. Hofstadter [82] also noted that the observation of the calculated spectrum experimentally using a crystal lattice with periodicity of ≈ 2 Å is not feasible, as it would require magnetic fields of up to 10^4 T. However, the large scale superlattice moiré potential should allow for the observation of the effect.

Graphene, as a 2D material, is a prime candidate for the experimental observation of the Hofstadter butterfly. Indeed, the experiments of graphene on a flat hBN with a periodic superlattice of 14 nm already demonstrate the Hofstadter butterfly spectrum in laboratory accessible magnetic fields of up to 30-40 T [17–19]. The magnetic flux ratio for the hexagonal moiré superlattice $\Phi/\Phi_0 = BAe/h$ equal unity at $B = 25$T. Three experiments [17–19] confirmed the theoretical prediction by Hofstadter [82] independently using different techniques: (1) magnetocapacitance measurements [18]; (2) magnetotransport measurements [19]; and (3) quantum Hall state measurements [17].

4.3 DOS and bandstructure simulations

The density of states (DOS) calculations of large size graphene flakes within the tight-binding approach is a good approximation of the DOS of bulk graphene. The method is very useful for situations, where sophisticated techniques mainly based on periodic boundary conditions (e.g., density functional theory) are computationally difficult or not applicable, for example, due to the presence of a magnetic field or an additional large-scale potential: superlattice or charge puddles. We simulate the magnetic response of a finite-sized patch of graphene with dimensions $L_x \times L_y = 170 \times 130$ nm^2 [see Fig. 4.1(a)] using the third-nearest-neighbor tight-binding approximation [see 2.3]. The hBN substrate and many-particle effects are included through the potentials of Eqs.(4.2)-(4.4). The sublattice symmetry breaking potentials of $W(\vec{r})$ type affect sublattices A and B with opposite sign. To eliminate the edge effects at the flake boundary (i.e. localization at the zigzag edges), we include a repulsive Berry-Mondragon potential [86] of $W(\vec{r})$ type:

$$W_{\text{edge}} = W_0 \exp\left(-\Delta(\vec{r})/\Delta_0\right), \tag{4.6}$$

where $\Delta(\vec{r})$ is a distance to the edge, Δ_0 is the characteristic decay distance chosen to be much smaller compared to the size of the flake and W_0 is the amplitude at the edge of the graphene flake. The magnetic field is included by a Peierls phase factor [see section 2.5 and Eq.(2.46)], and we account for the Zeeman term by first-order perturbation theory.

Before discussing the density of states, we consider the unperturbed [Fig. 4.2(a)] and the superlattice-induced bandstructures [Fig. 4.2(b)-(e)]. The bandstructure calculations were performed for a square supercell with the moiré potential distribution depicted in Fig. 4.2(f) imposing periodic boundary conditions. Since we consider the same supercell for both perturbed and unperturbed ($V = W = 0$) calculations, the bandstructure is

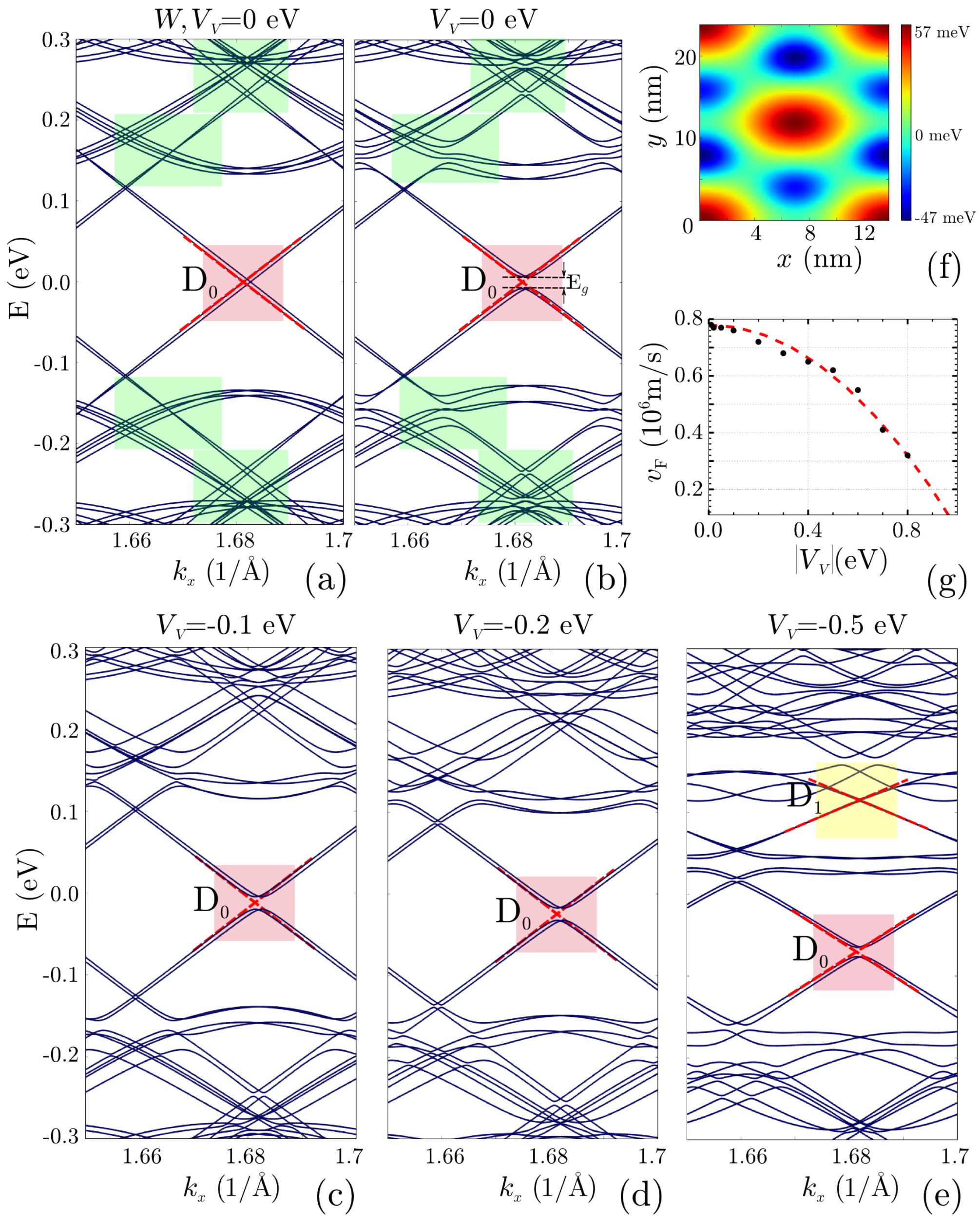

FIGURE 4.2: Cut through bandstructure ($k_y = 0$) of bulk graphene with periodic superlattice potential within the reduced zone structure of the superlattice calculated using third nearest-neighbor tight-binding: (a) $V = W = 0$ eV, i.e. pristine graphene, (b)-(e) $W_I = 57$ meV, $W_{III} = -34$ meV and $W_V = -47$ meV with varying V_V. The red dashed lines show a linear fit to the main Dirac cone D_0 (red regions) and to the secondary cone D_1 (yellow area) in (e), from which values of the Fermi velocity v_F are extracted. Green regions in (b) shows the formation of avoided crossings due to the moire potential, which are absent in (a). (f) Potential landscape of the supercell used in the bandstructure calculations. (g) The dependence of the Fermi velocity v_F of D_0 on the amplitude of the superlattice potential V_V.

displayed within the first Brillouin zone of the reciprocal supercell. In the unperturbed case, the parabolic bands [Fig.4.2(a)] correspond to cuts through back-folded off-center ($k_y \neq 0$) cones while the near-linear bands correspond to the main cone D_0 and its replica centered at $k_y = 0$. The substrate interaction $W(\vec{r})$ [Eq.(4.2)], as expected, opens a band gap at the main Dirac cone of $E_g = 15$ meV. Furthermore, the presence of an additional potential $W(\vec{r})$ induces a number of avoided crossings [green areas in Fig. 4.2(b)] which are absent in pristine graphene [green areas in Fig. 4.2(a)]. The additional long-range (particle-hole symmetry breaking) potential $V(\vec{r})$ [Eq.(4.3)] increases the size of the avoided crossings and shifts the position of the main Dirac cone D_0 relative to $E = 0$ eV [see the evolution of D_0 outlined by red areas in Fig. 4.2(c)-(e)]. The shift, to first order, is given by the average of the superlattice potential. The potential $V(\vec{r})$ also influences the effective Fermi velocity v_F of the main Dirac cone [D_0 is outlined by red areas in Fig. 4.2(a)-(e)]. v_F decreases with increasing amplitude V_V [Fig. 4.2(g)]. The tight-binding bandstructure calculations for pristine graphene yields a Fermi velocity of $v_F^0 = 0.78 \cdot 10^6$ m/s . With increasing $|V_V|$ the velocity v_F drops proportionally to the square of the amplitude of the on-site potential V_V, in agreement with second-order perturbation theory [92] which predicts a velocity renormalization

$$v_{F\vec{k}} = v_F^0 - \sum_{\vec{G}\neq 0} \frac{2\left|V(\vec{G})\right|^2}{v_F^0 \left|\vec{G}\right|} \sin^2 \theta_{\vec{k},\vec{G}}. \tag{4.7}$$

Here, $\vec{G}$ is the reciprocal lattice vector, $V(\vec{G})$ is the Fourier transform of the superlattice potential $V(\vec{r})$ [Eq.(4.2)], and $\theta_{\vec{k},\vec{G}}$ is the angle between $\vec{k}$ and $\vec{G}$.

Although we consider a perfectly aligned graphene on hBN with alignment angle $\phi = 0$, we note that for a finite alignment angle ϕ between graphene and hBN lattices, the periodicity of the moiré pattern is decreased, thereby increasing the size of the Brillouin zone in reciprocal space. Consequently, the additional bands due to the overlap between the main Dirac cone and its replica are located further away from the Dirac point.

We calculate the density of states of large graphene flakes on perfectly aligned hBN described by the additional potentials $W(\vec{r})$ [Eq.(4.2)], $V(\vec{r})$ [Eq.(4.3)] and $W_{\mathrm{MB}}(\vec{r})$ [Eq.(4.4)] using Arnoldi-Lanczos diagonalization. We first present the DOS for a realistic value of $V_V = -0.1$ eV for the electron-hole symmetry breaking potential $V(\vec{r})$ in both the E-B plane [Fig. 4.3(a,d)] and the N-B plane [Fig. 4.3(b)], where N is the number of charge carriers in the quantum dot ($N \propto V_{\mathrm{bg}}$ within a linear capacitance model discussed in section 2.7). For the transformation from energy to charge carrier number we do not use the square root dependence $E \sim \sqrt{N}$ for bulk graphene but sum over the actual number of eigenstates (or charge) of the finite size flake between the Dirac cone and the corresponding Fermi energy E_F, to accurately account for deviations from the linear DOS close to the Dirac point.

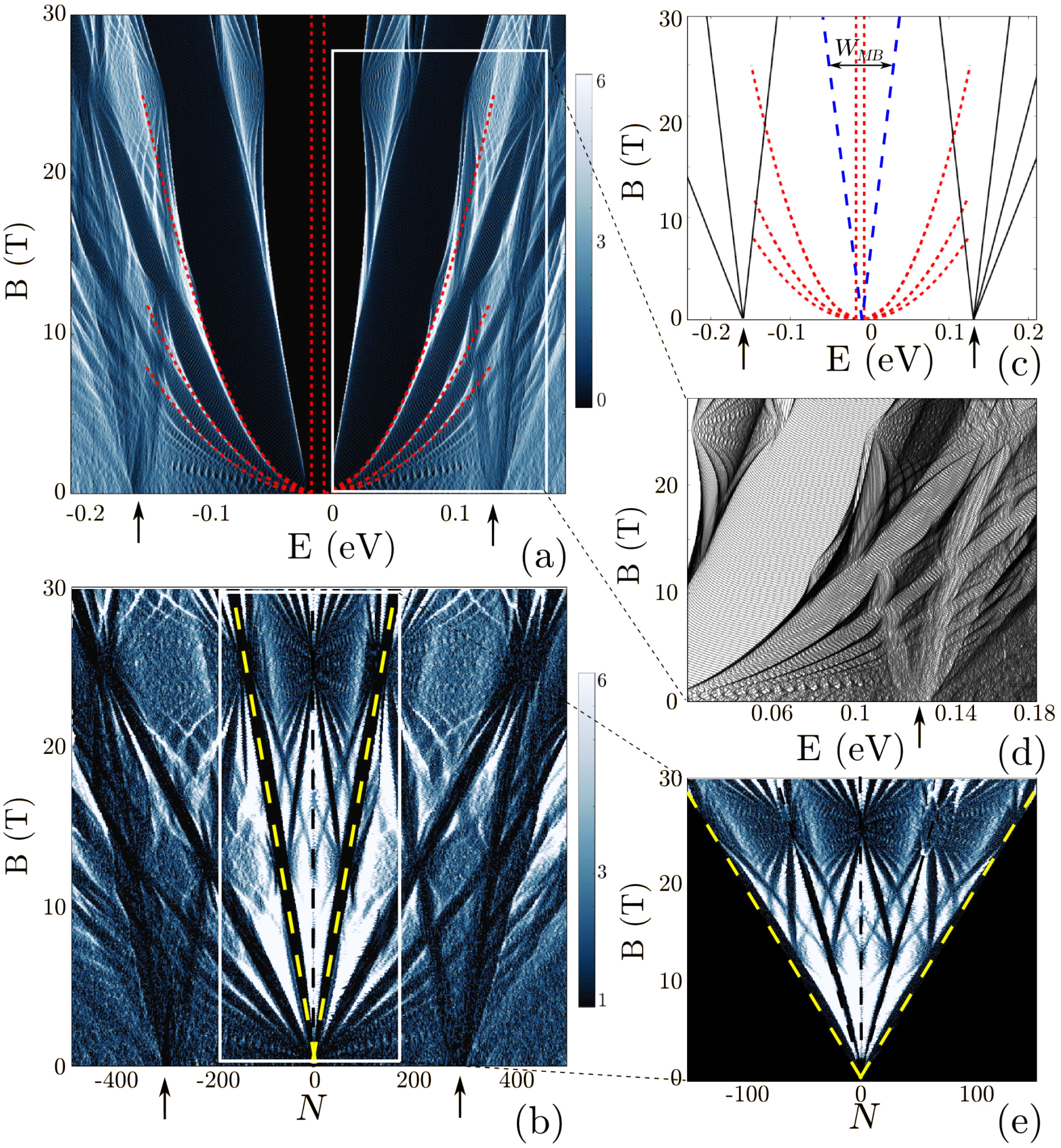

FIGURE 4.3: Density of states of a graphene flake in the presence of a superlattice potential ($V_V = -0.1$ eV): (a) as a function of electron energy and magnetic field; (b) same as (a) however as a function of the number of charge carriers N; (c) schematic plot of the important Landau level structures seen in (a): red dashed lines represent the Landau levels of the main Dirac cone including the energy gap $E_g = 15$ meV [see Fig. 4.2]; blue dashed lines denote the splitting of the zeroth Landau level due to W_{MB}; solid lines represent the Landau levels of the two Schrödinger-like satellites, whose origin is marked with black arrows in (a)-(d). (d) magnification of the area with the right satellite structure in (a). (e) four-fold splitting of the 0^{th} Landau level including W_{MB} and Zeeman term with an enhanced $g = 5$ due to electron-electron interaction [compare the area confined by yellow dashed lines in (b), where the Zeeman term is not included].

The calculated DOS displays the formation of Landau levels emanating from the Dirac point of the main cone D_0 [Fig. 4.3(a,c)]. The parabolic dependence [Eq. (2.44)] $B \sim E^2$ [see red dashed parabolas in Fig. 4.3(a) and the schematic plot in (c)] confirms a relativistic diamagnetic response behavior. Moreover, the curvature of the parabolas [Eq. (2.41)]

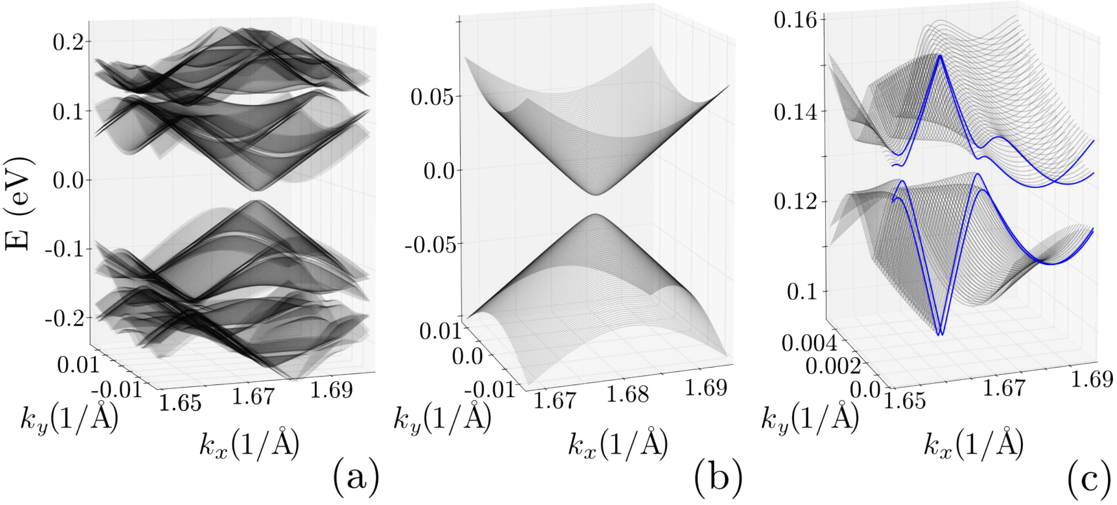

FIGURE 4.4: Two-dimensional zero-field ($B = 0$) bandstructure $E(k_x)$. (a) Near the main Dirac cone D_0 (see Fig.4.2(c)). (b) Bandstructure in the region of the satellite structure marked by the right arrow in Fig.4.3(a) and (c).

determined by the Fermi velocity $v_F^{\text{BN}} = 0.76 \cdot 10^6$ m/s extracted from the fit to the main Dirac cone in the bandstructure [red dashed lines in Fig.4.2(c)] agrees well with that of the simulated DOS. The zeroth Landau level splits linearly due to many-body correction [Eq. (4.4)]. We observe the substrate-induced Hofstadter spectrum [section 4.2] with a ”diamond”-like structures [81] [see close up of the structure in Fig. 4.3(d)] which is most pronounced at rational fractions of magnetic flux through a supercell to magnetic flux quantum Φ/Φ_0 [81, 91]. For the hexagonal superlattice with a period of $a^S = 13.8$ nm, this ratio equals one at $B_0 = 25.5$ T [see Fig. 4.3(a, d)]. Moreover, we observe two distinct satellites which evolve (approximately) linearly in the E-B plane emerging at $B = 0$ near $E = 0.13$ eV and -0.16 eV [marked by arrows in Fig. 4.3(a, c, d)]. These satellite structures clearly display a non-relativistic rather than a relativistic $E(B)$ dependence. A closer look into the $B = 0$ bandstructure near the satellites [Fig. 4.2(c)] reveals that they originate from a region with a parabolic rather than a linear $E(k)$ dispersion. At these energies, the 2D bandstructure $E(k_x, k_y)$ [Fig. 4.4(a), (c)] near the satellites does not show cone-like structures unlike the bandstructure near the main Dirac cone [Fig. 4.4(b)]. Consequently, the Landau levels show a Schrödinger-like rather than a Dirac-like [Eq. (2.41)] B-field dependence as a function of E_F. However, when plotted as a function of the charge carrier number N or, equivalently, as a function of V_{bg} a linear B-N (B-V_{bg}) dependence emerges [Fig. 4.3(b)] for both the main Dirac cone and the satellites. A simple capacitive coupling model [as discussed in section 2.7 and Eq.(2.74)] predicts a square-root relation between V_{bg} and E, i.e. $E \propto \sqrt{V_{\text{bg}}}$. Therefore, Eq. (2.41) predicts a linear V_{bg}-B relation for the relativistic Landau levels. Remarkably, the same holds for non-relativistic Schrödinger electrons since the non-relativistic

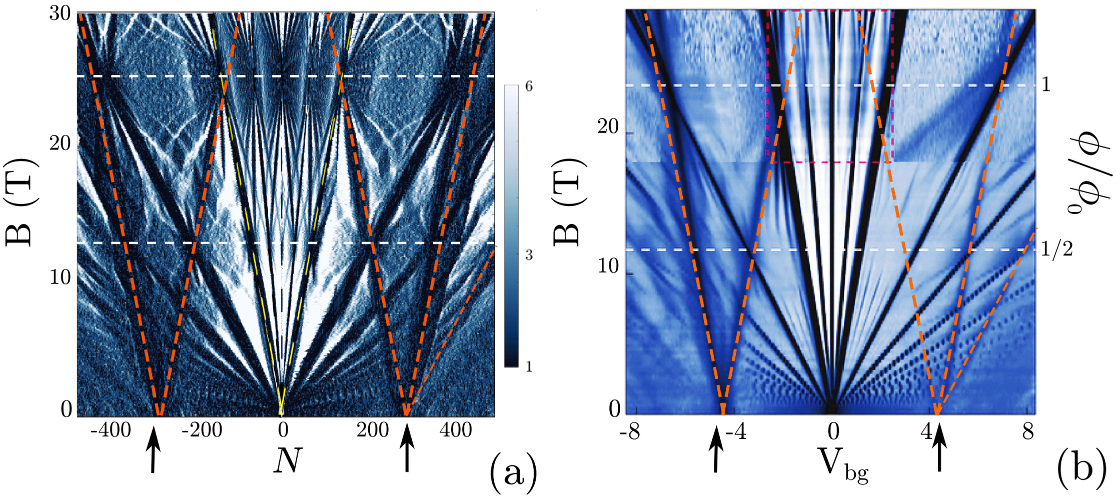

FIGURE 4.5: Calculated DOS (a) [combined Fig.4.3(b) and (e)] versus measured magnetocapacitance (b) [18]. The orange dashed lines The orange dashed lines follow Landau levels of satellites. These lines feature the same inclination for both theory and experiment.

density of states in $2D$ is energy independent, ρ_S =const, and $N \sim V_{\rm bg} \sim E$. Consequently, the linear relation between $V_{\rm bg}$ and B or, equivalently, $V_{\rm bg}$ and the charge carrier number N is found for both a Dirac-like and a Schrödinger-like spectrum.

The linear dependence for the satellites was observed in the experiment [18, 19] [see Fig.4.5(b) adapted from [18]] and was interpreted as the formation of Dirac Landau levels emerging from the satellites [83]. The satellites were, therefore, attributed to a Dirac cone replica. As discussed above, the linear behavior of Landau levels in the B-$V_{\rm bg}$ plane cannot be used to identify a Dirac cone or its replica. Instead, the distinctive feature is the presence or absence of the zeroth Landau level. Our DOS simulations with the chosen set of superlattice potential parameters agree very well with the measured magnetocapacitance [18] [compare Fig. 4.5(a) and (b)] in the B-N plane. In particular, the simulations demonstrate the linear Landau levels dependence on B emerged from the main Dirac point when viewed as a function of $V_{\rm bg}$ [see Fig. 4.5(a)] with the complex Hofstadter butterfly structures on top. The simulations correctly describe the zeroth Landau level splitting [Fig. 4.3(e); also included in Fig. 4.5(a)] when including the B-field dependent phenomenological many-body term $W_{\rm MB}$ lifting the valley degeneracy and the Zeeman term lifting the spin degeneracy with a strongly enhanced gyromagnetic ratio $g_{\rm eff} = 5$ [87]. In general, the effective g factor will be different for different Landau levels. Therefore, we do not discuss within our single-electron model the spin splitting of higher Landau levels. Our model also does not account for the valley splitting in the higher Landau states, as our effective many-body potential $W_{\rm MB}$ has negligible influence on energies far away from the Dirac point. Finally, we were able to reproduce the correct linear slopes of Landau levels of satellites. We, therefore, conclude, that the absence of

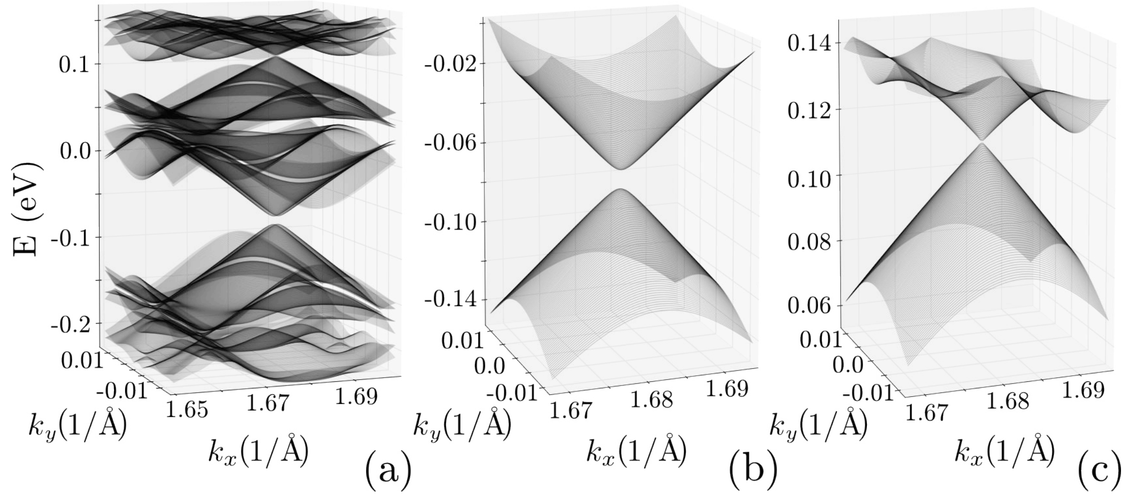

FIGURE 4.6: Two-dimensional bandstructure for graphene on hBN with an unrealistically enhanced strength $V_V = -0.5$ eV of superlattice on-site potential $V(\vec{r})$. (a) Primary Dirac cone D_0, (b) secondary Dirac cone D_1 (see Fig.4.2(e))

the 0^{th} Landau level and its Hofstadter butterfly for the satellites both in experiment and in our simulation, unambiguously confirms that the satellites are associated with a parabolic bandstructure rather than with a Dirac cone replica.

The origin of the non-relativistic dispersion can be easily traced to the unperturbed spectrum of bulk graphene [Fig. 4.2(a)]. The satellites emerge from parabolic bands with energies $|E| \approx 0.15$ eV above and below the Dirac point. Replica D_1 of the Dirac cone centered at $k_y = 0$ appears at much higher energies $|E| \gtrsim 0.28$ eV and are submerged in a region of high DOS. Accordingly, the superlattice potential resulting from the van der Waals interaction with the hBN substrate which is of the order $|V| \lesssim 0.1$ eV represents only a moderately weak perturbation of the parabolic bands giving rise to distortion and narrow avoided crossings but cannot significantly shift the distant Dirac cone into the region of low DOS and into the proximity of D_0. In turn, increasing the van der Waals interaction to an unrealistic strength with an on-site potential $V(\vec{r})$ [Eq.(4.3)] from $V_V = -0.1$ eV to $V_V = -0.5$ eV renders the replica D_1 of the Dirac cone visible near $E = 0.114$ eV [Fig. 4.6(a), (c) and D_1 is outlined by yellow area in Fig. 4.2(e)] in addition to the main cone D_0 at $E = -0.07$ eV [Fig. 4.6(b). We note that the main cone D_0 shows a finite gap of about 10 meV, while the replica cone appears gapless [compare Fig. 4.6 (b) and (c) for D_0 and D_1 cones]. The DOS in the B-E representation [Fig. 4.7(a)] and in the B-N representation [Fig. 4.7(b)] shows now two emerging Landau fans of relativistic dispersion with $B \sim E^2$ [in Fig. 4.7(a)] and $B \sim N$[in Fig. 4.7(b)]. The Fermi velocity of the main cone D_0 is now $v_F^{D_0} = 0.62 \cdot 10^6$ m/s, while we find $v_F^{D_1} = 0.39 \cdot 10^6$ m/s for the secondary cone D_1. The curvature of the parabolic Landau level states [Eq.(2.41)] determined by $v_F^{D_0}$ and $v_F^{D_1}$ again fits well to the DOS near both D_0 and D_1 [see red dashed parabolas in Fig. 4.7(a)]. The additional features emerging

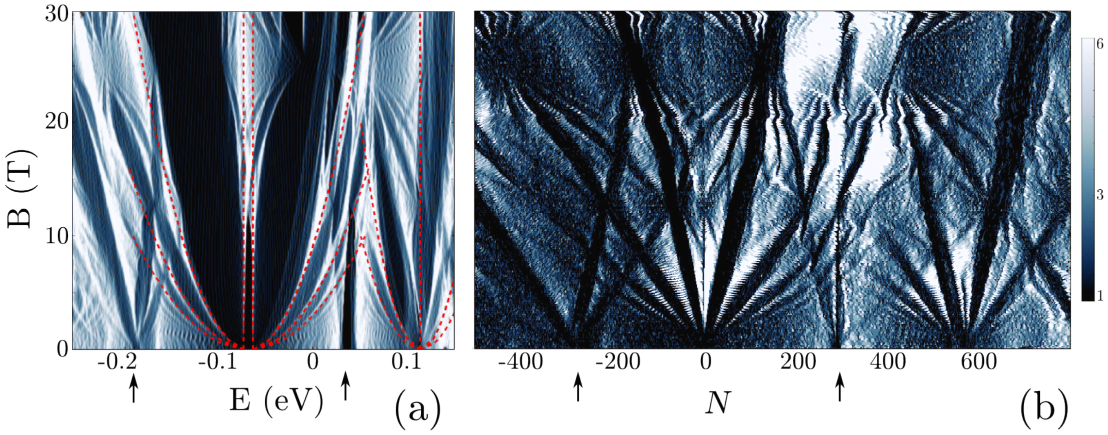

FIGURE 4.7: Density of states of a graphene flake on hBN however with an unrealistically large superlattice potential ($V_V = -0.5$ eV and $W_{\mathrm{MB}} = 0$): (a) in the B-E plane, as a function of magnetic field and electron energy; (b) in the B-N plane, as a function of magnetic field and number of charge carriers. Black arrows at $B = 0$ mark the same Schrödinger like satellites as in Fig. 4.3.

near $E = 0.03$ eV and $E = -0.19$ eV at $B = 0$ [see arrows in Fig. 4.7(a)] resulting from the regions of non-relativistic quasi-quadratic dispersion remain present for this much stronger superlattice potential. Thus, the coexistence in the spectrum of a Dirac-like and a Schrödinger-like diamagnetic response persists. As a function of back gate voltage, the satellite structures for relativistic and non-relativistic particles [Fig. 4.7(b)] are similar. However, as discussed above, they can be well distinguished by the presence of the zeroth Landau level for relativistic dispersion.

Another way to distinguish the two different dispersion relations is a direct energy dependent measurement. For example, magnetic field resolved STM measurements of the LDOS or measurements of the optical transitions within the satellite structures and within the Landau levels of the main cone [15] would yield data on their energy dependence. The magneto-optical response of graphene flakes with a superlattice potential is discussed in details in section 4.4.

We discuss now the behavior of the eigenfunctions of the graphene flakes with realistically moderate strength $V_V = -0.1$ eV of the on-site potential $V(\vec{r})$ [Eq.(4.3)]. In the vicinity of each Landau level of the flake, we observe bulk Landau states [see Fig.4.8(a), (b)] and quantum Hall-like edge states [see Fig.4.8(c)]. The bulk states forming the Landau level are broad and separated from the edge. The edge states, on the other hand, are localized at the circumference of the dot. For increasing magnetic field, these states move spatially from the edge to the bulk eventually merging into the bundle of states associate with Landau levels. The same magnetic field evolution of wavefunctions was observed for graphene flakes without any moiré potential [93]. The superlattice potential of the hBN, however, causes the periodic modulations of the eigenstates.

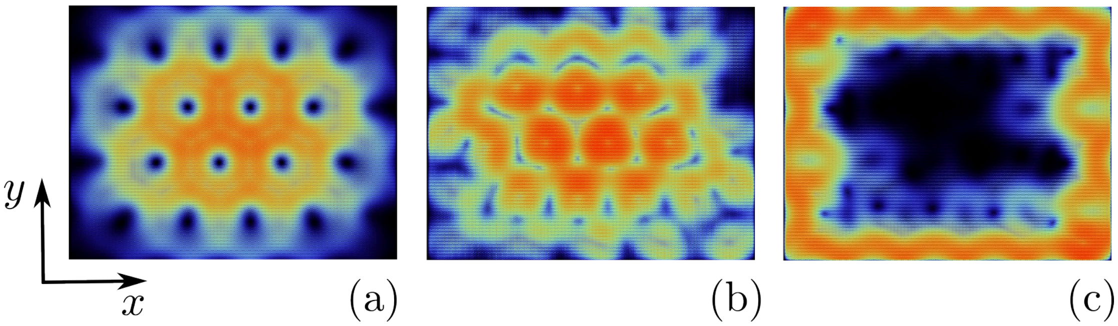

FIGURE 4.8: Typical eigenstates of graphene flake with hBN potential. (a) bulk eigenstate forming the 0^+ Landau level (at $B = 25$ T and $E = 0.08$ eV) (b) bulk eigenstate forming the -1 Landau level (at $B = 25$ T and $E = 0.15$ eV) (c) edge state in a vicinity of the 0^+ Landau level (at $B = 25$ T and $E = 0.08$ eV)

4.3.1 DOS of graphene on hBN: influence of disorder

Another interesting question is the influence of disorder on the density of states. Although graphene on hBN features reduced bulk and substrate induced disorder as compared to graphene on SiO_2, bulk disorder cannot be excluded completely and its possible impact on the signal in the experiment is important to elucidate. We therefore calculate the DOS of a graphene flake with a realistic hBN potential in the presence of single vacancies with a density of $n = 1.2 \cdot 10^{-4}$ Å^{-2} [see Fig.4.9(a,b)]. The main features such as the Landau levels and satellites remain discernible in line with previous studies [93]. However, the short-range disorder softens all features of the DOS. In particular, the fine structure of the Hofstadter butterfly is smeared out and is no longer well pronounced in agreement with the experiment [compare Fig.4.9(b) and Fig.4.5(b)]. We also notice one more difference to the disorder-free case – the presence of a magnetic field independent "gap" between the 0^+ and 0^- Landau levels at $N = 0$ [Fig.4.9(b)]. This gap is also present in the experiment [Fig.4.5(b)] and is missing in clean graphene flakes [Fig.4.5(a)]. In the disorder-free case there are no states between the two valley-splitted Landau levels [Fig.4.3(a)] and, therefore, the amount of charge in this area is $N = 0$. This means that the back gate voltage, which is $\sim N$, cannot resolve this region at all, i.e. no gap between 0^- and 0^+ valley splitted Landau levels is observed. On the other hand, there is a small amount of (edge-) states ($N \neq 0$) between, for example, -1 and 0^- or 0^+ and 1 Landau levels, which can couple to the back gate. Consequently, we observe a clear separation (a "gap") between these Landau levels in the DOS in the B-N plane in the disorder-free case. Introducing disorder not only broadens the Landau levels but also shifts a small amount of states from the 0^+ and 0^- Landau levels into the region in between [Fig.4.9(a)]. The non-zero contribution of these states opens a "gap" at $N = 0$ between the valley splitted zeroth Landau levels in the B-N plane [Fig.4.9(b)], which is also clearly visible in the experiment [Fig.4.5(b)]. Finally, long-range disorder,

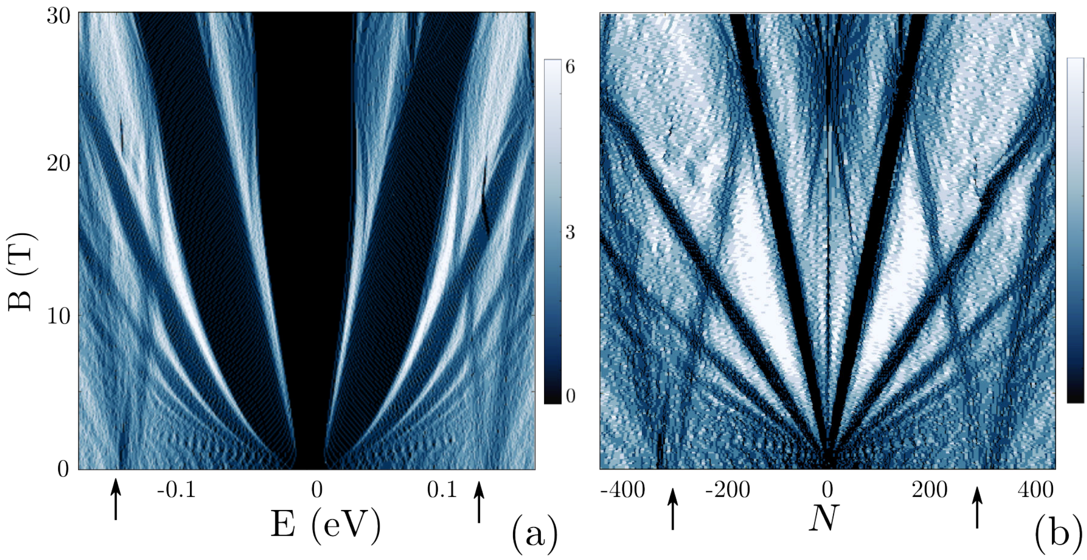

FIGURE 4.9: Density of states of graphene flake on top of hBN in the presence of single vacancies with a density of $n = 1.210^{-4}$ Å^{-2}: (a) in the B-E plane, as a function of magnetic field and electron energy; (b) in the B-N plane, as a function of magnetic field and number of charge carriers.

which would compete with the moiré superstructure is expected to further smear out the signal and the satellites.

4.4 Magneto-optical response of graphene flakes

As we discussed in the previous section, recent experiments aiming to probe the Hofstadter butterfly and the satellite structures of graphene on hBN in a magnetic field were performed using the back gate voltage (V_{bg}) to control the effective Fermi level in the graphene sheet. However, this method does not allow for probing the behavior of Landau levels and its Hofstadter butterfly in energy directly: quantum capacitance effects and deviations from the idealized linear density of states of graphene (as present, e.g., by the satellite structures) might substantially modify the relation between energy and applied back gate voltage.

A simple way to experimentally probe the physics of graphene in terms of energy is magneto-spectroscopy [15, 28, 94]. The method allows for probing the optical transitions between Landau levels in terms of energy directly. Localized (edge) states or traps which potentially alter the linear DOS of graphene and, thus, the V_{bg} coupling are eliminated. Fermi velocities are extracted from the fit of Dirac Landau levels to the appropriate transitions. In the presence of a supercell, e.g., due to a substrate induced moiré potential, the magneto-optical signal can also provide information about the satellites and the evolution of associated Landau levels. Moreover, such experiments can elucidate the interaction of graphene with the substrate. For example, magneto-optical experiments of graphene on hBN, [15] performed in magnetic fields up to ten Tesla, showed the presence of a 38 meV band gap due to breaking of sublattice (A and B) symmetry by the hBN substrate. In this section, we compare the behavior of a pristine graphene flake with a graphene flake aligned with hBN represented by a superlattice potential described in section 4.1.

We first calculate the DOS of a pristine graphene flake with Berry-Mondragon edge potential in a perpendicular magnetic field B [Fig.4.10(a)] in the same way we did in the previous section 4.3. The dimension of the flake we use here is 140×120 nm^2. As before we employ the third-nearest-neighbor tight-binding approximation to find the eigenstates of such a flake. For small magnetic fields ,i.e. $B \approx 0$, the density of states [see Fig.4.10(a)] is dominated by size quantization and properties of the flake boundaries. As the field increases, Landau levels begin to emerge resembling the behavior of bulk graphene. The transition from the linear DOS of bulk graphene at $B = 0$ to the Landau level regime is governed by the magnetic length l_B: the Landau levels appear when l_B becomes smaller than the flake diameter D.

The selection rule for optically allowed inter-Landau levels transitions is $\Delta N = |N_f| - |N_i| = \pm 1$, where $N_f(N_i)$ is the final (initial) Landau level quantum number [78]. The imperfections of the realistic graphene bandstructure beyond the Dirac approximation such as trigonal warping or the perturbation by the interaction with the substrate will break this selection rule and transitions with $|\Delta N| > 1$ become possible [78]. However, the probability of these transitions remains small. The main transition lines visible in the measured infrared absorption spectra [15, 28] are $\mathrm{T}_1 = E_1^D - E_0^D$, $\mathrm{T}_2 = E_2^D - E_{-1}^D$ and $\mathrm{T}_3 = E_3^D - E_{-2}^D$, where E_N^D is the energy of the N^{th} Landau level [Eq.(2.41)] The analytical forms of the transition lines minima in the absorption spectra can be deduced from Eq.(2.41) as

$$\begin{aligned} T_1 &= \sqrt{2|e|\hbar v_F^2 B}, \\ T_2 &= \sqrt{2|e|\hbar v_F^2 B}(\sqrt{2}+1), \\ T_3 &= \sqrt{2|e|\hbar v_F^2 B}(\sqrt{3}+\sqrt{2}). \end{aligned} \tag{4.8}$$

From the density of states calculations, which provide the eigenstates and eigenvalues of the graphene flake in a perpendicular magnetic field, it is straightforward to calculate optical dipole transitions between the different eigenstates. The associated optical

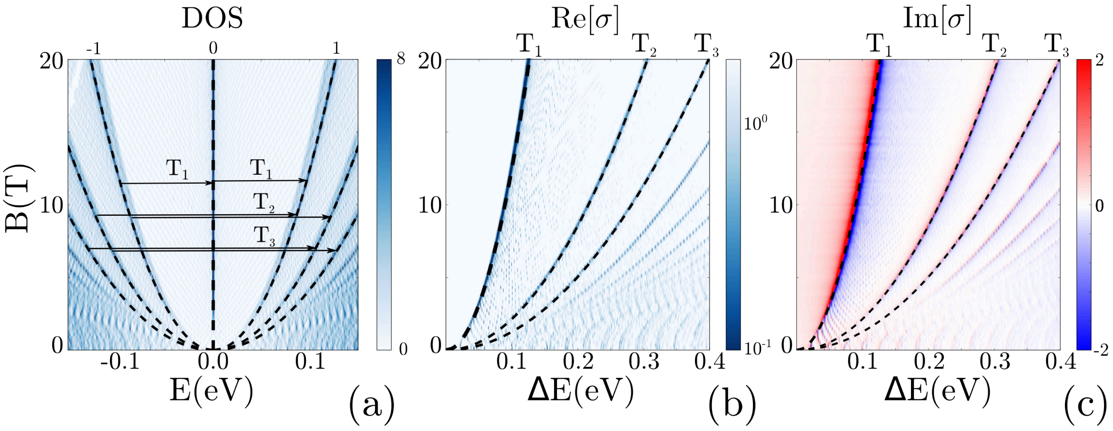

FIGURE 4.10: (a) The density of states of a 140x120 nm^2 pristine graphene flake as a function of energy and magnetic field. The black dashed parabolas correspond to the Landau levels of massless Dirac fermions [Eq.(2.41)]. (b) Real and (c) imaginary part of optical conductivity σ of the flake as a function of the excitation energy $\Delta E = \hbar\omega$ and magnetic field. The black dashed parabolas follows the analytical prediction for optical inter-Landau levels transitions [see Eq.(4.8)].

conductivity in velocity gauge is given by [78]

$$\sigma(\omega) = \frac{e^2\hbar}{iS}\sum_{a,b}\frac{f(\epsilon_a)-f(\epsilon_b)}{\epsilon_a-\epsilon_b}\frac{|\langle a|\hat{v}_x|b\rangle|^2}{\epsilon_a-\epsilon_b-\hbar\omega+i\eta}, \tag{4.9}$$

where ϵ_a (ϵ_b) is the eigenenergy corresponding to the eigenstate $|a\rangle$ ($|b\rangle$) of a flake, S is the size of the flake. The summation indices a and b go over all the eigenstates of the flake in the selected energy window. Here, we consider a graphene flake interacting with a laser light linearly polarized in x-direction. We transform Eq.(4.9) to the length gauge by replacing the velocity operator $\hat{v}_x = (i/\hbar)[\hat{x}, \hat{H}]$:

$$\sigma(\omega) = \frac{ie^2}{\hbar S}\sum_{a,b}\frac{f(\epsilon_a)-f(\epsilon_b)}{\epsilon_a-\epsilon_b-\hbar\omega+i\eta}(\epsilon_a-\epsilon_b)|\langle a|\hat{x}|b\rangle|^2. \tag{4.10}$$

The matrix element $\langle a|\hat{x}|b\rangle$ gives the transition dipole moment between the two eigenstates. We use the Fermi distribution $f(\epsilon_{a,b})$ at zero temperature with the chemical potential located at the Dirac point. The difference of Fermi distributions, $f(\epsilon_a)-f(\epsilon_b)$, is non-zero for transitions between occupied and unoccupied states corresponding to particle-hole excitation. Zeros in the denominator signify resonant absorption of photons with $\hbar\omega = \epsilon_a - \epsilon_b$. A line broadening $\eta = 0.1$ meV of sharp transitions between the discrete eigenstates of the flake is introduced to smoothen the numerical signal. This artificial broadening is small compared to the physical width of the coarse-grained DOS and, thus, of no consequence for the numerical results.

The magneto-optical conductivity calculated using Eq.(4.10) for the pristine graphene flake [Fig.4.10(b, c)] as function of the photon excitation energy $\Delta E = \hbar\omega$ shows the underlying optical transition lines between different Landau levels [Eq.(4.8)] following the main selection rule. The maximum of the real part of the optical conductivity as well as nodal lines of its imaginary part agree well with the analytical prediction [Eq.(4.8)] using the Fermi velocity $v_F^0 = 0.78 \cdot 10^6$ m/s of pristine graphene [see black lines in Fig.4.10(b, c)] corresponding to the present set of tight-binding parameters [see section 2.3]. We find sharp optical transition lines between different Landau levels with widths given by the widths of Landau levels in the DOS, which is ≈ 2 meV [Fig.4.10(a)]. Transitions with $\Delta N = \pm 2, 3, 4$ are too weak to be visible in the conductance signal but have non-vanishing dipole matrix elements.

We now discuss a graphene flake on hBN subject to a periodic moiré potential, which we discussed in detail in section 4.1. More precisely, we include the potentials $W(\vec{r})$ [Eq.(4.2)], $V(\vec{r})$ [Eq.(4.3)] and $W_{\mathrm{MB}}(\vec{r}, B)$ [Eq.(4.4)]. The sublattice symmetry breaking potential $W(\vec{r})$ [Eq.(4.2)] induced by the substrate opens up a band gap and modifies the Landau level spectrum according to Eq.(2.44). Hence, the positions of optical inter-Landau levels transitions for fermions with a gapped Dirac cone dispersion become

$$\begin{aligned} T_1 &= \sqrt{2|e|\hbar v_F^2 B + (E_g/2)^2} + E_g/2, \\ T_2 &= \sqrt{2|e|\hbar v_F^2 B \cdot 2 + (E_g/2)^2} + \sqrt{2|e|\hbar v_F^2 B + (E_g/2)^2}, \\ T_3 &= \sqrt{2|e|\hbar v_F^2 B \cdot 3 + (E_g/2)^2} + \sqrt{2|e|\hbar v_F^2 B \cdot 2 + (E_g/2)^2} \end{aligned} \tag{4.11}$$

It follows from Eq.(2.44), that the valley degeneracy of the zeroth Landau level is lifted by the presence of the gap. The effective many-body potential $W_{\mathrm{MB}}(\vec{r}, B)$ [Eq.(4.4)] introduces an additional linear magnetic field dependent splitting of valleys $\Delta_V \sim B$ (in this section we do not include the spin splitting due to the Zeeman effect).

For magnetic fields up to 10 T, the DOS of the graphene flake on hBN [Fig.4.11(a)] features the square root scaling for all $N \neq 0$ Landau levels $E_N^D \sim \sqrt{B}$ [Eq.(2.44)] [see black dashed parabolas in Fig.4.11(a)]. By contrast, the zeroth Landau level scales linearly with B due to the effective many-body potential $W_{\mathrm{MB}}(B)$ [see red dashed lines in Fig.4.11(a)]. If $W_{\mathrm{MB}} = 0$, the valley splitting in the zeroth Landau level is magnetic field independent [vertical black dashed lines in Fig.4.11(a)]. The positions of the absorption lines in the calculated optical conductivity for $N \neq 0$ coincide with the analytical estimate [Eq.(4.11)] for the energy difference between the Landau levels [see black dashed lines for T_2 and T_3 transitions in Fig.4.11(b,c)]. Here we used the reduced values for the Fermi velocity $v_F^{\mathrm{BN}} = 0.76 \cdot 10^6$ m/s deduced in section 4.3 for the potential modeling graphene on hBN. For the transition T_1 involving the $N = 0$ Landau level we have to include in Eq.(4.11) the linear magnetic field dependence of the 0^- Landau level due to many-body effects [red dashed curves in Fig.4.11(b,c)] resulting in a shift of the T_1

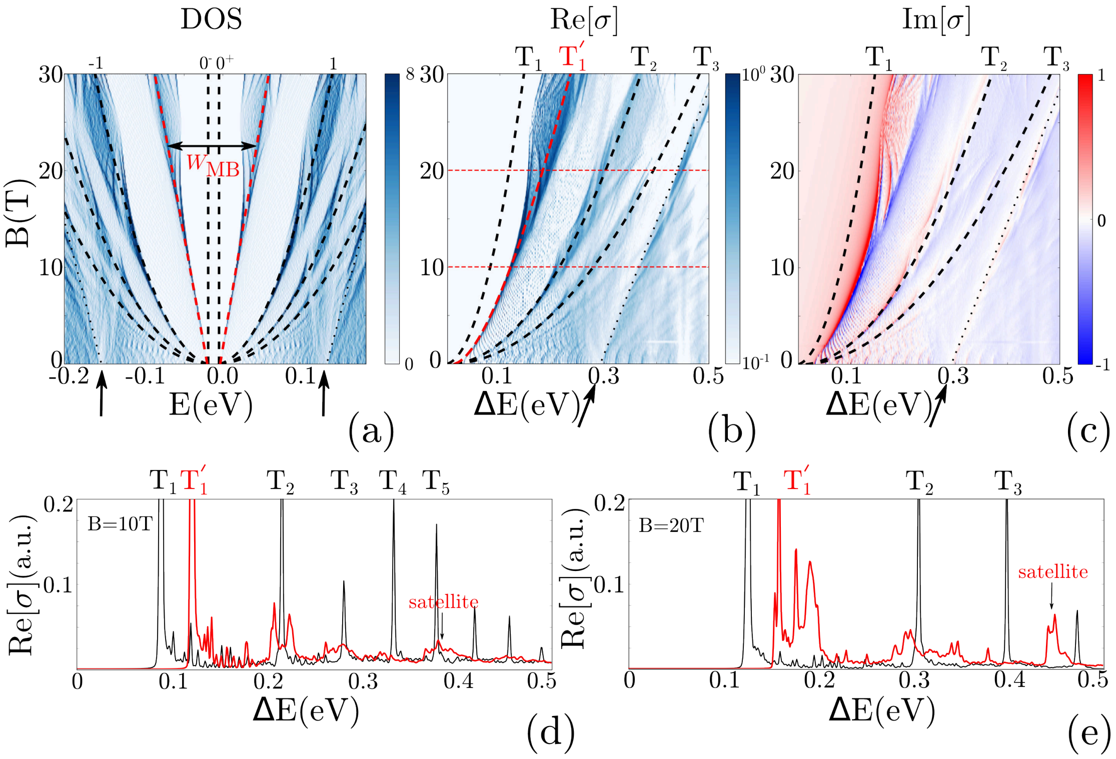

FIGURE 4.11: Same as Fig.4.10 but for a graphene flake placed on top of hBN resulting in a superlattice potential with 14 nm period. The black dashed parabolas in (a) correspond to the Landau levels of Dirac fermions with a finite mass [Eq.(2.44)]. The red dashed curves in (a) indicate the magnetic field dependent valley splitting in the zeroth Landau level due to phenomenological Many body term W_{MB} [Eq.(4.4)]. The satellites are marked by arrows and dotted lines. In (b) and (c) black dashed curves follow the analytical prediction for the position of inter-Landau levels transitions for massive Dirac fermions [Eq.4.11]. The red dashed curve shows the position of T_1 optical transition if magnetic field dependent many-body potential W_{MB} is included. The optical transition between the Landau levels of satellites are marked by arrows and dotted lines. Details of the real part of the optical conductivity as a function of energy at (d) B=10T and (e) B=20T. The red traces show the conductivity of graphene flake on top of hBN as in (b). For comparison, the black traces show the conductivity of pristine graphene flake presented in Fig.4.10(b).

transition to T_1'. The sensitivity of the T_1 transition to the many-body valley splitting in the zeroth Landau level, thus, offers an alternative to activation gaps measurement [87].

At higher magnetic fields, the Hofstadter butterfly becomes visible as a diamond-like structure in the DOS [Fig.4.11(a), see also the detailed structure in Fig.4.3(d)]. The optical conductivity reveals the Hofstadter butterfly as a magnetic field dependent absorption line broadening [Fig.4.11(b,c)]. The sharp peaks in the optical response of pristine graphene are replaced by a broad multi-peak structure [compare black T_1 transition of pristine graphene with red T_1' transition for graphene on hBN in Fig.4.11(d,e)]. The energetic width of the diamond (FWHM) of the T_1' transition at 25 T, i.e. at the magnetic field where the ratio of the magnetic flux through the moiré supercell equals to the magnetic flux quantum $\Phi = \Phi_0$ [section 4.2], is 20 meV consistent with the size of the first Landau level diamond obtained from the density of states [Fig.4.11(a)].

As we discussed in section 4.3, the Landau levels of the satellites evolve linearly with magnetic field in the DOS near E=-0.15 eV and E=0.14 eV at B=0 T [see arrows and dotted black lines in Fig.4.11(a)]. The same behavior is observed in the optical conductivity where a linear transition line emerges starting from ΔE=0.3 eV at B=0 T [marked by arrows and dotted black lines in Fig.4.11(b,c)], leading to a well-defined peak structure at ∼20T [Fig.4.11(d)]. The slope of the line corresponds to the slope of the Landau levels associated with the satellites. The difference in the magnetic field evolution of Landau levels of the satellites and the main Dirac cone is not obvious when measured as a function of V_{bg} [see section 4.3]. By contrast, energy-dependent optical measurements can distinguish Dirac and Schrödinger dispersions in the bandstructure. Magneto-optical experiments for graphene on hBN [15] have, up to now, not focused on the satellite structures induced by the moiré pattern. While challenging, the experimental observations of the satellites and their magnetic field evolution would yield valuable information on the moiré-potential modified bandstructure.

4.4.1 Magneto-excitons in graphene flakes

In the single-particle picture we considered so far, the calculated optical conductivity demonstrates the resonant optical inter-Landau levels transitions at the photon energies following the analytical prediction [Eq.(4.8)]. However, magneto-optical experiments [15, 28] probing Landau levels of graphene on different substrates reveal a shift of these inter-Landau levels transition lines. The shift can be conveniently parametrized in terms of a transition-line dependent Fermi velocity v^{T_i} in the analytical prediction Eq.(4.8). Notably, different velocity renormalizations for different transition lines were also observed in magneto-Raman scattering experiments [84, 85]. The velocity renormalization is often related to the influence of magneto-excitons [48, 95] created by optical excitations between the Landau levels. This many-body effect is absent in addition spectroscopy when varying the back-gate voltage V_{bg}

In this section we discuss the influence of many-body effects on magneto-optical transitions due to the formation of inter-Landau level excitonic states. To lowest order the excitonic wave function is a product of an electron and a hole wave function:

$$\Psi^{\mathrm{exc}}_{NM}(\vec{r}_{\mathrm{el}}, \vec{r}_{\mathrm{h}}) = \psi_N(\vec{r}_{\mathrm{el}})\psi_M(\vec{r}_{\mathrm{h}}), \tag{4.12}$$

where $\vec{r}_{\mathrm{el}}$ ($\vec{r}_{\mathrm{h}}$) is an electron (hole) coordinate, ψ_N and ψ_M correspond to the wave functions of the N^{th} and M^{th} Landau level undergoing optical transitions. The corresponding Dirac equation reads

$$\hat{H}\Psi^{\mathrm{exc}}_{NM}(\vec{r}_{\mathrm{el}},\vec{r}_{\mathrm{h}}) = E\Psi^{\mathrm{exc}}_{NM}(\vec{r}_{\mathrm{el}},\vec{r}_{\mathrm{h}}), \tag{4.13}$$

where

$$\hat{H} = \sum_{i=el,h} v_F \vec{\sigma}\cdot(\vec{p}_i - e\vec{A}) - \frac{e^2}{4\pi\varepsilon_0\varepsilon\,|\vec{r}_{\mathrm{el}} - \vec{r}_{\mathrm{h}}|}, \tag{4.14}$$

ε is a dielectric constant and ε_0 is the permittivity of the vacuum. We use $\varepsilon = 5$ found for graphene on SiO_2 within the random phase approximation (RPA) [96] and also for graphene on hBN [84]. If we neglect the Coulomb interaction [second term in $\hat{H}$ in Eq.(4.14)] the excitonic energy coincides with Eq.(4.8), i.e. the single-particle energy difference. The Coulomb interaction changes the transition energy value resulting in the observed energy shift due to particle-hole attraction. The magneto-excitonic effect was studied in details for the two-dimensional electron gas [97, 98] and for graphene [48, 95, 99]. In particular, it was shown that the excitation energy can be viewed as a sum of several terms: the (non-interacting) single-particle exciton energy $\Delta E = E^D_N - E^D_M$; the exciton binding energy, i.e. the direct Coulomb two-particle interactions between the particle and the hole; the annihilation and creation of electron-hole pairs at different points of the Brillouin zone; and the exchange interaction. The direct Coulomb term is negative and gives the leading contribution to the exciton binding energy. Therefore, the optical transition energy becomes smaller than estimated in the single-particle picture. However, the last two contributions, while smaller, are positive and slightly reduce the binding energy. Since the effect of these contributions is already, to a certain extent, empirically accounted for by the dielectric response of the medium ε, we neglect an explicit treatment of these terms.

Within the tight-biding approximation applied to graphene dots, it is possible to account for magneto-excitonic effects. To compare our results with the experiment we include the dielectric environment for graphene on a SiO_2 substrate by taking into account the dielectric constant ε when evaluating the Coulomb interaction term. We evaluate the dominant contribution of the direct Coulomb electron-hole interaction using first-order perturbation theory. Consider an optical transition between the two Landau levels N and M. Each of the Landau levels is degenerate and is formed by several eigenstates of the flake [see Fig.(4.10(a))] [93]. We restrict our considerations only to eigenstates contributing to a specific transition. A photoexcited state can be written as a superposition

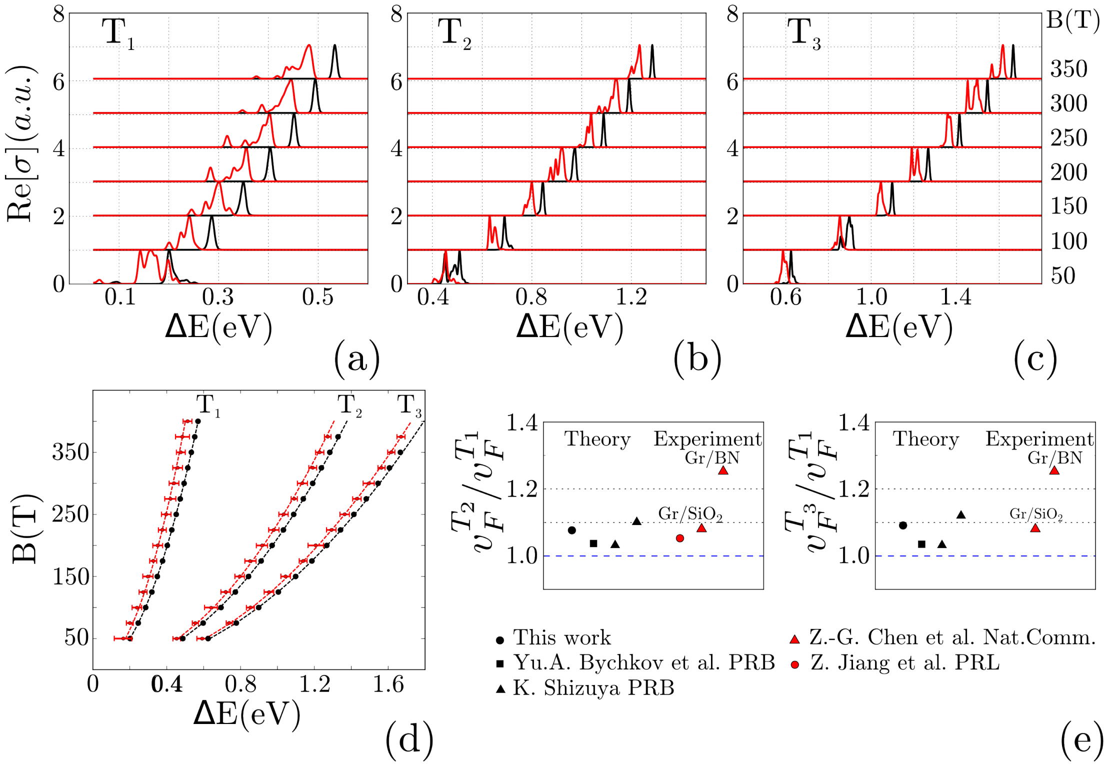

FIGURE 4.12: (a, b, c) Real part of the optical conductivity of the main transition lines T_1, T_2 and T_3 plotted with a constant shift to resolve magnetic field. Black traces correspond to the single-particle transitions, red traces correspond to the optical transitions taking into account the direct Coulomb electron-hole interactions from the first-order perturbation theory. (d) The position (dots) and width (bars) of spectral lines extracted from the first and second moment of the single-particle (black) and excitonic excitation (red) spectra. The black curves correspond to the theoretical Landau level transitions [Eq.(4.8)] with Fermi velocity $v_F^0 = 0.78 \cdot 10^6$ m/s. The red curves correspond to the fit of the theoretical lines Eq.(4.8) with renormalized Fermi velocities: $v_F^{\mathrm{T}_1} = 0.69 \cdot 10^6$ m/s, $v_F^{\mathrm{T}_2} = 0.745 \cdot 10^6$ m/s and $v_F^{\mathrm{T}_3} = 0.755 \cdot 10^6$ m/s. (e) The ratio between Fermi velocities of T_2 (right) and T_3 (left) transitions to the Fermi velocity of T_1: theory versus experiment.

of flake eigenstates near the corresponding Landau levels involved in the transition:

$$\Psi_{NM}^{\mathrm{exc}}(\vec{r}_{\mathrm{el}}, \vec{r}_{\mathrm{h}}) = \sum_{a,b} C_{ab} \phi_a^N(\vec{r}_{\mathrm{el}}) \phi_b^M(\vec{r}_{\mathrm{h}}). \tag{4.15}$$

The expansion coefficients C_{ab} can be obtained by inserting this wave function ansatz into the Dirac equation [Eq.(4.14)] as

$$(\epsilon_a^N - \epsilon_b^M) C_{ab} - \sum_{a',b'} V_{a'b'}^{ab} C_{a'b'} = \epsilon C_{ab}, \tag{4.16}$$

with eigenenergies of the flake ϵ_a^N (ϵ_b^M) in the vicinity of N^{th} (M^{th}) Landau level. The Coulomb matrix element is

$$V_{a'b'}^{ab} = \frac{e^2}{4\pi\epsilon_0\epsilon} \iint d\vec{r}_{\text{el}} d\vec{r}_{\text{h}} \frac{\phi_{a'}^{*N}(\vec{r}_{\text{el}})\phi_{b'}^{*M}(\vec{r}_{\text{h}})\phi_a^N(\vec{r}_{\text{el}})\phi_b^M(\vec{r}_{\text{h}})}{|\vec{r}_{\text{el}} - \vec{r}_{\text{h}}|} \tag{4.17}$$

Eq.(4.16) is similar to the Bethe–Salpeter equation (BSE) [100] adapted for a finite size graphene flake. The Coulomb integral [Eq.(4.17)], as discussed above, gives the exciton binding energy. The full solution of Eq.(4.16) is numerically difficult as the size of the Coulomb matrix $V_{a'b'}^{ab}$ is determined by the product of the number of eigenstates forming the Landau levels N and M. For each Landau level involved in the transition, we consider the energetically closest $N_S \approx 30-40$ eigenstates of a flake, which is a good compromise between accuracy and numerical effort. The dimension of the matrix $V_{a'b'}^{ab}$ is $N_S^2 \times N_S^2 \approx 10^6$. Moreover, each matrix element requires evaluation of a double spatial integral with a Coulomb kernel. Therefore, to keep the problem numerically feasible we solve Eq.(4.16) within first-order perturbation theory [45], i.e. we evaluate only the diagonal Coulomb matrix elements V_{ab}^{ab} in the sum, and reduce the size of the graphene flake to 24×24 nm^2, to speed up the calculation of each matrix element. Since the size of the flake is smaller than we used in section 4.3 and section 4.4, the Landau levels are formed at higher magnetic fields, when the magnetic length l_B becomes smaller than the flake diameter D [according to the geometrical argument given in section 2.5]. For example, the $N = 3$ Landau level participating in the T_3 optical transition emerges only at $B \gtrsim 30$ T for the reduced flake size we consider here. For magnetic fields strong enough to form the magnetically confined Landau level states inside the flake, the magneto-excitons created by two Landau levels are only weakly perturbed by the flake boundaries and boundary effects on our results can be neglected, making our results applicable also to bulk graphene. In first-order perturbation theory each electron-hole pair $|a,b\rangle$ is treated independently and the corresponding first-order energy correction to the noninteracting electron-hole transition energies $\epsilon_{a,b}^{(0)} = (\epsilon_a - \epsilon_b)$ is given directly by the diagonal matrix element:

$$\epsilon_{a,b}^{(1)} = V_{ab}^{ab} = \frac{e^2}{4\pi\epsilon_0\epsilon} \iint d\vec{r}_{\text{el}} d\vec{r}_{\text{h}} \frac{|\phi_a^N(\vec{r}_{\text{el}})|^2|\phi_b^M(\vec{r}_{\text{h}})|^2}{|\vec{r}_{\text{el}} - \vec{r}_{\text{h}}|}. \tag{4.18}$$

The total energy of the $|a,b\rangle$ exciton in this approximation is $\epsilon_{a,b} = \epsilon_{a,b}^{(0)} - \epsilon_{a,b}^{(1)}$.

We focus on the first three transition lines and calculate the energy shift $\epsilon_{a,b}^{(1)}$ for each electron-hole excitation pair $|a,b\rangle$ for different magnetic fields. More precisely, we first calculate the eigenstates and eigenfunctions of the flake using the third-nearest-neighbor tight-binding approach for a specific B-field. We then select eigenstates corresponding to each Landau level contributing to the photoexcitation and evaluate Eq.(4.18). The optical conductivity of each electron-hole pair, which is related to the dipole matrix element between an electron in eigenstate of the flake $|a\rangle$ and a hole in $|b\rangle$, is calculated using Eq.(4.10), however, with new excitonic energies. Within first-order perturbation theory, our calculations yield a clear shift of the T_1, T_2 and T_3 transition lines in the direction of smaller photon energies [see red traces in Fig.4.12(a,b,c)] as compared to the noninteracting single-particle picture [see black traces in Fig.4.12(a,b,c)]. The position and width of the transitions can be deduced from the first and second moments of the calculated spectral lines. If we neglect the Coulomb interaction, we extract the position of transitions [see black dots in Fig.4.12(d)] in agreement with analytical expectation [Eq.(4.8)] with a Fermi velocity of pristine graphene $v_F^0 = 0.78 \cdot 10^6$ m/s [see black traces in Fig.4.12(d)]. By contrast, the positions of transition lines including the two-particle excitonic corrections are shifted to lower excitation energies ΔE [see red points in Fig.4.12(d)]. Interestingly, the shifted transition lines demonstrate the same square root dependence on the magnetic field, i.e. $\Delta E \sim \sqrt{B}$, as the single-particle energies. The $\sqrt{B}$ scaling of the excitonic correction is related to the inverse scaling of the computed Coulomb integral [Eq.(4.18)] with the length scale of the magneto-exciton determined by the magnetic length $l_B \sim (\sqrt{B})^{-1}$. Therefore, both the single-particle transition energies as well as the first order excitonic correction to these energies scale as square root of the magnetic field. Consequently, the results we obtain can be (to first order) directly compared to magneto-optical experiments on bulk graphene at laboratory accessible magnetic fields. The energy shifts we compute are different for different transitions. Since the lines should follow a $\sqrt{B}$ scaling, we can conveniently introduce the line-specific Fermi velocities in the Eq.(4.8). In particular, from the best fit we find for T_1 the Fermi velocity $v_F^{\mathrm{T}_1} = 0.69 \cdot 10^6$ m/s; for T_2, $v_F^{\mathrm{T}_2} = 0.745 \cdot 10^6$ m/s and for T_3, $v_F^{\mathrm{T}_3} = 0.755 \cdot 10^6$ m/s. This velocity renormalization is clearly observed in recent experiments [15, 28]. To provide a comparison between experimentally observed and calculated line shifts, we evaluate the ratio of the renormalized Fermi velocities of the $\mathrm{T}_{2,3}$ transitions to that of T_1 [see Fig.4.12(e)]. By doing so, we can distinguish effects of Landau level specific velocity renormalization from other bandstructure effects that uniformly affect all transitions. We find a reasonable agreement with experiments measuring optical inter-Landau levels transitions for graphene on SiO_2 and also with alternative theoretical approaches for bulk graphene [95, 99][Fig.4.12(e)]. The effect of puddles observed in graphene on SiO_2 can be included within our tight-binding description by including a smooth disorder potential with an amplitude of 25 meV (50 meV) and a correlation length of 10 nm (5nm), which is close to realistic values [55]. The calculated transitions lines remain well-defined in the presence of disorder and feature the same velocity renormalization as for pristine graphene.

However, the measured magneto-optical response for graphene on hBN reveals a velocity renormalization notably different from our theoretical estimate [Fig.4.12(e)]. This mismatch arises due to substantially lower value of $v_F^{\mathrm{T}_1}$ in experiment compared to our theory, which can be attributed to many-body effects strongly influencing the zeroth Landau level. One possible explanation is the substantial splitting of the four-fold degenerate Landau levels for graphene on hBN observed in quantum capacitance measurements [18]. On the other hand, any such splitting should shift the T_1 line to higher photon energies [as seen in Fig.4.11(b,c)], i.e. in the opposite direction to that observed in the experiment. Clearly, future magneto-optical experiments for graphene on hBN are necessary to resolve this puzzle.

4.5 Commensurate to incommensurate transition

In the discussion up to now, we considered graphene on top of the hBN with a fixed carbon-carbon distance throughout the flake. In reality graphene aligned on hBN features a periodic strain pattern [101], which depends on the alignment angle ϕ. In particular, for a moiré periodicity of less than 10 nm, the Young's modulus follows a sinusoidal pattern. For larger moiré supercells and $\phi \to 0$ the behavior is different: ~ 2 nm wide narrow regions with large Young's modulus alternate with broad regions of small modulus. This change in behavior is explained by a commensurate $-$ incommensurate transition. It appears that for almost perfect alignment $\phi \approx 0$ the energetically most favorable configuration corresponds to locally adjusting the graphene lattice to be commensurate with hBN. In this case the loss in elastic energy is compensated by the gain in van der Waals interaction energy with the substrate. For smaller moiré supercells, the incommensurate configuration is energetically more preferable [101, 102].

To account for the induced strain in graphene on hBN in the perfectly aligned configuration considered in the previous sections, we change the on-site potential $V(\vec{r})$ and the first nearest - neighbor coupling $t_1^s(\vec{r})$ according to the measured Young's modulus profile. Since $V(\vec{r})$ describes only variations of the local on-site potential and does not necessary relate to lattice deformations, local variations in the hopping element $t_1^s(\vec{r})$ are important to include if one aims to account for a strained graphene lattice. As a template for $W(\vec{r})$, $V(\vec{r})$ and $t_1^s(\vec{r})$ we use a hexagonal structure [see Fig.4.13(a)] following experimental observations [101]. The template consists of 3 regions of different alignment of graphene with hBN: *I*, *III* and *V* in accordance with section 4.1. The energetically most favorable region V, where carbon atoms of sublattice A of graphene are on top of boron, appears commensurate with the hBN over a much more extended area than considered in section 4.1. As a result the graphene in this region is stretched

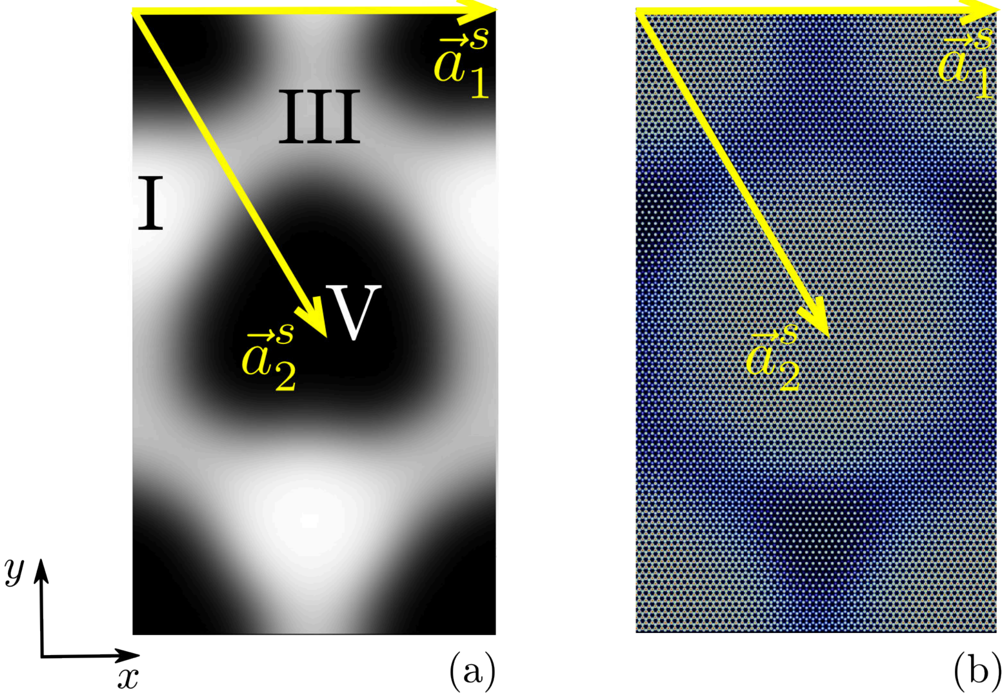

FIGURE 4.13: (a) Template of a potential in an extended supercell following the commensurate state of the experiment [101]. (b) The on-site potential used in the simulations based on the template in (a). The moiré supercell (with periodicity of 13.8 nm) lattice vectors are shown in yellow.

to match the lattice constant of hBN, which is 1.8% larger. To compensate the commensurate parts of the supercell, graphene in regions *I* and *III* becomes compressed by about 1.4 to 2%. These compressed areas create the hexagons of large Young's modulus seen in experiment [101]. We reuse the maximal values of the $W(\vec{r}) \propto \hat{\sigma_z}$ in those three regions according to our previous discussions and Ref. [79], as they correspond to the local van der Waals interactions of aligned graphene with boron, nitride or a vacancy. However, we change the on-site potential $V(\vec{r})$ as well as the first nearest-neighbor coupling t_1 to account for the strain. The tight-binding parameters for $V(\vec{r})$ and t_1^s under strain can be obtained from DFT calculations of stretched or compressed graphene [103]. The maximal values of the potentials and nearest-neighbor couplings are summarized in Table 4.1, where for the region V we also added an adhesion energy of -20 meV obtained in [79].

Bandstructure calculations with the strain-dependent potential [Fig.4.14(b) and including the local variation of the t_1 in Fig.4.14(c)] reveal features similar to the ones observed for a moiré superlattice potential in a form of Gaussians discussed in section 4.3 [Fig.4.14(a)]. In particular, we observe the formation of avoided crossings and opening of the band gap at the main cone D_0 [marked by green and red in Fig.4.14, respectively]. The new potential creates a larger band gap $E_g = 40$ meV at D_0 as compared to $E_g = 15$ meV for the superlattice potential used in section 4.3. The increase of the band gap is

Table 4.1: Summary of parameters of superlattice potential for the different aligned regions of graphene on hBN

	I	III	V
carbon - carbon distance (in % of $a = 1.42$ Å for unstratched graphene)	98 %	99 %	101.8 %
$W(\vec{r})$ (meV)	57	-34	-47
$V(\vec{r})$ (meV)	30	20	-43
t_1^{S}/t_1	1.06	1.04	0.95

related to the geometrical enlargement of the region V accounting for the commensurate state. We note that the same band gap $E_g = 38 \pm 4$ meV was extracted from fitting the transition lines between Landau levels in a magneto-optical experiment performed for graphene on hBN [15]. The positions of the avoided crossings and their parabolic behavior qualitatively do not change for different effective moiré potentials [compare the bandstructure used for simulations of DOS in section 4.3 Fig.4.14(a) with the bandstructures calculated for the new potential Fig.4.14(b,c)]. The interesting feature, however, is a more pronounced electron - hole asymmetry of the avoided crossings (at ~ 0.13 eV and ~ -0.16 eV) which generate the satellite structures in the DOS [marked in green in Fig.4.14(a,b,c) near 0.13 eV and -0.16 eV]. The satellite bands at 0.13 eV become dense as compared to the bands at ~ -0.16 eV. Therefore, the magnetic evolution of the satellite at positive energy is expected to be less pronounced than the evolution of the satellite at negative energy. This electron - hole asymmetry of the satellites is very well visible in the experiment [18, 19]. However, the linear magnetic field dependence of the satellites in the $B - E$ plane should not change and their overall behavior stays the same as discussed in section 4.3.

We also point out another interesting detail: the bandstructure stays qualitatively unchanged if we include strain by local variation of the bond length [Fig.4.14(c)], i.e. by local variation in the nearest-neighbor hopping amplitude t_1^s, as compared to the strain free case $t_1^s = t_1$ [Fig.4.14(b)]. Bandstructures with [Fig.4.14(c)] and without [Fig.4.14(b)] strain both are qualitatively similar to the bandstructure obtained for the parameters of an effective hBN potential used in the previous sections [Fig.4.14(a)]. We therefore expect no crucial change in the magnetic field evolution of the DOS in a system with and without strain. Indeed, the DOS calculated using the hBN potential discussed in this section reveals the same structure as the DOS calculated in section 4.3. Although, the inclusion of strain into our tight-binding model qualitatively does not affect the DOS, it can be critically important in, for example, the local density of states (LDOS) of graphene on hBN.

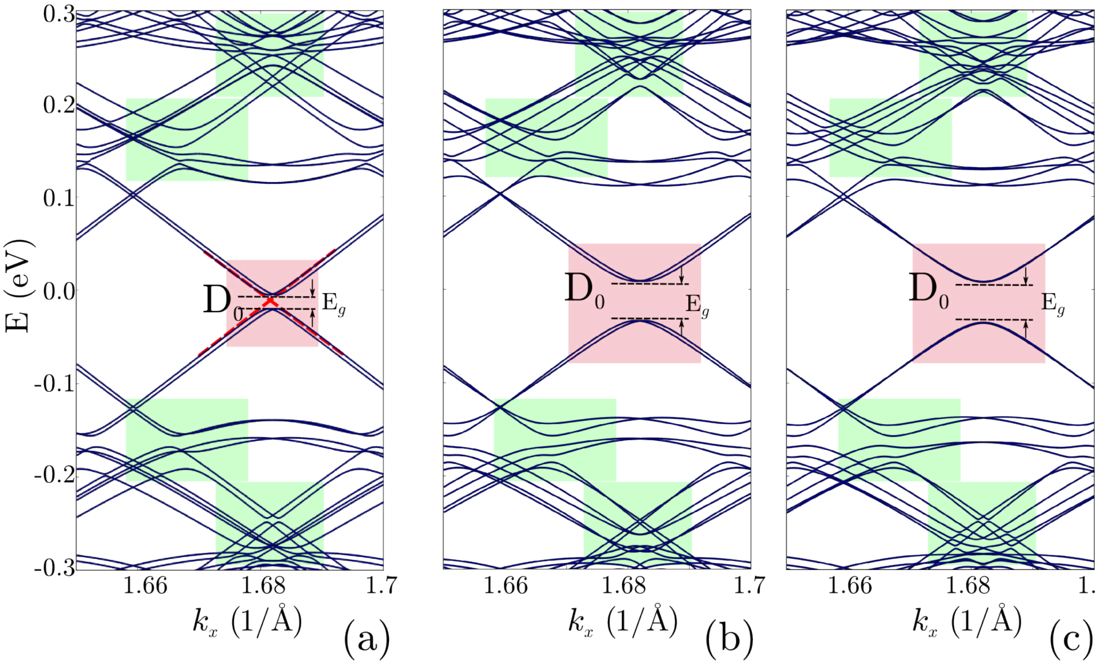

FIGURE 4.14: Cut through bandstructure ($k_y = 0$) for graphene on hBN: (a) with a moiré superlattice potential in a form of Gaussians discussed in section 4.1 and 4.3: $W_I = 57$ meV, $W_{III} = -34$ meV and $W_V = -47$ meV; $V_V = -100$ meV. (b, c) with a moiré superlattice potential in a form of a hexagonal pattern according to the commensurate state in the experiment [101]. The parameters $W(\vec{r})$ and $V(\vec{r})$ are given in Table 4.1: (b) with a constant nearest-neighbor interaction $t_1^s = t_1$ of unstrained graphene; (c) with a strain dependent nearest-neighbor interaction t_1^s given in Table 4.1.

Chapter 5

Nonlinear optical response of graphene to a few cycles THz laser pulse

Graphene with its exceptional electronic properties is a very interesting playground for the investigation of the optical response. The linear dispersion of graphene in contrast to the parabolic one in semiconductors plays an important role in the generation of nonlinear optical response of graphene to an applied terahertz laser field [the process is schematically shown in Fig.5.1]. The optical response of graphene in the THz part of the spectrum was extensively studied theoretically [104–106] by solving the Boltzmann equation or the Dirac equation in the time-domain. With the advances in THz laser technology achieved in the last years, studies of different nonlinear effects (such as second harmonic generation [107, 108], photon drag effect [109], four-wave mixing [108] as well as the study of the nonlinear carrier dynamics [110] and THz generation [111]) in graphene became feasible. The nonlinear low odd harmonic generation in graphene was examined experimentally by Paul et al. [112] and Bowlan et al. [21]. In Ref. [112] the response of multi-layer (∼ 20 layers) epitaxial graphene and a single layer graphene produced by chemical vapor deposition (CVD) to a strong teraherz field was investigated. This study showed no generation of harmonics in graphene up to 40 kV/cm amplitudes of the laser fields. Nevertheless in the experiment by Bowlan et al. [21], nonlinear odd harmonics of multi-layer (∼ 45 layers) epitaxial graphene were observed for short laser pulses with 40 kV/cm field strength and 2 THz frequency. The power spectrum of the detected far-field THz response showed the first, third, and fifth harmonics with relative strengths of 1, $3 \cdot 10^{-3}$ and $5 \cdot 10^{-4}$. In this chapter we develop the theory of the nonlinear response of graphene by solving the Dirac equation in the time domain and by solving the time-dependent Schrödinger equation with the tight-binding Hamiltonian of graphene. The

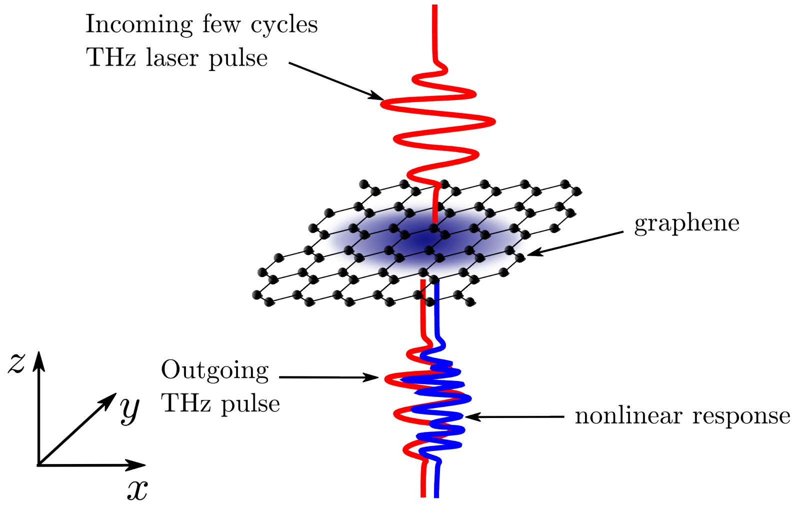

FIGURE 5.1: The incoming THz laser pulse (red) accelerate electrons in graphene, which emit radiation (blue) at higher frequencies.

latter approach, although applied to finite size structures, produces qualitatively and quantitatively similar nonlinear responses to the solution of the Dirac equation for bulk graphene. Furthermore, the tight-binding approach allows for inclusion of different types of disorder, superlattice potentials due to the substrate (for example, the hBN potential considered in chapter 4) and imperfections of the bandstructure such as trigonal warping and electron-hole asymmetry. We also provide a comparison of the calculated response with the experiment [21] and analyze the change in the signal due to non-zero doping and disorder.

Another issue we address is the high-harmonic generation in graphene and especially the high harmonic cut-off we observe. The calculated harmonic spectrum reveals similarities to the nonlinear response of atoms to intense laser fields [22–24], where the generation of high harmonics is due to the recombination of ionized electrons with their ions. We derive the harmonic energy cut-off in graphene, which is proportional to the amplitude of the electric field $\sim E_0$, whereas in atoms it is proportional to the field intensity $\sim E_0^2$. The study of high-harmonic generation in other solid materials, like ZiO [25], GaSe [26] and SiO_2 [113], also unveil linear scaling with E_0 of the cut-off. Probing the driven fermionic dynamics in close vicinity to the Dirac point is an interesting problem from the point of view of solid state physics and relativistic electron dynamics.

5.1 Classical motion of Dirac fermions in a laser field

Surprisingly, the enhanced non-linear properties of graphene follow from the linear dispersion of Dirac fermions. To illustrate this, let us consider the classical motion of a massless Dirac fermion in a continuous linearly polarized laser with the harmonic electric field:

$$E_x(t) = E_0 \cos(\omega t), \tag{5.1}$$

where E_0 is the amplitude and ω is the frequency of the laser. Then, the Hamiltonian of the classical relativistic fermion reads:

$$H = v_F \sqrt{p_x^2 + p_y^2} - eE_x x, \tag{5.2}$$

and the canonical Hamilton equations take the form

$$\begin{aligned}
\dot{p_x} &= \frac{\partial H}{\partial x} = -eE_x, \\
\dot{p_y} &= \frac{\partial H}{\partial y} = 0, \\
\dot{x} = v_x &= \frac{\partial H}{\partial p_x} = v_F \frac{p_x(t)}{\sqrt{p_x(t)^2 + p_y(t)^2}}, \\
\dot{y} = v_y &= \frac{\partial H}{\partial p_y} = v_F \frac{p_y(t)}{\sqrt{p_x(t)^2 + p_y(t)^2}}.
\end{aligned} \tag{5.3}$$

The electron momentum follows from the first two equations:

$$\begin{aligned}
p_x &= p_{x0} + \frac{eE_0}{\omega} \sin(\omega t) = p_{x0} + eA_x(t), \\
p_y &= p_{y0} = \text{const},
\end{aligned} \tag{5.4}$$

where $\vec{p}_0 = (p_{x0}, p_{y0})$ is the initial electron momentum. The x component of the momentum oscillates harmonically and follows the vector potential of the laser field

$$A_x(t) = -\int E_x(t) dt = \frac{E_0}{\omega} \sin(\omega t). \tag{5.5}$$

The time evolution of the electron energy is

$$E(t) = v_F \sqrt{(p_{x0} + eA_x(t))^2 + p_{y0}^2}. \tag{5.6}$$

Unlike the harmonic behavior of the momentum $p_x(t) \propto A_x(t)$, the electron velocity exhibits strong nonlinear or anharmonic behavior (from Eq.(5.3))

$$v_x = v_F \frac{p_{x0} + eA_x(t)}{\sqrt{(p_{x0} + eA_x(t))^2 + (p_{y0})^2}}, \tag{5.7}$$

which arises from the square-root dependence of the denominator. This is different from the behavior of nonrelativistic electrons (or electrons in semiconductors with parabolic energy dispersion), where the velocity is proportional to the momentum and likewise exhibits harmonic oscillations with the field. The physical observables such as the electric current ($j_x = -|e|nv_x$ with n being the electron density) or the second derivative of the dipole moment responsible for the far-field radiation are proportional to the electron velocity and, therefore, are also nonlinear. In general, the current can be connected to the laser field as

$$j_i(t) = \sigma^{(1)}_{ij} E_j(t) + \sigma^{(2)}_{ijk} E_i(t) E_j(t) + \sigma^{(3)}_{ijkl} E_j(t) E_k(t) E_l(t) + \cdots , \tag{5.8}$$

where indices i,j,k,l refer to the Cartesian coordinates. The first term describes the linear response of the medium characterized by linear optical conductivity tensor $\sigma^{(1)}$, whereas the other terms describe the nonlinear response to the applied electric field and are characterized by the nonlinear optical conductivity tensor $\sigma^{(N\neq 1)}$. We simplify Eq.(5.8) for the fields $\vec{E}(t) = E_x(t)\vec{e_x}$ considered in this chapter as

$$j_x(t) = \sigma^{(1)} E_x(t) + \sigma^{(2)} E_x^2(t) + \sigma^{(3)} E_x^3(t) + \cdots . \tag{5.9}$$

The higher order terms contribute to the response at higher carrier frequencies than the frequency ω of the driving field. For example, the second order nonlinearity $\sim E_x^2(t)$ contributes to the frequency of 2ω and the third order nonlinearity $\sim E_x^3(t)$ contributes to 3ω in the response.

The nonlinear behavior of fermions in graphene depends on their initial momentum. For instance, consider $p_{y0} = 0$. In this case the x velocity component is

$$v_x = \xi v_F \frac{p_{x0} + eA_x(t)}{|p_{x0} + eA_x(t)|} = \xi v_F \mathrm{sign}\left[\sin(\omega t)\right] \tag{5.10}$$

where $\xi = \pm 1$ is the conduction and valence band index. The obtained velocity is a square wave, and its Fourier expansion yields

$$v_x = \xi v_F \frac{4}{\pi} \left(\sin(\omega t) + \frac{1}{3}\sin(3\omega t) + \frac{1}{5}\sin(5\omega t) + \cdots \right) . \tag{5.11}$$

Since $j_x \sim v_x$, we observe a strong non-linear signal [Eq.(5.9)] with odd harmonics $(\omega, 3\omega, 5\omega, \cdots)$ and relative amplitudes $(1, 1/3, 1/5, \cdots)$. It is also striking that the theory predicts the generation of odd harmonics at arbitrary low field strengths in this example. However, to obtain the response from an ensemble of electrons in graphene near the Fermi energy we need to find the total current by integrating over the different initial electron momenta. As a result the nonlinearity in graphene is observed only at finite ($10^2 - 10^3$ V/cm) field strengths (see discussion below).

5.2 Time-dependent Dirac equation

In the previous section we obtained the equations of motion of classical relativistic electrons. Let us now understand the response of graphene under the application of an arbitrary in-plane field $\vec{E}(t)$ by solving the more general case of the time-dependent Dirac equation for massive fermions (TDDE):

$$i\hbar\frac{\partial}{\partial t}\psi = v_F \begin{pmatrix} \Delta & pe^{-i\theta_{\vec{p}}} + |e|\vec{A}(t) \\ pe^{i\theta_{\vec{p}}} + |e|\vec{A}(t) & -\Delta \end{pmatrix} \psi, \tag{5.12}$$

where $\Delta = mv_F$, and the band gap at the Dirac point is $E_g = 2mv_F^2$ [see section 2.2], $\vec{A}(t)$ is the vector potential, and $\theta_{\vec{p}}$ is the directional angle of the electron momentum, i.e. $\theta_{\vec{p}} = \arctan(p_x/p_y)$. Within the Dirac picture we use the Fermi velocity $v_F^D = 10^6$ m/s. In the field-free case, the solution of the TDDE follows trivially from the solution of the stationary equation [Eq.(2.5)]:

$$\psi_\xi(\vec{p}) = \sqrt{\frac{p_\xi - \Delta}{2p_\xi}} \begin{pmatrix} \frac{p}{p_\xi - \Delta} e^{-i\theta_{\vec{p}}/2} \\ e^{-i\theta_{\vec{p}}/2}. \end{pmatrix}, \tag{5.13}$$

multiplied by the corresponding phase

$$e^{iE_\xi t/\hbar}, \tag{5.14}$$

where $\xi = \pm 1$ is the band index and $E_\xi = \xi v_F\sqrt{\Delta^2 + p^2}$. For non-zero field we first consider the case of a field linearly polarized along the x direction and an electron momentum parallel to the field, i.e. $\vec{p} = (p_x, 0)$. In this case, the TDDE has an analytic solution [106, 114]:

$$\psi_\xi(t) = \psi_\xi(p_x, 0)\exp\left(-i\xi\frac{v_F}{\hbar}\int\sqrt{(p_x + |e|A_x(t))^2 + \Delta^2 dt}\right), \tag{5.15}$$

where $\psi_\xi(p_x, 0)$ is given by Eq.(5.13). The solution is similar to the field-free case, however, with a modified temporal phase due to the time-dependence of the Hamiltonian. We can extend the solution above to an arbitrary in-plane field and an arbitrary electron momentum. To do this, we expand the single-electron wave function as:

$$\psi(t) = \sum_\xi C_\xi(t)\psi_\xi(t), \tag{5.16}$$

where

$$\psi_\xi(t) = \psi_\xi(\vec{p})\exp\left(-i\xi\phi(t)\right), \tag{5.17}$$

and the temporal phase is

$$\phi(t) = \frac{v_F}{\hbar} \int \sqrt{(p_x + |e|A_x(t))^2 + (p_y + |e|A_y(t))^2} dt. \tag{5.18}$$

Substituting this expansion [Eq.(5.16)] into the TDDE [Eq.(5.12)] yields a system of differential equations for the coefficients $C_\xi(t)$. For the case of massless Dirac fermions, i.e. $\Delta = 0$, it reads [106]:

$$\dot{C}_\xi(t) = \frac{i}{2}\dot{\theta}_{\vec{p}} C_{-\xi}(t) e^{2i\xi\phi(t)}. \tag{5.19}$$

The differential equations for the fermions with a finite mass, i.e. $\Delta \neq 0$ are more difficult. We therefore numerically solve the time-dependent Dirac equation [Eq.(5.12)] directly by searching for a solution in terms of a time-dependent spinor

$$\psi(\vec{p}, t) = \begin{pmatrix} a(\vec{p}, t) \\ b(\vec{p}, t) \end{pmatrix}. \tag{5.20}$$

After substituting this wave function into the TDDE [Eq.(5.12)], we arrive at another system of differential equations, which we solve numerically:

$$\begin{cases} \frac{i\hbar}{v_F}\dot{a} & = \Delta a + [p_x + |e|A_x(t) - i(p_y + |e|A_y(t))]\, b, \\ \frac{i\hbar}{v_F}\dot{b} & = -\Delta b + [p_x + |e|A_x(t) + i(p_y + |e|A_y(t))]\, a. \end{cases} \tag{5.21}$$

Despite the use of Eq.(5.21) in the numerical treatment, the analytical solution Eq.(5.17) is still very useful for understanding the essence of electron dynamics in graphene. We will use it later along with the full numerical solution of Eq.(5.21).

5.2.1 Single-electron currents in the TDDE

We study electron dynamics by solving the TDDE numerically [Eq.(5.21)] and by analyzing the single-electron current given by [106]

$$\vec{j}(t) = (j_x(t), j_y(t)) = v_F \langle \psi(t) | (\sigma_x, \sigma_y) | \psi(t) \rangle, \tag{5.22}$$

where $\sigma_{x,y}$ are the Pauli matrices. We start our discussion with the simplest case of massless Dirac fermions ($\Delta = 0$) subject to a linearly polarized laser field and moving parallel to the field, i.e. $p_y = 0$. In this case the analytical solution [Eq.(5.15)] of the TDDE reads:

$$\psi_\xi(t) = \exp\left(-i\xi\frac{v_F}{\hbar}\int (p_x + |e|A_x(t))dt\right) \begin{pmatrix} e^{-i\frac{\pi}{4}(1-\mathrm{sgn}(p_x))} \\ \xi e^{i\frac{\pi}{4}(1-\mathrm{sgn}(p_x))} \end{pmatrix}. \tag{5.23}$$

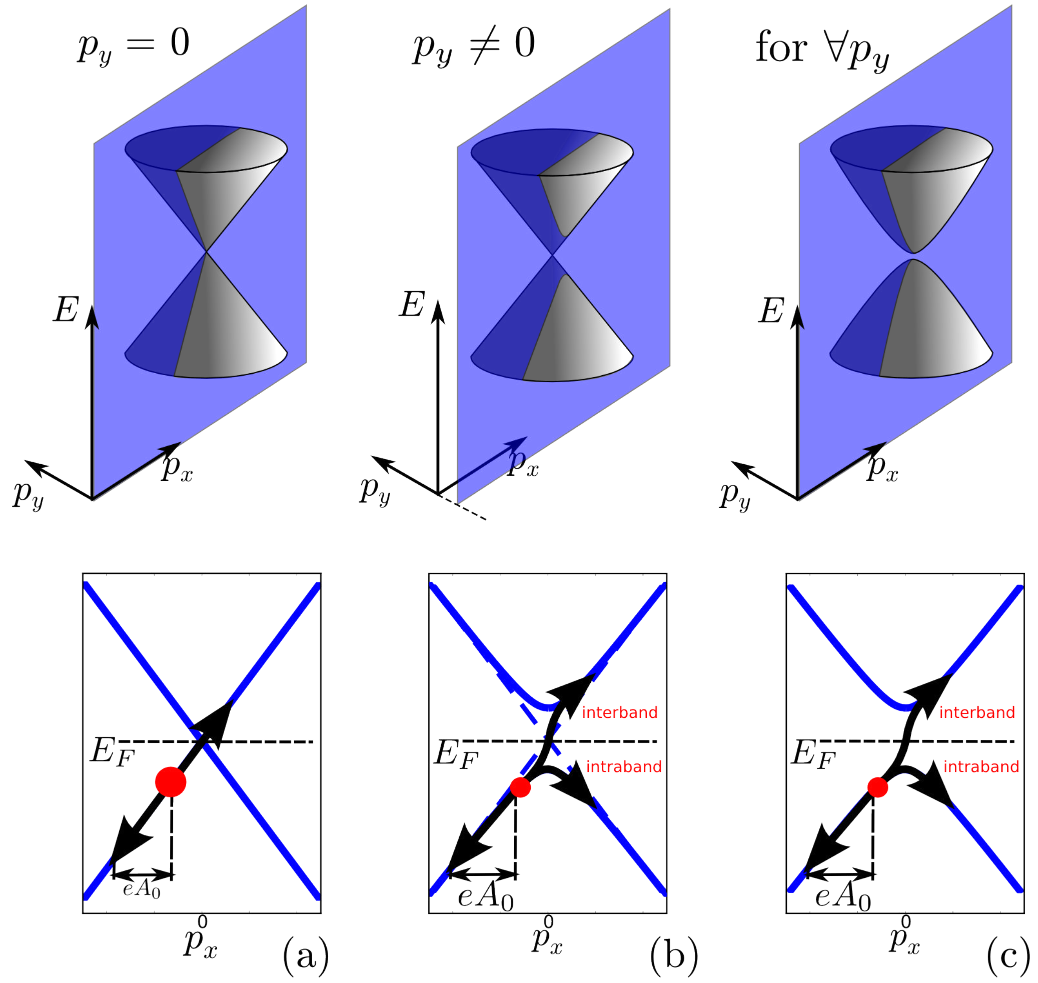

FIGURE 5.2: Schematic electron motion on the Dirac cone with different initial momenta and mass: (a) $p_y = 0$ and $m = 0$; (b) $p_y \neq 0$ and $m = 0$; (c) arbitrary p_y and $m \neq 0$ results in a finite energy gap at the Dirac point. The top row of figures shows the 2D energy dispersions. The bottom row of figures displays cross-sections of the Dirac cones with $p_y = \text{const}$ plane.

It is easy to find the current using this analytical form of the wave function for the conductance or the valence band

$$\vec{j} = (\xi, 0)v_F. \tag{5.24}$$

The current is obviously conserved and shows no response, as electrons with $p_y = 0$ undergo a complete population inversion and, therefore, a constant velocity when passing the Dirac point [see Fig.5.2(a)].

The situation is different for $p_y \neq 0$. For states with an initial energy $|E| = v_F\sqrt{p_x^2 + p_y^2}$ larger than the maximal energy a particle can pick up from the pulse, i.e. $E_c = v_F|e|A_0$, where A_0 is the strength of the vector potential of the laser, the dynamics is governed by the electron motion within one band, which is referenced to as the *intraband* current. For smaller p_y and $|E| \lesssim E_p$, the electron can be excited to the conduction band through interband Landau-Zener tunneling [115] inducing *interband* polarization and, therefore, an *interband* current. The tunneling probability [115] depends exponentially on the smallest energy gap (ΔE) between the two cones at the $p_y = \text{const}$ conical intersection [see Fig.5.2(b)]:

$$P = \frac{|e|a\omega A_x}{h} e^{-\alpha \Delta E^2/\omega A_x}, \tag{5.25}$$

where $\alpha = \pi^2 m_e a/h^2|e|$ and a is the periodicity of the graphene unit cell. This probability P is exponentially small for large p_y (and, therefore, large ΔE) and the effect of *interband* polarization can be neglected. The dynamics of Dirac fermions having a linear dispersion with a finite band gap E_g is qualitatively similar [see Fig.5.2(c)]

To be more quantitative, suppose we know the solution of the TDDE [Eq.(5.12)] for the coefficients C_ξ [Eq.(5.19)] of the wave function expansion in Eq.(5.16). These coefficients convey the evolution of the population in each band, which we describe by introducing the population difference $n = |C_+|^2 - |C_-|^2$, and the interband coherence $\rho = C_+ C_-^*$. The single-electron current for any arbitrary p_y is then given by [106]

$$\begin{aligned} j_x(t) &= v_F \left(n \cos\theta_{\vec{p}} + i \sin\theta_{\vec{p}} [\rho e^{-2i\phi(t)} - \rho^* e^{2i\phi(t)}] \right), \\ j_y(t) &= v_F \left(n \sin\theta_{\vec{p}} - i \cos\theta_{\vec{p}} [\rho e^{-2i\phi(t)} - \rho^* e^{2i\phi(t)}] \right), \end{aligned} \tag{5.26}$$

where the first term describes the intraband current and the last two terms describe the interband polarizations. Notably, at $t = 0$ the current $j_x(t = 0)$ ($j_y(t = 0)$) is proportional to the cosine (sine) of the directional angle. If we neglect interband tunneling processes by neglecting the second term in Eq.(5.26) and setting the population to only one band $n = \xi$, we obtain an intraband current

$$j_x = \xi v_F \frac{p_x + eA_x(t)}{\sqrt{(p_x + eA_x(t))^2 + (p_y + eA_y(t))}}, \tag{5.27}$$

which coincides with the classical solution in Eq.(5.7) as expected.

In order to test the solution of the time-dependent Dirac equation, we consider the particular example of a few-cycle THz pulse linearly polarized along x [Fig.5.3]: $A_x(t) \equiv A(t) = A_{\text{env}}(t)\sin(2\pi\nu t)$. We model a $\nu = 2$ THz pulse with a period $T = 0.5$ ps and the envelope:

$$A(t) = A_0(t) \begin{cases} \exp\left(-\frac{(t-1.1T)^2}{(0.67T)^2}\right), & \text{if } \ t <= 1.1T; \\ \exp\left(-\frac{(t-1.1T)^{2.7}}{(0.47T)^{2.7}}\right) & \text{otherwise}, \end{cases} \tag{5.28}$$

where the amplitude of the vector potential $A_0 = E_0/2\pi\nu$ is proportional to the laser field strength E_0 and inversely proportional to the laser frequency $\omega = 2\pi\nu$. The pulse shape is chosen to resemble the experimental pulse used for observation of nonlinear harmonics in [21].

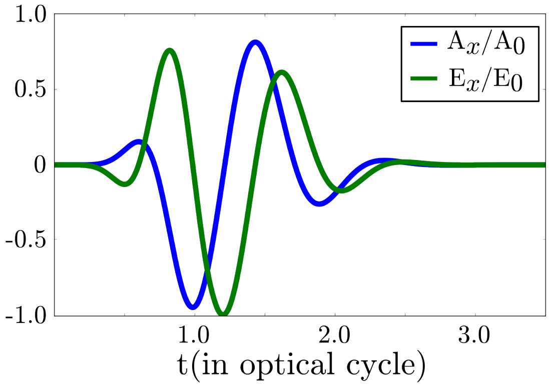

FIGURE 5.3: The normalized electric field (green) and vector potential (blue) of a 2 THz linearly polarized laser pulse following the experiment [21].

5.2.2 Examples of single-electron currents

To provide examples of the solutions of the TDDE, we calculate the response of massless Dirac fermions located in the valence band at $t = 0$ with different initial momenta and energies: (i) with $p_y = 0$; (ii) with $p_y \neq 0$ and near the Dirac point $E \approx 0$, i.e. with energy much less than the maximal energy a particle can gain from the laser field $E_c = -v_F|e|A_0$; (iii) with energy $E \approx E_c$ and $p_y \ll p_x$; (iv) far away from the Dirac point $E \ll E_c$. In the first case of $p_y = 0$, the solution of the Dirac equation yields a constant current [red line in Fig.5.4(a)] in line with the analytical prediction [Eq.(5.24)]. In this situation the response is governed by the interband dynamics. This is in contrast to the pure intraband current [Eq.(5.27)], which changes sign at the Dirac point for an electron to stay within the valence band [green square wave in Fig.5.4(a)]. The windowed Fourier transform (WFT) [see Appendix A] of the calculated total wave function [Fig.5.4(b)] confirms our analysis of total population inversion at the Dirac point, i.e. $E = 0$, which is the reason of the constant current. The particle trajectory in energy space alternates smoothly between the corresponding intraband trajectories $E_{\pm}(t) = \xi v_F\,|p_x + |e|A(t)|$, determined by the energy evolution of a relativistic electron driven by the laser field, in the lower [black-white curve in Fig. 5.2(b)] and upper [white-dashed curve in Fig. 5.2(b)] cones. The wave function of an electron moving only within the valence band can be calculated using Eq.(5.17) for $\xi = -1$. The windowed Fourier transform of this intraband wave function coincides with the intraband energy evolution in the valence band [black-white lines in Fig.5.4(c)] and shows a sharp change of the trajectory in momentum (energy) space at the Dirac point.

The current corresponding to the initial states (ii) and (iii) with $p_y \neq 0$ and $E \lesssim E_c$ [see red curves in Fig.5.4(d) and (g)] strongly deviates from the corresponding intraband current [see green curves in Fig.5.4(d) and (g)] and the constant current of the (i) case when $p_y = 0$. Moreover, it oscillates due to the presence of two parts of the wave packet simultaneously propagating in the valence and the conduction bands and acquiring opposite phases. The intraband response does not show these oscillations as the electron follows the classical pathway in the energy space while moving in the valence band only [see Fig.5.4(f) and (i)]. The interband polarization appears as a result of the Landau-Zener tunneling between the two bands at the point where the wave packet in the energy space travels through the Dirac point. Part of the wave packet then propagates within in the upper band [white dashed curves in Fig.5.4(e) and (h)] while the other portion of the wave packet still follows the classical trajectory $E(t)$ in the lower band [black-white dashed curves in Fig.5.4(e) and (h)]. Their superposition results in a beating of current with frequency $2\phi(t)$ [Eq.(5.33)], since the two parts of the wave packet acquire phases of opposite sign $e^{i\phi(t)}$ and $e^{-i\phi(t)}$ while moving on the valence and the conduction cones [Eq.(5.17)]. The oscillations are time-dependent and their frequency $\Omega(t) = \dot{\phi}(t) = (E_+(t) - E_-(t))/\hbar = 2E(t)/\hbar$ follows the evolution of the energy difference between the two pathways. The analytical solution [Eq.(5.26)] predicts oscillations in the current with this frequency [second term in Eq.(5.26)].

In the last case (iv) when $p_x, p_y \gg 0$ and $E \gg E_c$ the calculated current [red curve in Fig.5.4(j)] and intraband current [green curve in Fig.5.4(j)] coincide. In this case the windowed Fourier transforms of the wave function obtained from the full solution of TDDE and the intraband wave function [Eq.(5.27)] are the same [Fig.5.4(k) and (l)]. Indeed, far away from the Dirac point the interband polarizations as well as the tunneling probability [Eq.(5.25)] between the upper and lower cones approaches zero, and the electron dynamics is well approximated by the intraband contribution only.

All the considered examples show a highly nonlinear response of the current to the laser field. The anharmonic behavior of the current leads to the observed nonlinear response in terms of far-field radiation which we discuss in detail in section 5.4.

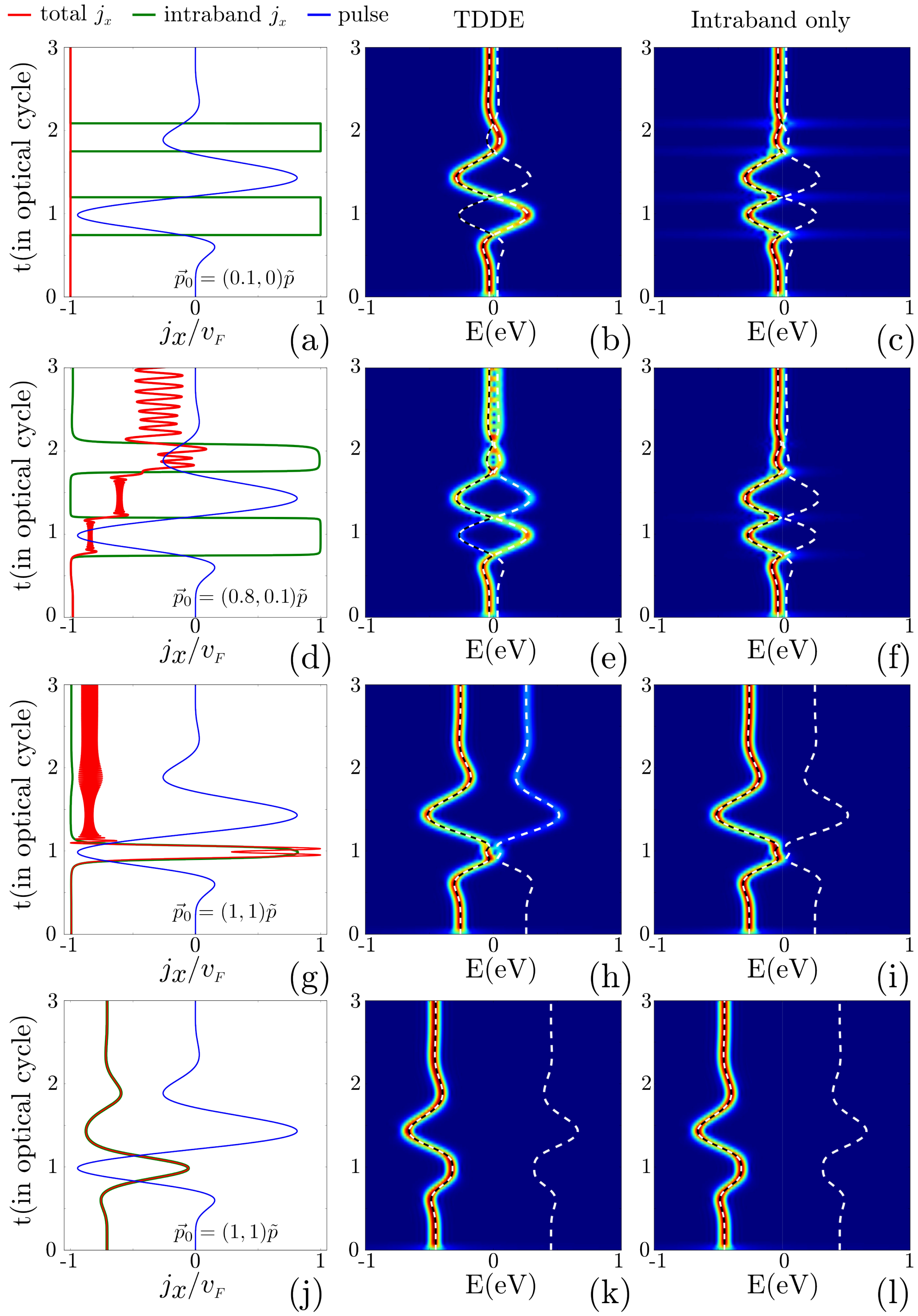

FIGURE 5.4: (a), (d), (g), (j) Red and green curves correspond to the single-electron currents calculated within the TDDE and intraband currents for different initial conditions: (a-c) $\vec{p}_0 = (0.1, 0)\tilde{p}$; (d-f) $\vec{p}_0 = (0.1, 0.02)\tilde{p}$; (g-i) $\vec{p}_0 = (0.8, 0.1)\tilde{p}$; (j-l) $\vec{p}_0 = (1.0, 1.0)\tilde{p}$, where $\tilde{p} = |e|A_0$ is the maximal momentum an electron can gain from the laser vector potential with an amplitude A_0. Windowed Fourier transform of the wave function (b), (e), (h), (k) and the intraband wave function (c), (f), (i), (l). Black-white and white dashed curves correspond to the classical trajectory in energy (or momentum) space [Eq.(5.6)] for the electron motion in the valence and the conduction bands respectively.

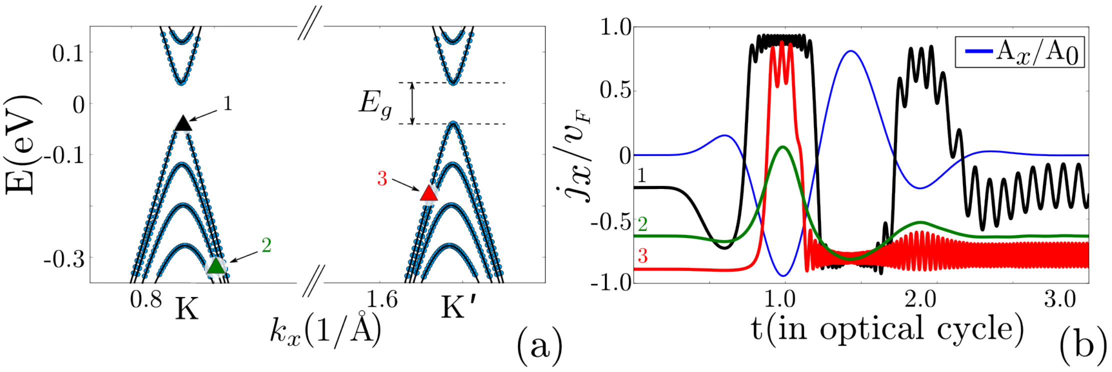

FIGURE 5.5: (a) Eigenstates of a $L_x \times L_y = 250 \times 25$ nm^2 flake with periodic boundary conditions in x-direction and screened zigzag boundaries parallel to the x-axis (blue dots). Black curves correspond to the bandstructure of the infinite ZGNR of the same width L_y with screened boundaries. The bandstructure of the flake revels a bandgap $E_g \approx 64$ meV. Green, black and red triangles denote the eigenstates, for which we show the single-electron current in (b) calculated within TDTB. Blue curve in (b) represents the renormalized vector potential of the laser.

5.3 Time-dependent tight-binding approximation

Another way to approach the problem of the electron dynamics in graphene is to solve the time-dependent Schrödinger equation with the third-nearest-neighbor tight-binding Hamiltonian [section 2.3]:

$$i\hbar\frac{\partial}{\partial t}\psi(t) = H_{TB}\psi(t) \tag{5.29}$$

We will apply the time-dependent tight-binding approximation (TDTB) to large finite size structures to approximate the behavior of bulk graphene. The great advantage of the method is the opportunity to study the influence of disorder or a substrate on the response of graphene. We include the laser pulse through its vector potential (velocity gauge) using the Peierls phase factor [Eq.(2.46)]. We solve the Schrödinger equation [Eq.(5.29)] numerically using a Short Iterative Lanczos propagator (SIL) [116] [see Appendix B]. The SIL is a powerful method for finding the wave function described by a complex vector for a Hamiltonian given by a large, sparse matrix. SIL propagates the wave function at each time step, allowing for variations in the time-steps for the time-dependent Hamiltonian.

5.3.1 Single-electron currents in the TDTB

As the single-electron response in the TDTB approximation applied to a finite size graphene flake we consider the evolution of an n^{th} eigenstate $\psi_n(t)$ in a laser field.

A single-electron current is then determined by the quantum mechanical probability current:

$$j_x^n(t) = \frac{1}{2m}\left\{-i\hbar\left(\psi_n(t)^*\frac{\partial}{\partial t}\psi_n(t) - \psi_n(t)\frac{\partial}{\partial t}\psi_n(t)^*\right) + 2|e|A_x|\psi_n(t)|^2\right\}. \tag{5.30}$$

To provide a numerical example, we first calculate the eigenstates of a rectangular graphene flake with dimensions $L_x \times L_y = 250 \times 25$ nm^2 with periodic boundary conditions in x-direction, i.e. the pulse polarization direction. We screen the zigzag edges parallel to the x-direction with a Berry-Mondragon potential [86] to avoid the high density of edge states at the Dirac point. The eigenstates of the flake in the field-free case [Fig.5.5(a) blue points] feature two inequivalent K and K' Dirac cones and closely resemble the bandstructure of the infinite zigzag graphene nanoribbon of the same width L_y with likewise screened edge [see black curves in Fig.5.5(a)] also calculated within the third-nearest-neighbor tight-binding approach. To resolve the eigenstates of the flake as a function of k_x, we calculated the Fourier transform of the corresponding eigenfunction [as described in section 2.8]. We then find k_x as a local maximum of the Fourier transform near each cone and assign one eigenstate to k_x near K and another one to k_x' near K' in order to disentangle the two degenerate states near K and K'. It is evident that, unlike the solution of the TDDE where the initial single-electron wave function can have any momentum of the continuous Dirac spectrum, the eigenstates of the flake allow for probing of the electron dynamics only for discrete values of momentum. Moreover, in the distribution of eigenstates, we observe a clear size quantization in y-direction and a band gap $E_g = 64$ meV [Fig.5.5(a)]. The effect of the size quantization and the finite band gap can be reduced by increasing the flake size at additional computational cost.

For the chosen parameters of the flake, the single-electron currents [Fig.5.5(b)] reveal similar features to those discussed in subsection 5.2.1 for the single-electron currents calculated within the TDDE [Fig.5.4(a, d, g, j)]. In particular, for an initial state $\psi_n(t=0)$ corresponding to an eigenstate of the flake away from the Dirac point [marked by a black triangle in Fig.5.5(a)], we observe the suppression of the interband response, and the dynamics is governed by the intraband motion [see black curve in Fig.5.5(b)]. For the initial states $\psi_n(t=0)$ in the vicinity of the Dirac point [marked by red and green triangles in Fig.5.5(a)], the laser-induced tunneling between the cones creates an interband polarization, which we observe as high frequency oscillations in the current [see green and red curves in Fig.5.5(b)]. However, the response of graphene calculated using the TDDE and the TDTB are different due to differences in the band structure, i.e. the presence of size-quantization and a non-zero band gap in our tight-binding approach.

5.4 Simulation of the experiment: TDDE versus TDTB

The physical observable in the experiment [21] was the far-field response of graphene, which clearly revealed the presence of the odd harmonics in the power spectrum. The electromagnetic field generated by the moving charges in graphene due to the interaction with the laser pulse is determined by the dipole acceleration of the charge carriers $\ddot{\vec{d}}(t)$ in the far-field approximation. The squared Fourier transform of the dipole acceleration yields the power spectrum:

$$P(\omega) \propto \left|\ddot{\vec{d}}(\omega)\right|^2 = \left|\omega\dot{\vec{d}}(\omega)\right|^2. \tag{5.31}$$

Since both current and first derivative of the dipole moment are proportional to the velocity, we can equivalently write

$$P(\omega) \propto \left|\omega\vec{J}(\omega)\right|^2, \tag{5.32}$$

where $\vec{J}(\omega)$ is a Fourier transform of the total current given by [114]

$$\begin{aligned} \vec{J}_{TDDE}(t) &= \frac{n_s n_v |e|}{(2\pi\hbar)^2} \int \vec{j}_{\vec{p}}(t) d\vec{p}, \\ \vec{J}_{TDTB}(t) &= n_s |e| \sum_n \vec{j}_n(t), \end{aligned} \tag{5.33}$$

with $n_s = 2$ and $n_v = 2$ the spin- and valley-multiplicity. We assume that at $t = 0$ electrons in graphene occupy the valence band up to the Dirac point, i.e. $E_F = 0$. The states in the conduction band are empty. The single-electron current $\vec{j}(t)$ is calculated either by solving the TDDE or the TDTB. The integration is performed over the uniform momentum distribution $\vec{p}$ for the TDDE or by summation over the eigenstates of a graphene flake for the TDTB. We consider electrons in the valence band with energies $0 \le E \le -0.33$ eV at $t = 0$ to capture all the states reaching the Dirac point for the pulse strengths we examine. We focus only on the far-field response parallel to the polarization axis of the laser, i.e. we evaluate $\vec{J}_x$ and calculate the power spectrum $P(\omega)$ only for this component of the total current. The y component of the current is zero for a symmetric distribution of p_y.

The power spectrum [Eq.(5.32)] of the integrated intraband response [see Fig.5.6 (a-e)] calculated using Eq.(5.27) shows the formation of the third and the fifth harmonics starting from the field strength of $E_0 \approx 20$ kV/cm. The harmonic strengths grow with laser intensity. The power spectrum of the integrated current [Eq.(5.33)] calculated using the TDDE for massless fermions [Eq.(5.21)] is similar to the intraband response [see Fig.5.6 (f-j)] but has more structure due to the additional interband polarizations.

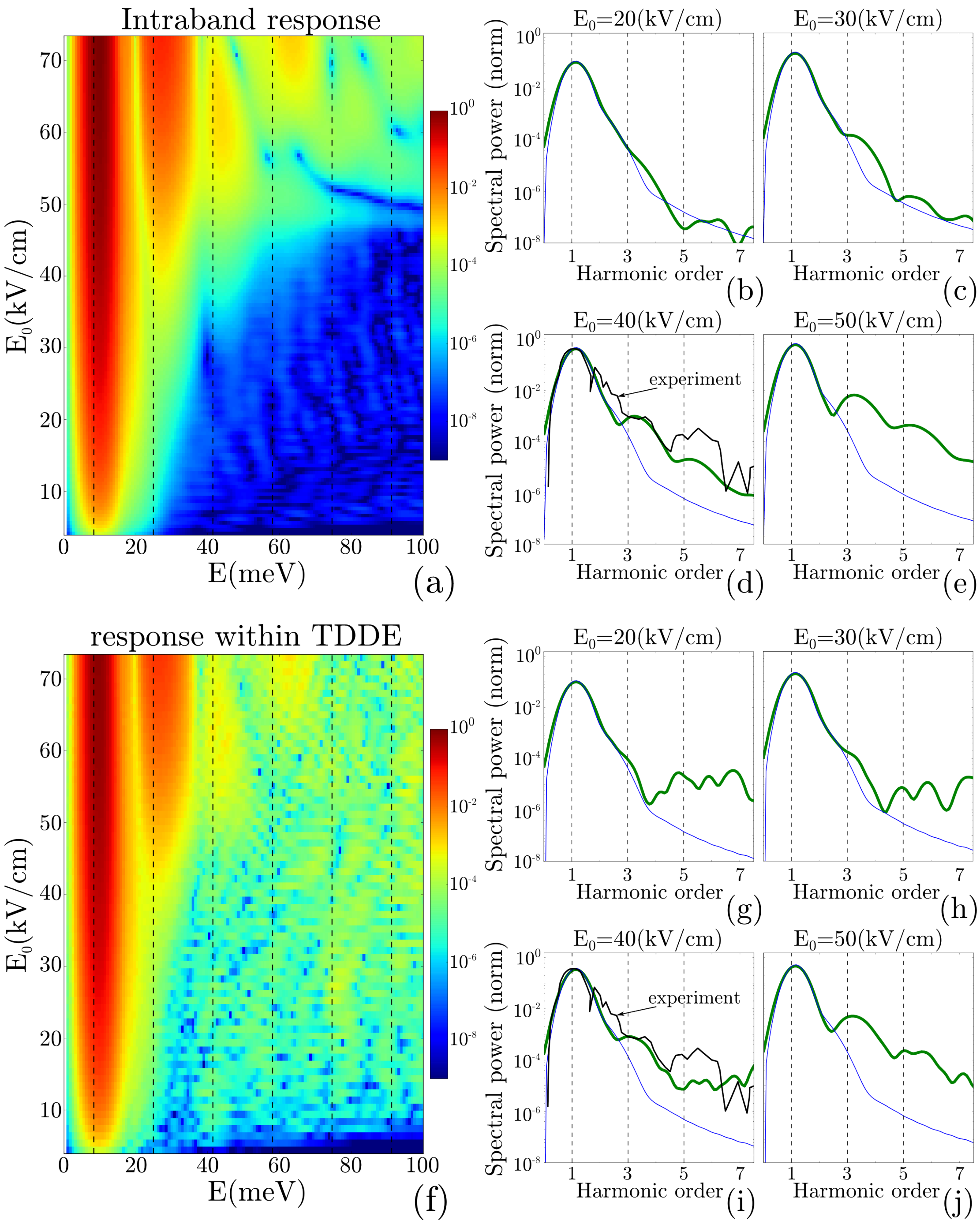

Figure 5.6: (a) Nonlinear far-field intraband response represented by power spectrum [Eq.(5.32)] (in color) as function of laser field strength and harmonic energy. Vertical dashed lines denote the low odd harmonics. (b-e) The cuts through (a) for different field strengths: (b) $E_0 = 20$ kV/cm, (c) $E_0 = 30$ kV/cm, (d) $E_0 = 40$ kV/cm and (e) $E_0 = 50$ kV/cm. (f) Same as in (a-e) but for the power spectrum evaluated within the TDDE, which includes both intraband and interband contributions. In all figures, the blue curves are the power spectrum of the pulse itself and the black curves represent the measured response adapted from [21].

In particular, the interband current leads to a stronger nonlinear response at low fields in comparison with the intraband contributions. The onset of odd harmonic generation

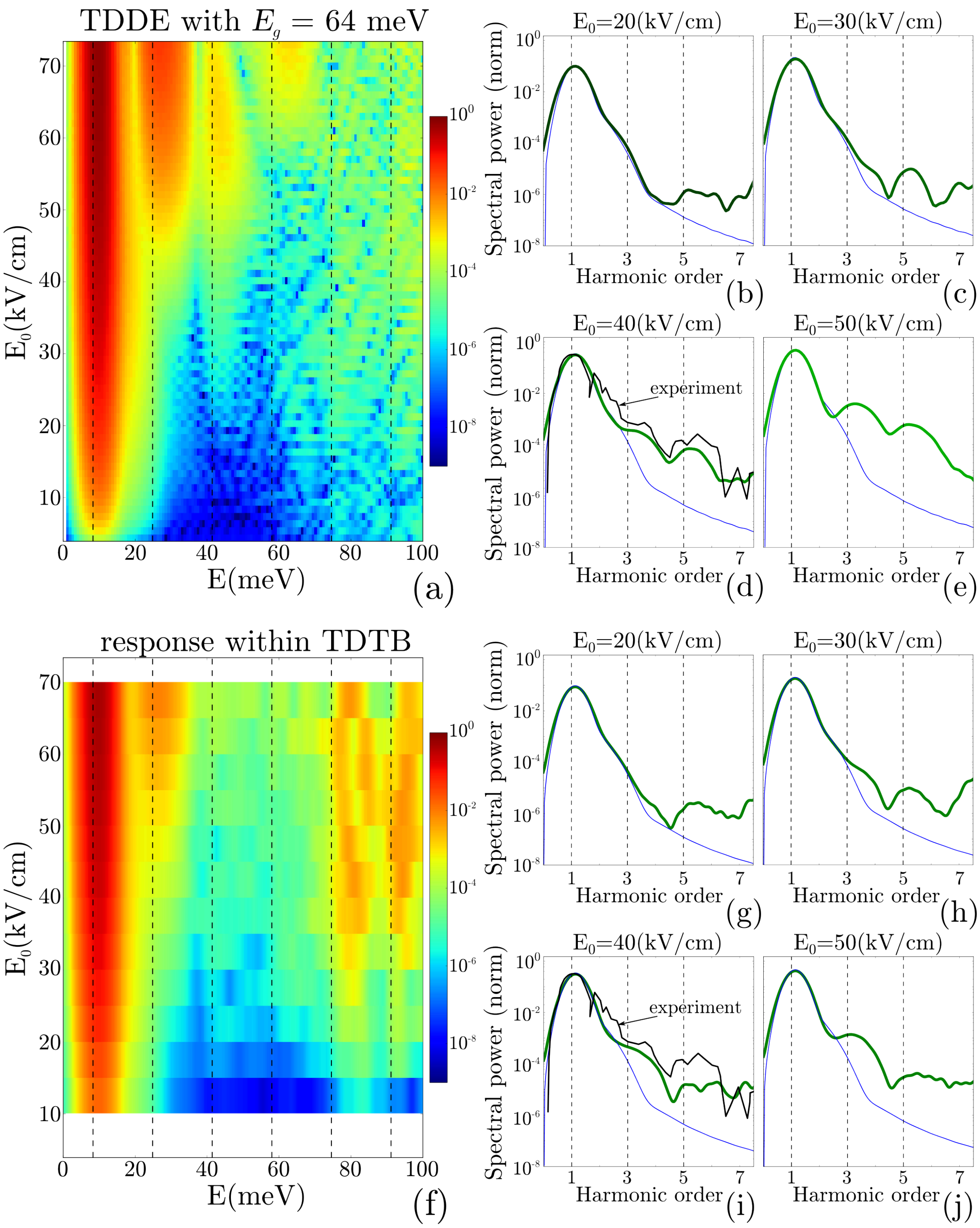

FIGURE 5.7: Same as in Fig.(5.6), but for nonlinear responses evaluated by solving TDDE with a finite band gap E_g = 64 meV (a-e) and for nonlinear responses evaluated within TDTB (f-j). Vertical dashed lines denote the low odd harmonics.

is again at about $E_0 \approx 20$ kV/cm. The nonlinear response becomes more pronounced if we calculate the power spectrum of the integrated current [Eq.(5.33)] using the TDDE with a band gap of $E_g = 2v_F\Delta = 64$ meV [see Fig.5.7 (a-e)] as compared to the response of massless Dirac fermions [see Fig.5.6 (f-j)]. Obviously, the presence of the gap reduces the interband polarization, which is responsible for the fluctuations in the signal. The solution of the TDDE for the fermions with finite mass can be compared

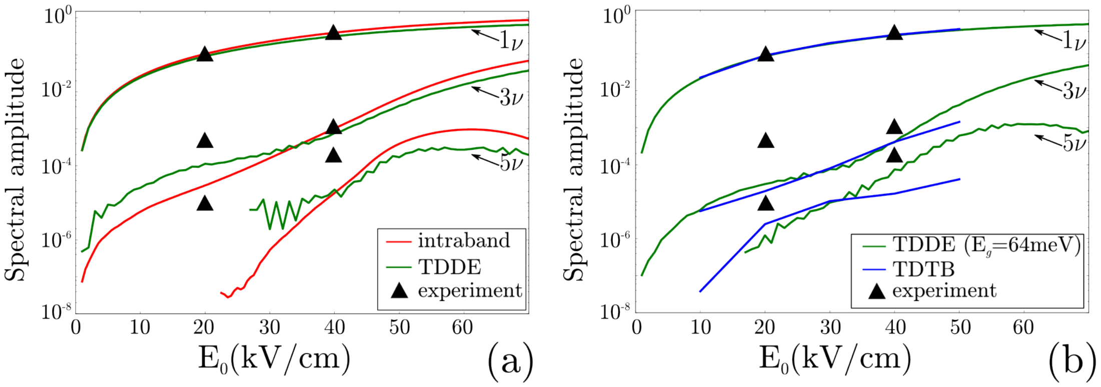

Figure 5.8: (a) First, third and fifth harmonic intensities as function of laser field strength of the intraband response (red) and the response calculated within the TDDE (green). (b) Same as (a), but for the low harmonic response determined within the TDDE for electrons with a finite mass due to a band gap $E_g = 64$ meV in the energy dispersion (green) and the response calculated within TDTB (blue).

with the solution of the TDTB equation [Eq.(5.29)] applied to the finite size ribbon [see Fig.5.7(f-j)], since the ribbon also features a band gap of ≈ 64 meV [see the eigenstates of the ribbon in Fig.(5.5)(a)]. We again observe a qualitatively similar behavior between these two approaches. However, in the power spectrum of the TDTB we find larger intensities at 70-100 meV, which correspond to dipole excitations between the different subbands of the ribbon [see Fig.5.5(a)]. We finally compare odd harmonic intensities as function of the laser field strength calculated with different methods [see Fig.5.8]. We find comparable harmonic behavior as function of pulse amplitude. The experimental values of the harmonic intensities [black triangles in Fig.5.8], taken from [21] and normalized to the first harmonic of the TDDE response at 40kV/cm, are in reasonable agreement with the calculated response.

We emphasize the excellent overall agreement of all the calculations with the experimental power spectrum for the field strength of $E_0 = 40$ kV/cm [21] [compare the calculated power spectrum in green with an experiment in black in Fig.5.6 (d),(i) and Fig.5.7 (d),(i)]. The only adjustable parameter is the overall normalization to the peak intensity of the linear response, i.e. the first harmonic. There are, however, several noticeable deviations. First of all, the methods underestimate the intensity of the fifth harmonic, which we explain in the following section as a result of non-zero doping of the samples. Secondly, the experimental data shows the presence of the second harmonic. The second-order nonlinearity appears due to the presence of disorder, for example grain boundaries, edges, vacancies etc., which allow for local inversion symmetry breaking resulting in the back scattering of the laser driven electrons in real space. In the next subsections we, therefore, provide a thorough discussion of the influence of non-zero doping [subsection 5.4.1] and disorder [subsection 5.4.2]. We consider the effect of short- and long-range disorder within the TDTB approximation.

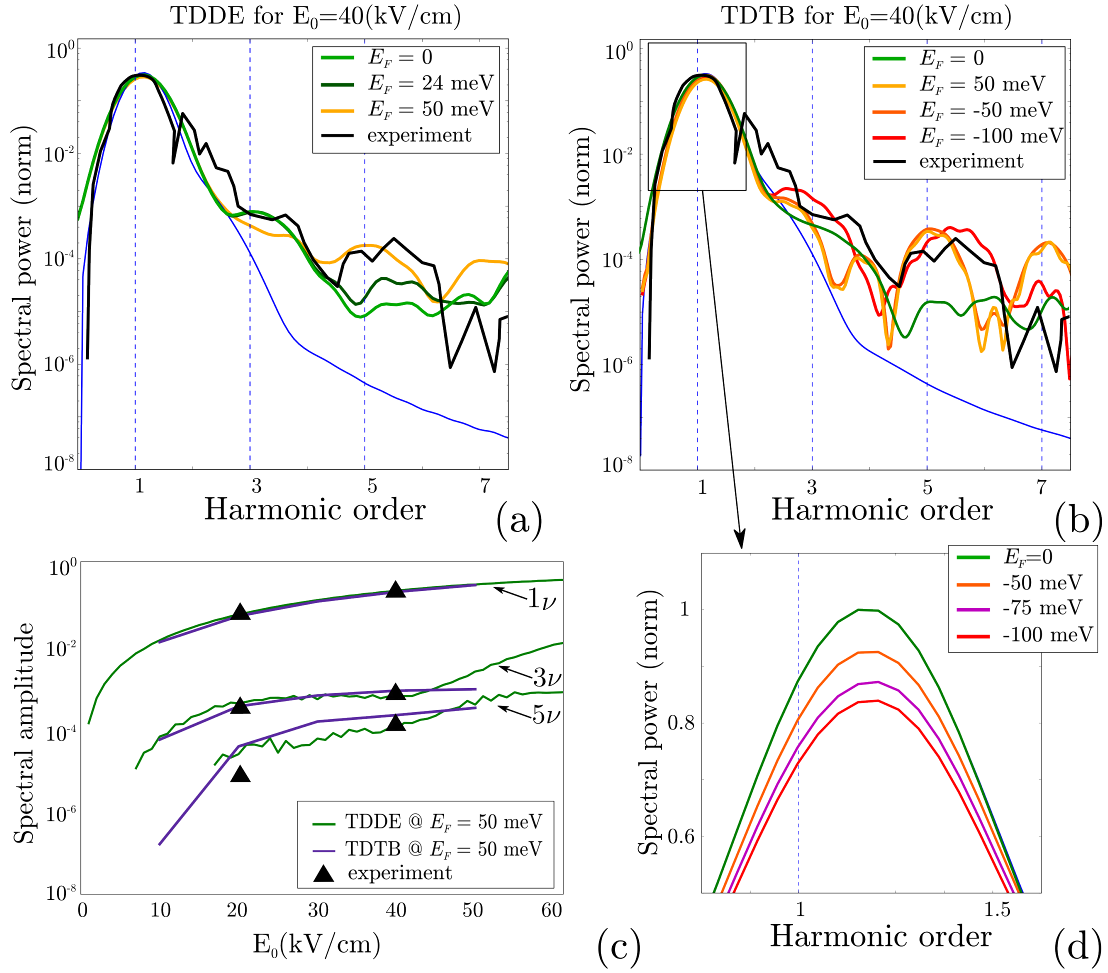

FIGURE 5.9: Specttal power of the nonlinear harmonic response of graphene at different doping levels for $E_0 = 40$ kV/cm laser pulse. The response is evaluated within (a) TDDE and (b) within TDTB. The blue curves are the power spectrum of the pulse itself and the black curves represent the measured response adapted from [21]. (c) First, third and fifth harmonic intensities as function of laser field strength for the response evaluated within TDDE with a band gap $E_g = 64$ meV (green) and within TDTB (violet) at the Fermi level of 50 meV. (d) Zoom in of the first harmonic in (b) for different amount of doping, i.e. E_F.

5.4.1 Influence of doping

All the calculations above were performed for zero doping of graphene, as we considered only the occupied states up to the Dirac point, and Fermi energy $E_F = 0$. In the experiment, however, this is not the case due to finite doping of the samples. The influence of the doping on the harmonic intensities can be large. The response near the Dirac point is very sensitive to interband polarizations, which may lower the harmonic intensities. By changing the doping or by changing E_F this high frequency interband-induced oscillations in the current can be reduced and stronger intraband signal with higher odd harmonics can be observed. The influence of doping was theoretically considered in [105] while solving the kinetic Boltzmann equation. Al-Naib et al. [104] examined the maximization problem of the emitted third harmonic as a function of Fermi energy for the intraband response. In this subsection we follow up on this discussions and calculate the response of graphene within the TDDE and the TDTB approximations at $E_0 = 40$ kV/cm for different values of E_F [see Fig.5.9(a,b)]. Within our single-electron picture, we calculate the total current [Eq.(5.33)] by integrating over k-space including electron energies up to E_F in the TDDE approach (in the same way as we did for $E_F = 0$) and by summing the response of eigenstates with energies up to E_F in the TDTB.

The change in Fermi level has a dramatic influence on the harmonic spectra of the total current. In particular, we observe one to two orders of magnitude increase of the 5^{th} harmonic in both TDDE and TDTB solutions. Its amplitude becomes comparable with experiment upon changing E_F. This indirectly confirms the non-zero doping of the graphene samples used in [21]. However, in the experiment [21] a direct measurement of the doping was not possible. A doping level of $E_F = 24$ meV was deduced from fitting the measured signal to the Drude model. We also find a more pronounced 7^{th} harmonic as the doping level increases. The strength of the 7^{th} harmonic is maximal at $E_F \approx 50$ meV and decreases at higher E_F. Notably, the response for the same absolute value but different sign of the Fermi energy is very similar [compare, e.g., the responses for $E_F = 50$ meV and $E_F = -50$ meV shown as light orange and dark orange traces in Fig.(5.9)(b)]. In comparison to the evaluation of the integrated current for zero doping, i.e. $E_F = 0$, the summation in Eq.(5.33) excludes states with energies $-|E_F| > -|E| > 0$ for negative Fermi energies, while for positive Fermi energies states above the Dirac point with energies $0 < E < E_F$ are included in the sum. States with the same momentum and absolute value of the energy but belonging to upper and lower cones produce nearly identical currents with opposite sign (within the Dirac picture the current are exactly opposite) and, therefore, approximately cancel each other [see false color plor in Fig.5.10: currents for the states in the upper and the lower cones have opposite sign]. Therefore, the resulting current from the energy window $-|E_F| < E < E_F$ is nearly zero producing a negligible response. Since the difference between the currents evaluated for the occupied states up to $+|E_F|$ and up to $-|E_F|$ is the current produced by the states with $-|E_F| < E < E_F$, the integrated current does not change leading to the same nonlinear response for the opposite doping levels. The magnitude of the 3^{rd} and 5^{th} harmonics in our calculations agree well with the experiment when doping is taken into account [see Fig.5.9(c)]. Both, the TDDE and the TDTB methods give qualitatively and quantitatively very similar results: the harmonic strengths as a function of the field amplitude E_0 are comparable [see Fig.5.9(c)].

We also note a change in the intensity of the linear response [see close up of the first harmonic in Fig.5.9(d)]. The reduction of the first harmonic amplitude, i.e. linear response $j_x^{(1)}(\omega) = \sigma^{(1)}(\omega) E_x(\omega)$ [Eq.(5.9)] is correlated with the decrease of the amplitude of the total current. The decline of the total current with E_F or doping concentration obviously reduces the optical conductivity. This result, however, contradicts experimental observations [117] of a growing optical sheet conductivity with the applied back gate voltage outside of the charge neutrality point (CNP). The experiment [117] were performed on graphene grown by chemical vapor deposition and placed on SiO_2 with a Si substrate used as back gate. The optical conductivity was obtained by measuring the THz transmission amplitude through the graphene sample with different V_{bg} applied. The increase of the conductivity with the doping level away from the CNP was explained by a simple Drude model, which described classical electron transport: the conducting electrons move on straight trajectories in the solid between inelastic collisions with, for example, atoms in the lattice or other electrons (the exact scattering mechanism in the Drude model is unimportant). The optical conductivity within the Drude model in application to graphene reads [117]

$$\sigma(\omega) = \frac{e^2}{\hbar}\frac{2k_BT}{\pi\hbar}\left[\ln\left(e^{-E_F/k_BT} + e^{E_F/k_BT}\right)\right]\frac{1}{1/\tau - i\omega}, \tag{5.34}$$

where k_B is the Boltzmann constant, T is the temperature and τ is the scattering time. Near the CNP in the region of charge puddles and trap states [see also subsection 3.2.1], the optical conductivity remains constant and is proportional to T. Away from the CNP $\sigma(\omega) \sim E_F$. The Drude model includes effective scattering, which influences the collective electron dynamics. Therefore, the difference between the theory presented here and the experiment can be explained as a result of electron-electron, electron-phonon and other scattering mechanisms which we neglect completely.

5.4.2 Influence of disorder

Another issue we address is the presence of second-harmonic generation (SHG) in the experiment [21] The second-order nonlinear response to a linear polarized continuous laser field is

$$j_x^{(2)} = \sigma^{(2)} E_x E_x^*, \tag{5.35}$$

where $\sigma^{(2)}$ is the optical conductivity tensor describing second-order nonlinearity [see Eq.(5.9)]. This equation describes the so-called linear photogalvanic effect [118, 119]. In pristine graphene, i.e. with no local symmetry reduction due to bulk disorder or edges, the quadratic form $E_x E_x^*$ does not change its sign under parity transformation in contrast to the current. Therefore, the SHG is zero unless the lattice symmetry is broken, which leads to increased back scattering of electrons and hence the opposite to the direction of the field current flow. In our tight-binding simulations we can account for different types of disorder. Major candidates for local symmetry breaking in real

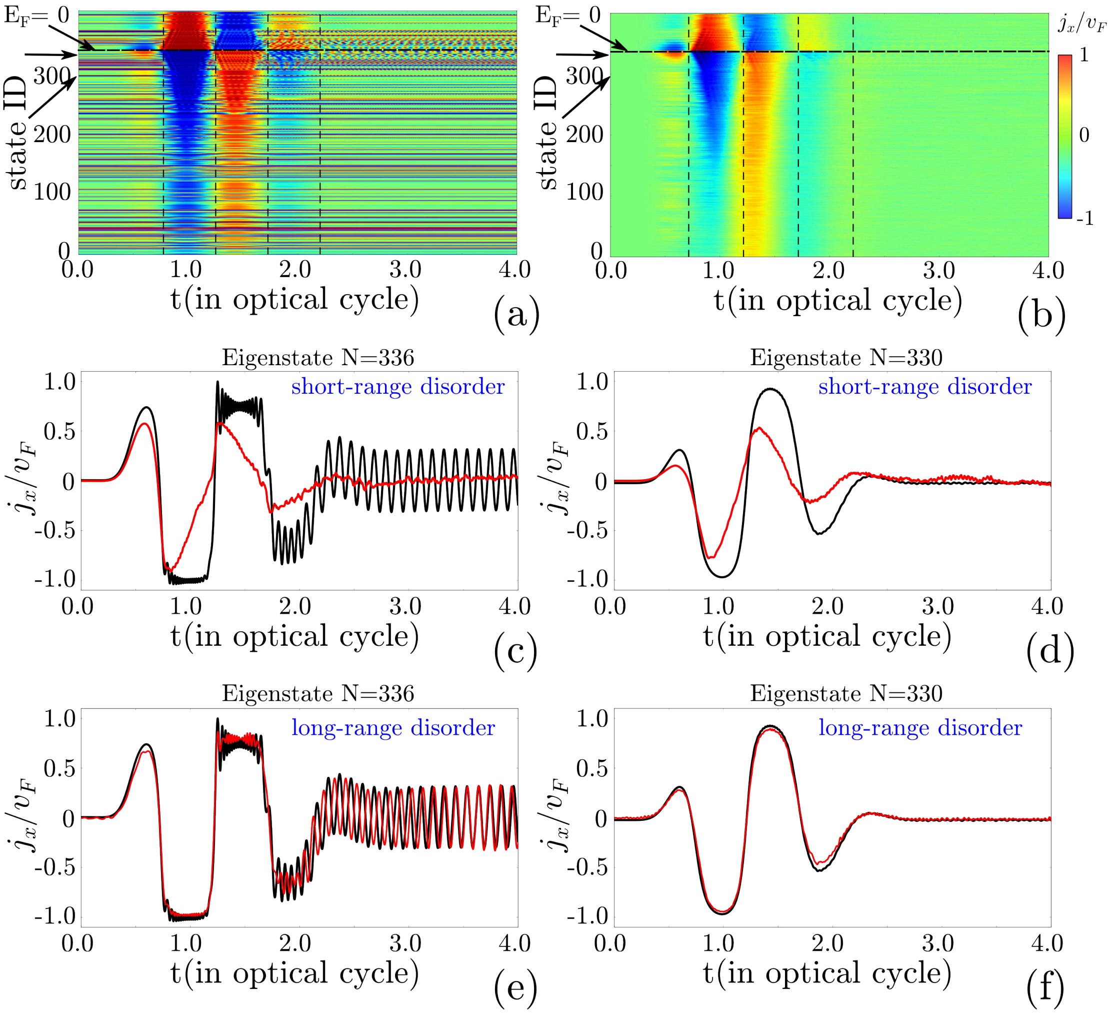

FIGURE 5.10: (a-b) Time evolution of single-electron currents (in color) corresponding to different eigenstates of a rectangular flake calculated within TDTB in the disorder-free case (a) and in the case of short-range disorder (b) simulated by adding single vacancies (with density $n_v = 1.3 \cdot 10^{-4}$Å^{-2}). (c-f) A comparison between the single-electron currents produced by the 330th (d,f) and 336th (c,e) eigenstate of the flake driven by the laser field. Black curves show the current in a disorder-free flake, whereas red curves correspond to the current in a flake with (c-d) short-range and (e-f) long-range (with correlation length l_{cor} = 10 nm and amplitude of 50 meV) types of disorder.

crystals are vacancies [54] (short-range disorder) and charge puddles [55] (long-range disorder). We calculate the response of a graphene flake in the presence of disorder to a laser pulse [Eq.(5.28)] for a laser intensity of 40 kV/cm using time dependent tight-binding (TDTB). The single-electron current is given by the time propagation of an eigenstate of the disordered flake.

We first examine the effect of randomly distributed single vacancies. The influence of other short-range defects is expected to be qualitatively similar. First of all, we observe a dramatic change in the single-electron current $j_n(t)$ calculated for a flake with single vacancies [Fig.5.10(b) and red curves in Fig.5.10(c) and (d)] as compared

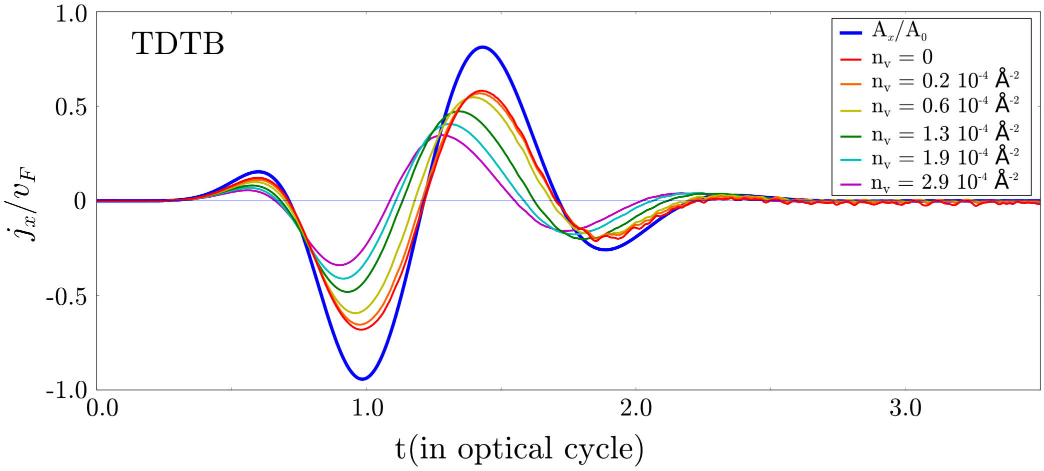

FIGURE 5.11: The time evolution of the integrated current [Eq.(5.33)] calculated within the TDTB approximation for different number of randomly distributed over the flake single vacancies.

to the disorder-free case [Fig.5.10(a) and black curves in Fig.5.10(c) and (d)] . Within each half-cycle of the pulse the current decreases, due to electron backscattering at the vacancies. The total (integrated) current [Eq.(5.33)] calculated for a pulse strength of 40 kV/cm [Fig.5.11] displays a pronounced decrease of its amplitude with increasing amount of short-range disorder due to the enhancement of electron back scattering. Furthermore, in the presence of disorder the response is out of phase with the vector potential [blue curve in Fig.5.11, the ideal current denoted in red in Fig.5.11 is perfectly in-phase with the vector potential]. The current is leading the vector potential and the phase shift increases with increasing disorder. We note that we only consider elastic disorder scattering processes with the amount of disorder resulting in shortest elastic scattering times of ≈ 100 fs. Including the energy loss in theoretical calculations [105] leads to a similar phase shift of the current.

The power spectrum [Eq.(5.32)] of the total response of the graphene flake in the presence of short-range scatterers [Fig.5.12(a)] clearly shows the SHG. The intensity of the second-order nonlinearity increases with increasing number of vacancies. In contrast, long-range disorder does not lead to the appearance of the second-order harmonic [Fig.5.12(b)]. We model long-range disorder as smooth random modulations of the on-site energies with amplitude $a = 50$ meV and correlation length l_{cor} =10 (or 25) nm in the tight-binding approximation. This potential describes charge puddles in graphene on SiO$_2$ [55]. Note that l_{cor} is much smaller than the classical quiver amplitude $x_0 = |e|A_0/m\omega = 180$ nm at $E_0 = 40$ kV/cm. Long-range disorder does not allow for K-K' (intervalley) scattering and the intravalley back scattering is very weak. Therefore, there is no second-order response as compared to short-range disorder, which induces strong intervalley back scattering of electrons. Indeed, long-range disorder does not significantly reduce single-electron

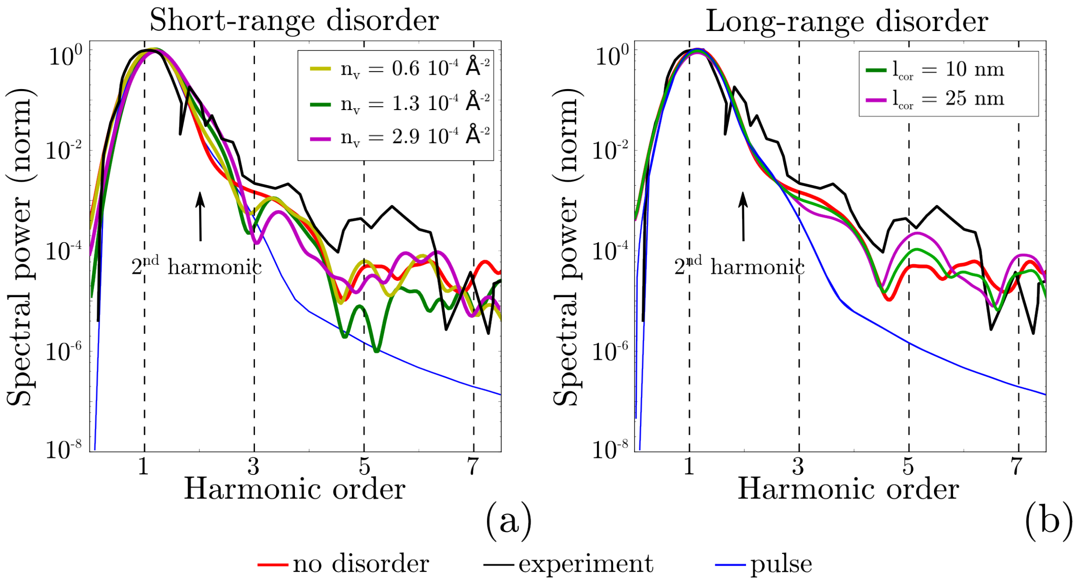

Figure 5.12: Power spectra of the far-field response calculated within the TDTB for different amount of disorder: (a) for different number of single vacancies and (b) for different correlation lengths of the smoothly varying random potential landscape. Arrows mark the second harmonic, which is only present in the case of short-range disorder.

currents generated by the eigenstates of the flake [red curves in Fig.5.10(e)] as compared to the single vacancies [red curves in Fig.5.10(c)]. Although the long-range disorder lowers the magnitude of the single-electron currents [red curves in Fig.5.10(e,f)], their contours still follow the currents of the disorder-free case [black curves in Fig.5.10(e,f)]. Notably, the interband polarizations manifesting themselves as oscillations of the current decrease [red curve in Fig.5.10(e)] in comparison with the disorder-free case [black curve in Fig.5.10(e)] presumably due to the disorder-induced dephasing of the signal, i.e. dephasing between the two electron paths moving within the conduction and valence bands [see discussion in subsection 5.2.2 and Fig.5.4].

5.5 High-harmonic generation in graphene

One important aspect of nonlinear optics is high-harmonic generation in systems interacting with strong laser pulses. This nonlinear phenomenon was first discovered in gases [22, 23]. In strong femtosecond laser fields an electron can leave the atomic core through above threshold ionization (ATI) and recombine with the core as the field reverses, emitting a single high-frequency photon [24]. The recombination and emission of photons in gases creates a train of attosecond pulses. The harmonic spectrum of such a pulse train reveal a sharp cut-off [22, 23], which scales linearly with the laser intensity or parabolic with the laser field amplitude. By contrast, recent studies of solid crystals, e.g., ZnO [25], GaSe [26], and SiO_2 [113] subject to intense laser pulses revealed high-harmonic generation with a cut-off energy scaling linearly with the laser field, i.e. with the square root of the laser intensity. This fundamental difference in the behavior of gases and solids sparked a lot of discussions [26, 113, 120–123].

Within a single-band model [25, 113, 124] the appearance of high-harmonic generation (HHG) in semiconductors was attributed to the nonlinear *intraband* response as a result of the nonparabolicity of the band. Within this model the cut-off frequency ω_c of the broadband HHG spectra is predicted to be proportional to the Bloch oscillation frequency $\Omega_B = |e|aE_0/\hbar$, i.e. the largest possible frequency in the one band model. Here a is the lattice constant and E_0 is the electric field amplitude of the laser. The same scaling behavior of ω_c was derived as a result of transitions between Wannier-Stark states separated by multiples of $\hbar\Omega_B$ in Ref. [125]. However, this model fails to predict the harmonic generation with odd frequencies of the driving field ω in the spectra observed in various experiments.

Alternative approaches to HHG in solids based on the inclusion of multiple bands [120–123] anticipate that the HHG is governed not only by the anharmonic electron motion within one conduction band but by a complex interplay between *intraband* and *interband* responses. More precisely, this interplay results in *interband* polarizations dominating the high energy part of the spectra and the harmonic cut-off. For example, in Refs. [121, 122] the cut-off is given by the maximal energy difference between the valence and conduction bands. The cut-off frequency ω_c scales as E_0/ω or equally as strength of the vector potential of the laser pulse A_0.

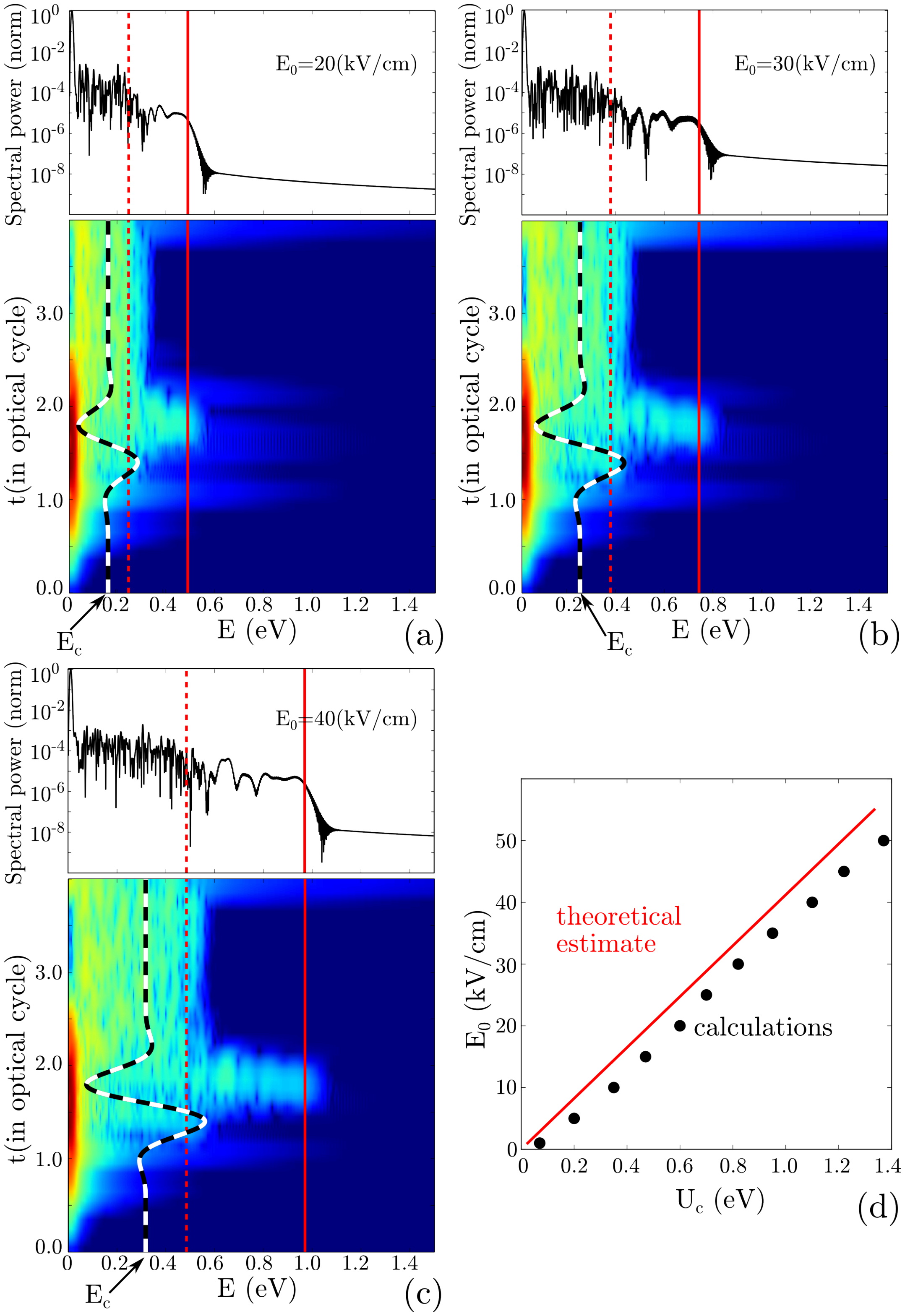

FIGURE 5.13: (a)-(c) Integrated (top) and time-resolved (bottom) power spectrum [Eq.(5.32)] of the far-field response of the graphene to a 2THz, 2-cycle Gaussian laser pulse with zero carrier envelope phase. The amplitude of the laser field: (a) $E_0 =$ 20 kV/cm, (b) $E_0 = 30$ kV/cm and (c) $E_0 = 40$ kV/cm. We use linear dispersion $E = v_F p = v_F|e|A(t)$ to plot the vector potential (black-white curve), starting from the critical energy $|E_c| = v_F|e|A_0$. Solid red lines show the theoretically estimated harmonic cut-off U_c. Dashed red lines correspond to 50 % of the U_c (d) Theoretically estimated (red line) and computed (black dots) harmonic cut-offs as function of the laser field strength.

In this section we address the question of the importance of the interband polarizations on the spectra of a qualitatively different material - the monolayer graphene. Consider first the response of graphene to a 2THz, two-cycle laser pulse with a Gaussian envelope and zero carrier envelope phase. The calculated high-harmonic spectra [see Fig.5.13(a-c)] for different laser strengths consist of three main regions: (i) a pronounced part of low frequency harmonics exponentially decaying as a function of ω; (ii) a central plateau region; and (iii) a sharp cut-off at high frequencies. Similar spectra were first observed in laser-irradiated gases [22, 23]. The generation of high frequency photons in gases is explained through recombination of the ionized electrons with their ionic cores. The kinetic energy gained by an electron propagating in the laser field determines the energy of the radiation emitted, when the electron recombines with its core. The cut-off U_c is given by the maximal kinetic energy gain after which an electron can still return back to its core and is estimated as [24]

$$U_c^{\text{atoms}} = I_p + 3.17U_p = I_p + 3.17e^2E_0^2/4m\omega^2, \tag{5.36}$$

where I_p and U_p are the ionization potential of the atom and the ponderomotive energy respectively [24, 126] defined as the average quiver energy of the oscillating electron in the laser field. It scales as the square of the vector potential A_0. The reason for the cut-off can be explained as follows. The time-evolution of the ionized electron (due to the ATI) can be approximated using classical equations of motion. To generate a photon through recombination with the ionic core, the electron needs to return back to its ion at some later time. A precise analysis of such classical trajectories reveals that the maximum classical electron kinetic energy upon the return is $3.17U_p$, determining the cut-off [24]. Notably, the cut-off is proportional to the square of the vector potential (or to the laser intensity, i.e. E_0^2). By contrast, the linear dispersion of graphene results in a cut-off energy linearly proportional to the vector potential [see black dots in Fig.5.13(d)]. The HHG cut-off U_c in graphene and in atoms depends not only on the amplitude of the laser field, but also on the laser frequency.

To gain an understanding on how the harmonic spectrum is formed and within what time frame the highest possible harmonics are generated we perform a windowed Fourier transform of the total current [see bottom figures in Fig.5.13(a-c)]. Interestingly, a time-resolved analysis of the Fourier spectrum shows the appearance of very high harmonics right after the maximum of the vector potential A_{max}. The highest harmonic develops at the subsequent minimum of the vector potential A_{min}. For the rest of the laser pulse the spectrum stays broad but confined to energies below 50 % of the cut-off energy. The appearance of high harmonics within a narrow time window and their energy cut-off can be understood as follows. Consider an electron with initial electron momentum $p_x \approx -|e|A_0$ ($p_y << p_x$) and energy $E_c \approx -v_F|e|A_0$ [Fig.5.14(a) at t_0], which coincides

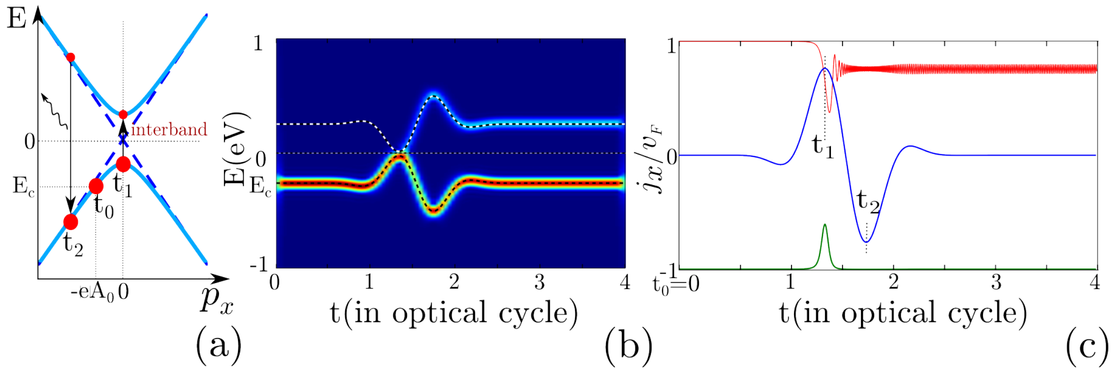

FIGURE 5.14: (a) Schematic interpretation of high energy harmonic generation in graphene and the harmonic cut-off. The depicted state contributes to the energy cut-off. At $t_0 = 0$ a state has an energy E_c and momentum $p_x \approx -|e|A_0$ (but $p_y \neq 0$). At the maximum of the vector potential (at time t_1) the state momentum is ≈ 0 and its energy reaches the minimal cross-sectional (with $p_y = \text{const}$) band gap allowing for enhanced Landau-Zener tunneling between the two bands. Two paths then propagate within conduction and valences cones. The maximal energy distance between the two trajectories at the minimum of the vector potential (at time t_3) give rise to the cut-off energy. (b) Windowed Fourier transform of a wave function $\Psi(t)$ evaluated by solving the TDDE with an initial momentum $\vec{p} = (p_x, p_y) = (-0.9, 0.1)|e|A_0$ and an energy close to E_c. (c) Time-evolution of the single-electron current (red curve) evaluated for the same wave function $\Psi(t)$ as in (b). The corresponding intraband current (for a state moving only within one band) is shown in green. We multiplied the intraband current by -1 for better visibility. Blue curve represents the vector potential of the laser.

with the maximal energy a Dirac electron can pick up from the laser field. Then, at the maximum of the vector potential this electron is brought close to the Dirac point $p_x = p_{x0} + |e|A_0 = 0$ by the laser [Fig.5.14(a) at t_1], where part of the electron wave packet can be excited to the conduction band through interband Landau-Zener tunneling [115]. Superposition of the two wave packets results in the oscillations of the single-electron current $j_x(t)$. The oscillation frequency is determined by the phase difference between the two wave packets, $\Omega(t) = (E_+(t) - E_-(t))/\hbar = 2E_+(t)/\hbar$ [106] [as discussed in subsection 5.2.1]. The maximal possible phase and, therefore, energy difference between the two (conduction and valence band) pathways is achieved at the minimum of the vector potential [Fig.5.14(a) at t_2], i.e. $\approx 2v_F|e|(A_{\text{max}} - A_{\text{min}})$, and determines the energy cut-off

$$\begin{aligned} U_c^{\text{graphene}} &= 2v_F|e|(A_{\text{max}} - A_{\text{min}}) \\ &\approx 4v_F|e|A_0 = 4v_F|e|E_0/\omega, \end{aligned} \tag{5.37}$$

being proportional to A_0. Notably, the cut-off depends not only on the field strength, but also on the driving frequency similar to U_c^{atoms} [Eq.(5.36)]. The cut-off predicted for Bloch oscillating electrons within a single cosine-like band model does not show any frequency dependence. Even if the single band model includes (small) higher order Fourier components to correctly reproduce the bandstructure [113], the frequency dependence of

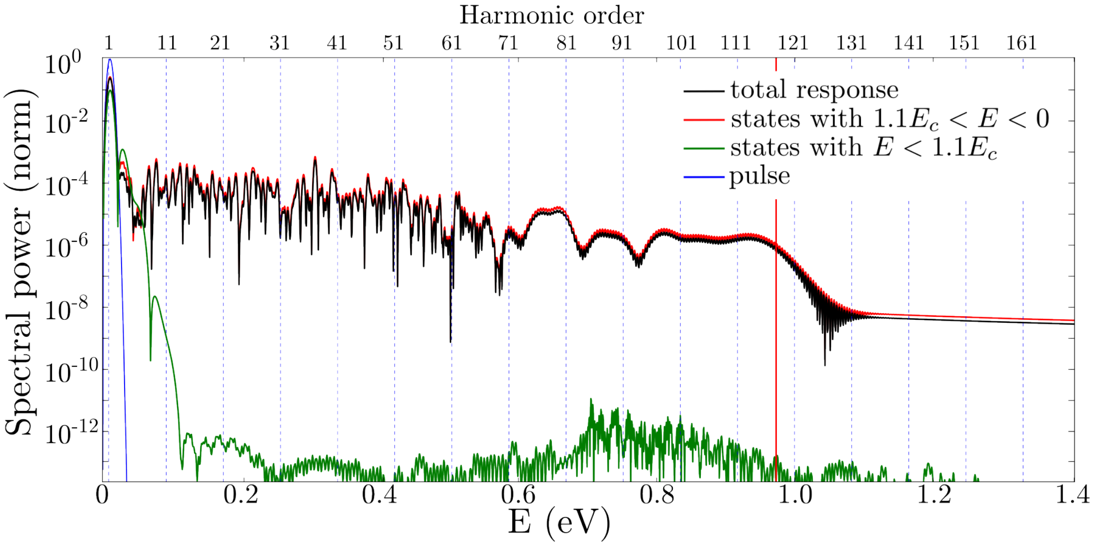

FIGURE 5.15: High-harmonic generation in graphene: the total nonlinear response of graphene is shown in black; red trace corresponds to the response of electrons near the Dirac point with energies $1.1E_c < E < 0$, these electrons contribute to the high-harmonic part of the spectra; the response of electrons away from the Dirac point with $E < 1.1E_c$ is shown in green, it reveals only rapidly decaying odd harmonics at low energies.

the cut-off energy is expected to be weak. Our theoretical estimate of U_c^{graphene} [see solid red lines in Fig.5.13(a-c) and Fig.5.13(d)] agrees well with simulations [see black dots in Fig.5.13(d)]. The small deviation between theoretical estimate and calculations can be explained by the tunneling and interband polarization for electrons with energies below $|E_c|$. The probability of such events, however, decays exponentially with increasing $|E|$.

To further support the discussion above and to provide an example of a trajectory in the energy space contributing to the harmonic cut-off, we solve the TDDE for an initial state with $\vec{p} = (0.8, 0.1)eA_0$ and $E = -0.8v_F|e|A_0$. The windowed Fourier transform of the calculated wave function $\psi(t)$ describes the energy evolution $E(t)$ of the wave packet [Fig.5.14(b)]. Apparently, the two wave packets are formed near the minimum of the vector potential at $t \gtrsim t_1$. The two wave packets gain the largest phase difference at the maximum of the laser pulse, $t \sim t_2$, as we described above. Moreover, the single-electron current [red curve in Fig.5.14(c)] evaluated by using Eq.(5.22) reveals oscillations. There is an obvious correlation between the frequency of these oscillations and the phase difference between the two wave packet propagating within the valence and conduction bands. In particular, the oscillations are present only if two wave packets are formed due to the tunneling process while passing near the Dirac point, i.e. at times $t \gtrsim t_1$ [see red curve in Fig.5.14(c)]. They are the fastest, when the phase difference between the two wave packets (or the energy difference between the two pathways $E_\xi(t)$ along which the wave packets propagate in the laser field) is maximal. The intraband current [green curve in Fig.5.14(c)] calculated for an electron moving only within the valence band does not show such oscillations. It coincides with the total current [red curve in Fig.5.14(c)] only at the beginning of the pulse, i.e. $t \lesssim t_1$, when the electron moves only within the lower band.

Electrons above the energy E_c and up to the Dirac point can tunnel between the two cones similarly producing single-electron currents resulting in a complex mixture between intraband and interband contributions. These electrons form the broad harmonic plateau as well as decaying low harmonics. Electrons with energies below E_c have an exponentially small tunneling probability between the two cones and, hence, produce only an intraband current. We confirm these statements by calculating the integrated response of electrons with $E \lesssim E_c$ [see green trace in Fig.5.15]. The harmonic spectrum shows only rapidly decaying odd harmonics due to the intraband current at low energies. Note that this current does not probe the vicinity of the sharp Dirac point and, therefore, produces an exponentially decaying response. The other features, such as the plateau and the harmonic cut-off, are absent. Electrons with energies $E_c \lesssim E \leq 0$, on the other hand, account for the most part of the high-harmonic spectrum [see Fig.5.15 red trace], and in high energies (up to the cut-off energy) their contribution coincides with the total response [see Fig.5.15 black trace].

In the time-resolved Fourier spectrum we observe another cut-off after the pulse is over [denoted by dashed red lines in Fig.5.13(a-d)]. This cut-off originates from the residual interband polarizations after the end of the pulse. The maximal oscillation frequency in the single-electron current is governed by the same types of trajectories (in energy space) that give rise to the main cut-off [Fig.5.14(b)]. After the pulse is over the wave packet in the lower band returns to its initial state with energy $-|E_c|$ and the wave packet in the upper band correspondingly returns to a state with $|E_c|$. The frequency of the oscillations of the current produced by the superposition of these two states is $\Omega = (E_+ - E_-)/\hbar = 2|E_c|/\hbar$, which results in a cut-off with 50 % of the cut-off energy U_c^{graphene}.

It is also important to note that the carrier envelope phase (CEP) of the laser pulse does not induce an additional effect to the cut-off energy [Fig.5.16(a)], but can modify the details of the high energy tail. In particular a Gaussian envelope pulse with CEP of $\pi/2$ causes a more chaotic pattern near the cut-off as compared to the pulse with zero CEP [Fig.5.13(b)]. Longer pulses, for example, a Gaussian 10-cycle envelope pulse with zero CEP [Fig.5.16(b)], also do not introduce any change in the scaling of the cut-off and its estimate [Eq.(5.37)], but modify the harmonic spectra in the high-harmonic tail in a similar way as for a short pulse with CEP of $\pi/2$. In both cases the change in behavior near the cut-off can be assigned to the intercycle processes, i.e. the generation of high energy trajectories within the different laser cycles. Since for the short laser pulses with zero CEP the high energy trajectories contributing to the high energy part of the spectra are generated only within one laser cycle, the high energy tail of the spectra is smooth. Furthermore, we stress that U_c^{graphene} is proportional to the Fermi velocity, which may allow for an independent way to extract v_F in the experiment, i.e. by analyzing the high-harmonic cut-off. For example, the Fermi velocity of graphene in our tight-binding approximation is $v_F^0 = 0.78 \cdot 10^6$ m/s. The HHG spectra for graphene evaluated within the TDDE with changed value of Fermi velocity from $v_F^D = 10^6$ m/s to v_F^0 [Fig.5.16(c)] and the HHG calculated within the TDTB approach [Fig.5.16(d)] feature a cut-off shifted to lower energies in accord with our estimate of U_c^{graphene} [Eq.(5.37)]. Notably, these harmonic spectra calculated within the TDDE and the TDTB [Fig.5.16(c) and (d)] show overall comparable behavior. The differences in the two signals arise from the different approximate treatment of the graphene bandstructure in these two approaches.

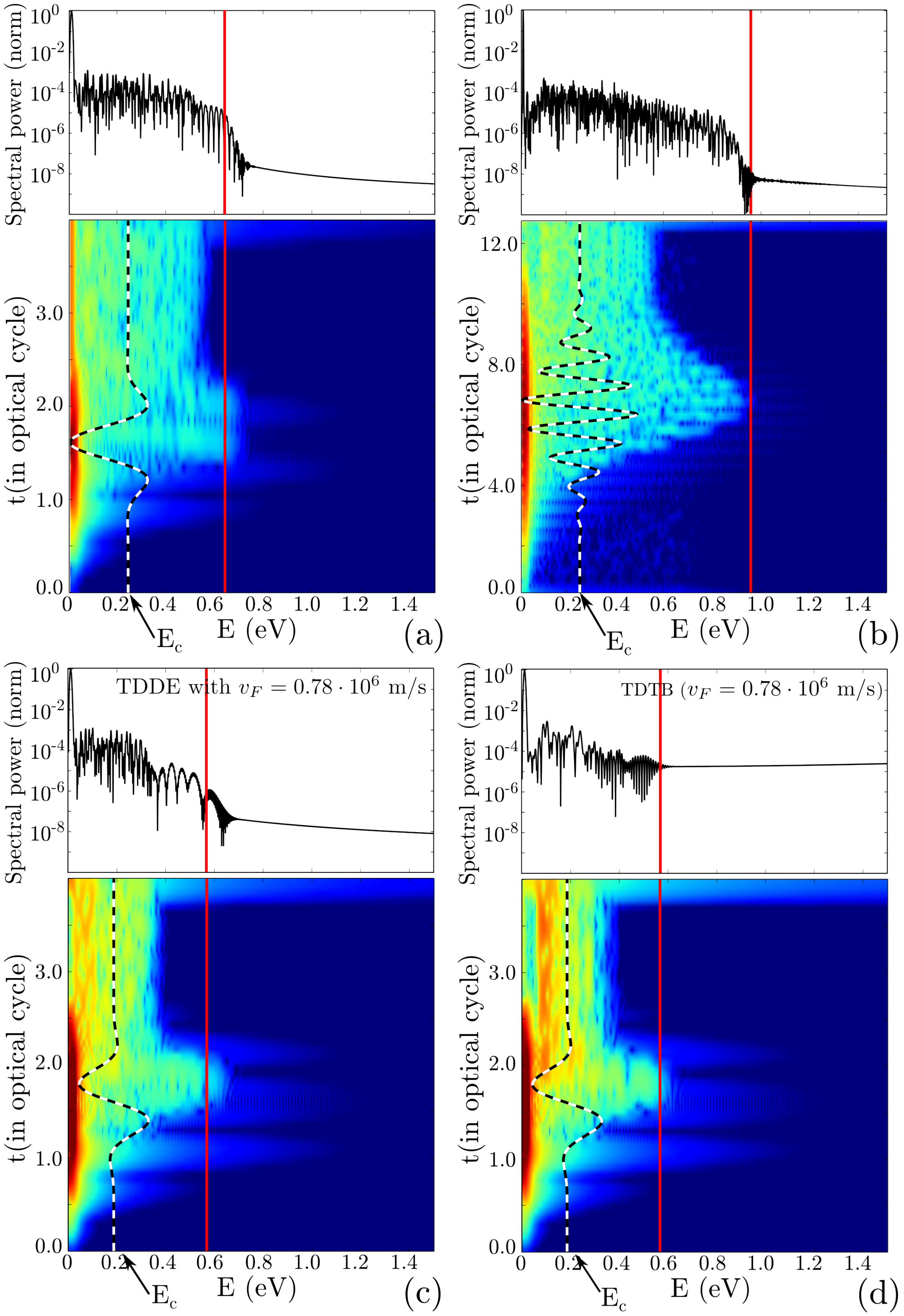

FIGURE 5.16: Same as in Fig.5.13. High armonic spectra of graphene subject (a) to a 2-cycle Gaussian 2THz laser pulse with carrier envelope phase (CEP) of $\pi/2$; (b) to a 10-cycle Gaussian 2THz laser pulse (CEP=0). (c-d) to a 2-cycle Gaussian 2THz laser pulse (CEP=0). In all figures the pulse strength is 30 kV/cm. Response in (c) is calculated within the TDDE, however, with a reduced value of Fermi velocity $v_F^0 = 0.78 \cdot 10^6$ m/s equal to the Fermi velocity of graphene in our tight-binding approximation. (d) The high-harmonic spectra of graphene within the TDTB. In (c-d) the cut-off energy is shifted as compared to Fig.5.13(b) calculated within TDDE with $v_F^D = 10^6$ m/s due to a smaller value of the Fermi velocity v_F^0.
]

Chapter 6

Summary

In this thesis we touched only a few problems of graphene science. Our research was mainly motivated by the following recent experiments: (i) measurements of electrical conductivity in graphene nanoconstrictions [27]; (ii) measurements of electronic and optical properties of graphene on hexagonal boron nitride [15, 18]; and (iii) the measured nonlinear optical response of multi-layer graphene [21]. These experiments inspired us to attempt a detailed theoretical description which is based on the Dirac and the third-nearest-neighbor tight-binding approximations. Both methods have advantages and disadvantages. A solution of the Dirac equation provides insight on the properties of bulk graphene, but in this approach the bandstructure of graphene is oversimplified, for example, trigonal warping and electron-hole asymmetry are neglected. These issues can be resolved in the tight-binding approximation. Considering contributions from up to the third-nearest-neighbor carbon atoms leads to recovering of proper particle-hole asymmetry in the bandstructure and of trigonal warping. By constructing the tight-binding Hamiltonian on a grid, one can introduce disorder and describe complex nanostructures.

In chapter 3 we applied the tight-binding approximation to study the electronic transport properties of graphene nanoconstrictions resembling quantum point contacts (QPC). The shape of the nanodevice we studied was taken directly from an AFM image of the device used in the experiment [27]. The measured conductance through the QPC showed distinct features whose connection to size quantization were confirmed by the magnetic field evolution. Our theoretical calculations demonstrate very good agreement with the measurements away from the Dirac point. The observed deviations from the theoretically predicted behavior of the conductance near the charge neutrality (or Dirac) point, brought us to the conclusion that localized edge states must have a significant impact on the measured signal. Indeed, the calculated density of states of such QPCs demonstrate a large deviation from the linear density of states of ideal graphene near the Dirac point due to the rough edges introduced in the calculations. This change in the density of states, of course, alters the correspondence between the back gate voltage and the Fermi energy level. Taking into account the density of localized states allowed us to achieve an excellent agreement between the measured and calculated conductance traces. We, therefore, propose that the conductance of small graphene nanodevices can be a tool for probing the physics at the device edges, by extracting the density of localized or trapped edge states from conductance trace measurements.

The graphene QPCs used in this particular experiment were sandwiched between hexagonal boron nitride films. Nowadays, hBN is commonly used as a substrate for graphene. Compared to more conventional substrates such as SiO_2 which were popular at the beginning of graphene science, atomically flat hBN induces less disorder, i.e. charge puddles and surface corrugation. Therefore, devices placed on a hBN substrate have higher mobility and allow one to observe ballistic electron transport. However, hBN can strongly modify the electronic properties of graphene if the layers are (almost) perfectly aligned. In this case the hBN induces a moiré pattern (with up to 14 nm periodicity), which changes the bandstructure of graphene by backfolding the graphene Brillouin zone into the smaller Brillouin zone of the moiré superlattice. Van der Waals interaction between graphene and hBN opens up a gap at the Dirac point and small mini-gaps, where the bands cross. In chapter 4 we studied the influence of such superlattice on the bandstructure of bulk graphene. Using the tight-binding approximation we calculated the density of states of large-scale graphene flakes in a magnetic field and found excellent agreement with magneto-capacitance experiments. In particular, we observed the formation of Hofstadter butterflies on top of each Landau level of Dirac fermions and new Landau levels emerging above and below the Dirac point, corresponding to mini-gaps (or avoided crossings) in the bandstructure. Moreover, our analysis showed that the correspondence between the back gate voltage and the Fermi energy in graphene depends on the density of states in a similar way as we observed for the transport problem [chapter 3]. To resolve any artifact related to measurements of the density of states as function of back gate voltage, we presented an alternative probe of the DOS in the magnetic field by using magneto-optical spectroscopy. In this method, the measured optical conductivity provides information on optical inter-Landau levels transitions as function of the photon energy. The theoretically calculated optical conductivity has many features which we could trace back to the DOS. We also included effects related to the formation of magneto-excitons, i.e. electron-hole pairs created due to optical excitations between the Landau levels. We estimated the exciton binding energy in terms of the direct two-particle Coulomb interaction, approximating the excitonic wave function as a product of two eigenstates of a graphene flake near the optically excited Landau levels. Even though we evaluated the direct Coulomb interaction to first order only, our approach yields quantitative agreement to the experimentally observed shift of the inter-Landau levels transition lines [15].

After studying the optical response of graphene in the near- and mid-infrared spectral range we moved to the far-infrared region and studied the nonlinear response of graphene to THz radiation [chapter 5]. The linear dispersion of electrons in graphene is a promising prerequisite for the observation of nonlinear effects such as high-order harmonics generation. We confirmed the existence of high-order nonlinearities by solving the Dirac and the Schrödinger equations (with a tight-binding Hamiltonian) in the time domain. The results of our calculations agree well with a recent experiment where the third and fifth harmonics were observed in multilayer epitaxial graphene [21]: the relative harmonic strengths are consistent with the experiment in both Dirac and tight-binding models. We demonstrated that the second-order harmonic appear only after introducing defects, which locally break the inversion symmetry of graphene. Moreover, we investigated the influence of interband polarization on the high-harmonic cut-off, which scales linearly with the laser field. We found a close correspondence with other experiments and theories studying the high harmonic generation in semiconductors and insulators.

As outlook we note that in chapter 3 and 4, we dealt with graphene on hBN or graphene sandwiched between hBN. Going forward, new devices with several layers of alternating graphene and hBN or other 2D materials can be fabricated [127–129]. Such layered materials are called van der Waals heterostructures and are expected to become a new area of material science. The graphene - hBN heterostructures could be interesting for studying nonlinear response of graphene. Single layer graphene absorbing only 2.3% of light [20] generates a very weak response signal which is difficult to detect. Therefore, to enhance the response a multi-layer graphene was used in the optical experiments aiming to detect a nonlinear response. However, the interaction between layers cannot be neglected and the signal might deviate from expectations in the high-energy part of the nonlinear spectra. An additional hBN layer between graphene layers could prevent such interlayer interactions. The further study of moiré phenomena could be another interesting subject in application to transport and nonlinear optical response. The moiré superlattice changing the bandstructure of graphene leads to substantial changes in magneto-transport properties [19, 130] due to the presence of mini-gaps and Hofstadter butterfly. The presence of minigaps can alter the nonlinear optical response of graphene. In particular, the mini-gaps could modify the cut-off energy and perhaps enhance the interband polarizations. We believe these questions will be addressed in works to follow.

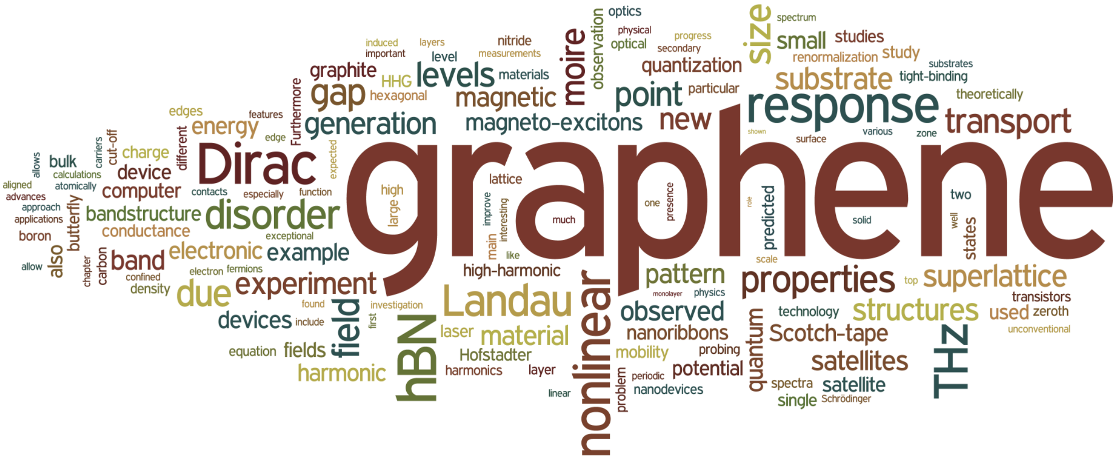
graphene
response
Dirac
disorder
transport
size
substrate
point
new
magnetic
levels
generation
gap
graphite
magneto-excitons
quantization
moire
observation
optics
physical
optical
progress
secondary
spectrum
small
studies
renormalization
study
substrates
tight-binding
theoretically
particular
nitride
measurements
materials
induced
important
layers
level
HHG
hexagonal
edges
features
energy
edge
Furthermore
expected
different
charge
cut-off
carriers
bulk
allows
calculations
device
atomically
aligned
computer
advances
approach
applications
boron
contacts
especially
function
bandstructure
conductance
butterfly
also
allow
band
chapter
carbon
confined
density
electronic
exceptional
example
electron
fermions
due
experiment
found
include
devices
investigation
first
field
equation
fields
harmonic
hBN
high
large
improve
interesting
main
like
lattice
much
one
presence
role
predicted
high-harmonic
Landau
laser
material
Hofstadter
harmonics
layer
linear
nonlinear
problem
periodic
pattern
monolayer
physics
observed
nanoribbons
mobility
probing
potential
nanodevices
quantum
spectra
single
satellite
Schrödinger
satellites
Scotch-tape
technology
structures
THz
properties
top
superlattice
transistors
used
zeroth
unconventional
scale
shown
surface
various
zone
solid
two
well
states

FIGURE 6.1: Thesis summary

As final accord, we summarized the whole thesis in a diagram in Fig.6.1, which was created by counting the words most frequently used throughout the thesis.

Appendix

Appendix A

Windowed Fourier transform

The windowed Fourier transform is a tool to obtain information about a signal simultaneously in the time and frequency domains (for more details see [131]). The Fourier transform of a signal function $f(t)$ in the time-frequency domains is defined as:

$$f(\omega, t) = \int_{-\infty}^{\infty} dt' e^{-2\pi i\omega t'} g(t' - t) f(t'), \tag{A.1}$$

where $g(t)$ is a window (or weight) function helping to resolve the signal with time. It is defined within a time window T, which defines the time-resolution of the Fourier transform of the signal. Outside this window $g(t)$ vanishes. We use a $g(t)$ of the form:

$$g(t) = \begin{cases} 1 + \cos\left(\frac{2\pi t}{T}\right) & |x| \leq T/2 \\ 0 & \text{otherwise.} \end{cases} \tag{A.2}$$

In the main text of the thesis, we performed the windowed Fourier transform using the window function $g(t)$ defined above with the parameter T chosen to achieve reasonable time-frequency resolution.

Appendix B

Short Iterative Lanczos propagator

To perform numerical time propagation of a wave function, i.e. to find $e^{-iHt/\hbar}\Psi$, we use the Short Iterative Lanczos propagator. In this section we highlight the concept of the method (for more details, see Ref.[132]). This polynomial method, performs the propagation within a Krylov subspace. The N-dimensional Krylov subspace is spanned by the vectors $q_j = H^j\Psi(0)$. In the Lanzos method each new Krylov vector is constructed to be orthogonal to all previous ones. The first vector q_0 is just an initial state $\Psi(0)$. To determine the second vector, we multiply q_0 by the hamiltonian matrix H and do the necessary orthogonalization

$$Hq_0 = \alpha_0 q_0 + \beta_0 q_1, \tag{B.1}$$

by introducing $\alpha_0 = \langle q_0|H|q_0\rangle$ and $\beta_0 = \langle q_1|H|q_0\rangle$. One can show that the general expression for finding vector q_{j+1} in the Krylov subspace is

$$Hq_j = \beta_{j-1}q_{j-1} + \alpha_j q_j + \beta_j q_{j+1}, \tag{B.2}$$

with $\alpha_j = \langle q_j|H|q_j\rangle$ and $\beta_j = \langle q_{j+1}|H|q_j\rangle$. The coefficients α_j and β_j are the elements of the tridiagonal matrix H_N in the Lanczos basis, i.e. satisfy the equation $Hq_j = \sum_i H_N^{ij} q_i$. The propagator in the N-dimensional Lanczos-Krylov subspace over the time step Δt is

$$U(\Delta t) = e^{-iH_N\Delta t/\hbar}. \tag{B.3}$$

By diagonalizing the matrix H_N, we can find its eigenvalues and eigenfunctions. If D_N is a diagonal matrix of eigenvalues of H_N and O is a matrix holding the corresponsing eigenfunctions, i.e. $H_N = OD_N O^\dagger$, we can rewrite the evolution operator as

$$U(\Delta t) = Oe^{-iD_N \Delta t/\hbar} O^\dagger. \tag{B.4}$$

The evolution of the wave function in the Lanczos basis over a time step Δt is

$$|\psi(\Delta t)\rangle = Oe^{-iD_N \Delta t/\hbar} O^\dagger |\psi(0)\rangle, \tag{B.5}$$

where $\psi(0)$ is an N dimensional vector with elements $(1, 0, 0, \ldots, 0)^T$. The real space wave function we have to project $|\psi(\Delta t)\rangle$ onto the Krylov basis vectors as

$$\Psi(\vec{r}, \Delta t) = \sum_{i=0}^{N} \psi_i \langle \psi_i(\Delta t) | q_i \rangle. \tag{B.6}$$

The numerical error can be estimated, by evaluating

$$N_{\text{Error}} = \left| \frac{\partial}{\partial t}\Psi - \frac{H}{i\hbar}\Psi(0) \right| = \left| \frac{\Psi(\Delta t) - \Psi(0)}{\Delta t} - \frac{H}{i\hbar}\Psi(0) \right|. \tag{B.7}$$

The method is very efficient, as the size of the Krylov subspace N is usually small and is governed by the numerical error N_{Error}. Therefore, diagonalization of the matrix H_N is fast. For further optimization this method can be used with an adaptive step size. To determine the time step Δt or size of the Krylov subspace N in a particular problem, one evaluates the numerical error N_{Error}. If N_{Error} becomes larger than desired error, one increases N or decreases Δt. Another advantage of the method is the possibility to consider time-dependent Hamiltonians, i.e. we can change our hamiltonian matrix after each propagation step. This is important for treating, for example, electronic propagation due to the presence of a time-dependent laser pulse.

Bibliography

[1] H. W. Kroto, J. R. Heath, S. C. O'Brien, R. F. Curl, and R. E. Smalley, "C60: Buckminsterfullerene," *Nature*, vol. 318, no. 6042, pp. 162–163, 1985.

[2] S. Iijima, "Helical microtubules of graphitic carbon," *Nature*, vol. 354, no. 6348, pp. 56–58, 1991.

[3] M. Monthioux and V. L. Kuznetsov, "Who should be given the credit for the discovery of carbon nanotubes?," *Carbon*, vol. 44, no. 9, pp. 1621–1623, 2006.

[4] A. K. Geim, "Nobel lecture: Random walk to graphene," *Rev. Mod. Phys.*, vol. 83, pp. 851–862, Aug 2011.

[5] K. S. Novoselov, A. K. Geim, S. V. Morozov, D. Jiang, Y. Zhang, S. V. Dubonos, I. V. Grigorieva, and A. A. Firsov, "Electric Field Effect in Atomically Thin Carbon Films," *Science*, vol. 306, pp. 666–669, Oct. 2004.

[6] K. S. Novoselov, A. K. Geim, S. V. Morozov, D. Jiang, M. I. Katsnelson, I. V. Grigorieva, S. V. Dubonos, and A. A. Firsov, "Two-dimensional gas of massless Dirac fermions in graphene," *Nature*, vol. 438, pp. 197–200, Nov. 2005.

[7] N. Tombros, A. Veligura, J. Junesch, J. J. van den Berg, P. J. Zomer, M. Wojtaszek, I. J. Vera Marun, H. T. Jonkman, and B. J. van Wees, "Large yield production of high mobility freely suspended graphene electronic devices on a polydimethylglutarimide based organic polymer," *Journal of Applied Physics*, vol. 109, pp. 093702+, May 2011.

[8] L. Banszerus, M. Schmitz, S. Engels, J. Dauber, M. Oellers, F. Haupt, K. Watanabe, T. Taniguchi, B. Beschoten, and C. Stampfer, "Ultrahigh-mobility graphene devices from chemical vapor deposition on reusable copper," *Science Advances*, vol. 1, no. 6, p. e1500222, 2015.

[9] L. Vicarelli, M. S. Vitiello, D. Coquillat, A. Lombardo, A. C. Ferrari, W. Knap, M. Polini, V. Pellegrini, and A. Tredicucci, "Graphene field-effect transistors as room-temperature terahertz detectors," *Nature Materials*, vol. 11, pp. 865–871, Oct. 2012.

[10] L. Prechtel, L. Song, D. Schuh, P. Ajayan, W. Wegscheider, and A. W. Holleitner, "Time-resolved ultrafast photocurrents and terahertz generation in freely suspended graphene," *Nature Communications*, vol. 3, p. 646, 2012.

[11] C. Sirtori, "Applied physics: Bridge for the terahertz gap," *Nature*, vol. 417, pp. 132–133, May 2002.

[12] L. A. Ponomarenko, F. Schedin, M. I. Katsnelson, R. Yang, E. W. Hill, K. S. Novoselov, and A. K. Geim, "Chaotic Dirac Billiard in Graphene Quantum Dots," *Science*, vol. 320, pp. 356–358, Apr. 2008.

[13] J. Xue, J. Sanchez-Yamagishi, D. Bulmash, P. Jacquod, A. Deshpande, K. Watanabe, T. Taniguchi, P. Jarillo-Herrero, and B. J. LeRoy, "Scanning tunnelling microscopy and spectroscopy of ultra-flat graphene on hexagonal boron nitride," *Nature Materials*, vol. 10, pp. 282–285, Feb. 2011.

[14] R. Decker, Y. Wang, V. W. Brar, W. Regan, H.-Z. Tsai, Q. Wu, W. Gannett, A. Zettl, and M. F. Crommie, “Local Electronic Properties of Graphene on a BN Substrate via Scanning Tunneling Microscopy,” *Nano Lett.*, vol. 11, pp. 2291–2295, May 2011.

[15] Z.-G. Chen, Z. Shi, W. Yang, X. Lu, Y. Lai, H. Yan, F. Wang, G. Zhang, and Z. Li, “Observation of an intrinsic bandgap and Landau level renormalization in graphene/boron-nitride heterostructures,” *Nature Communications*, vol. 5, July 2014.

[16] M. Yankowitz, J. Xue, D. Cormode, J. D. Sanchez-Yamagishi, K. Watanabe, T. Taniguchi, P. Jarillo-Herrero, P. Jacquod, and B. J. LeRoy, “Emergence of superlattice Dirac points in graphene on hexagonal boron nitride,” *Nature Physics*, vol. 8, pp. 382–386, Mar. 2012.

[17] C. R. Dean, L. Wang, P. Maher, C. Forsythe, F. Ghahari, Y. Gao, J. Katoch, M. Ishigami, P. Moon, M. Koshino, T. Taniguchi, K. Watanabe, K. L. Shepard, J. Hone, and P. Kim, “Hofstadter’s butterfly and the fractal quantum Hall effect in moiré superlattices,” *Nature*, vol. 497, pp. 598–602, May 2013.

[18] G. L. Yu, R. V. Gorbachev, J. S. Tu, A. V. Kretinin, Y. Cao, R. Jalil, F. Withers, L. A. Ponomarenko, B. A. Piot, M. Potemski, D. C. Elias, X. Chen, K. Watanabe, T. Taniguchi, I. V. Grigorieva, K. S. Novoselov, V. I. Fal’ko, A. K. Geim, and A. Mishchenko, “Hierarchy of Hofstadter states and replica quantum Hall ferromagnetism in graphene superlattices,” *Nature Physics*, vol. 10, pp. 525–529, June 2014.

[19] B. Hunt, J. D. Sanchez-Yamagishi, A. F. Young, M. Yankowitz, B. J. LeRoy, K. Watanabe, T. Taniguchi, P. Moon, M. Koshino, P. Jarillo-Herrero, and R. C. Ashoori, “Massive Dirac Fermions and Hofstadter Butterfly in a van der Waals Heterostructure,” *Science*, vol. 340, pp. 1427–1430, June 2013.

[20] K. F. Mak, M. Y. Sfeir, Y. Wu, C. H. Lui, J. A. Misewich, and T. F. Heinz, “Measurement of the optical conductivity of graphene,” *Phys. Rev. Lett.*, vol. 101, p. 196405, Nov 2008.

[21] P. Bowlan, E. Martinez-Moreno, K. Reimann, T. Elsaesser, and M. Woerner, “Ultrafast terahertz response of multilayer graphene in the nonperturbative regime,” *Physical Review B*, vol. 89, 2014.

[22] A. McPherson, G. Gibson, H. Jara, U. Johann, T. S. Luk, I. A. McIntyre, K. Boyer, and C. K. Rhodes, “Studies of multiphoton production of vacuum-ultraviolet radiation in the rare gases,” *Journal of the Optical Society of America B*, vol. 4, no. 4, pp. 595–601, 1987.

[23] M. Ferray, A. L’Huillier, X. F. Li, L. A. Lompre, G. Mainfray, and C. Manus, “Multiple-harmonic conversion of 1064 nm radiation in rare gases,” *Journal of Physics B: Atomic, Molecular and Optical Physics*, vol. 21, no. 3, pp. L31–L35, 1988.

[24] P. B. Corkum, “Plasma perspective on strong field multiphoton ionization,” *Phys. Rev. Lett.*, vol. 71, pp. 1994–1997, Sep 1993.

[25] S. Ghimire, A. D. DiChiara, E. Sistrunk, P. Agostini, L. F. DiMauro, and D. A. Reis, “Observation of high-order harmonic generation in a bulk crystal,” *Nature Physics*, vol. 7, no. 2, pp. 138–141, 2011.

[26] O. Schubert, M. Hohenleutner, F. Langer, B. Urbanek, C. Lange, U. Huttner, D. Golde, T. Meier, M. Kira, S. W. Koch, and R. Huber, “Sub-cycle control of terahertz high-harmonic generation by dynamical Bloch oscillations,” *Nature Photonics*, vol. 8, pp. 119–123, Jan. 2014.

[27] B. Terres, L. Chizhova, F. Libisch, D. Jörger, S. Engels, A. Girschik, K. Watanabe, T. Taniguchi, S. Rotkin, J. Burgdörfer, and C. Stampfer, “Size quantization of dirac

fermions in graphene quantum point contacts," *submitted to Nature Communications*, 2015.

[28] Z. Jiang, E. Henriksen, L. Tung, Y.-J. Wang, M. Schwartz, M. Han, P. Kim, and H. Stormer, "Infrared spectroscopy of landau levels of graphene," *Phys. Rev. Lett.*, vol. 98, p. 197403, May 2007.

[29] D. C. Elias, R. V. Gorbachev, A. S. Mayorov, S. V. Morozov, A. A. Zhukov, P. Blake, L. A. Ponomarenko, I. V. Grigorieva, K. S. Novoselov, F. Guinea, and A. K. Geim, "Dirac cones reshaped by interaction effects in suspended graphene," *Nature Physics*, vol. 7, pp. 701–704, July 2011.

[30] C. Neto, F. Guinea, N. Peres, K. Novoselov, and A. Geim, "The electronic properties of graphene," *Reviews of Modern Physics*, vol. 81, no. 1, p. 109, 2009.

[31] S. D. Sarma, S. Adam, E. H. Hwang, and E. Rossi, "Electronic transport in two-dimensional graphene," *REVIEWS OF MODERN PHYSICS*, vol. 83, pp. 407+, 2011.

[32] M. Katsnelson, K. Novoselov, and A. Geim, "Chiral tunnelling and the Klein paradox in graphene," *Nature Physics*, vol. 2, pp. 620–625, 2006.

[33] P. R. Wallace, "The band theory of graphite," *Phys. Rev.*, vol. 71, pp. 622–634, May 1947.

[34] F. LIbisch, *Electronic structure and transport in mesoscopic devices.* doctor thesis, Vienna University of Technology, 2009.

[35] M. Sprinkle, D. Siegel, Y. Hu, J. Hicks, A. Tejeda, A. Taleb-Ibrahimi, P. Le Fèvre, F. Bertran, S. Vizzini, H. Enriquez, S. Chiang, P. Soukiassian, C. Berger, W. A. de Heer, A. Lanzara, and E. H. Conrad, "First Direct Observation of a Nearly Ideal Graphene Band Structure," *Physical Review Letters*, vol. 103, pp. 226803+, Nov. 2009.

[36] Y. Zhang, Y.-W. Tan, H. L. Stormer, and P. Kim, "Experimental observation of the quantum Hall effect and Berry's phase in graphene," *Nature*, vol. 438, pp. 201–204, Nov. 2005.

[37] D. L. Miller, K. D. Kubista, G. M. Rutter, M. Ruan, W. A. de Heer, P. N. First, and J. A. Stroscio, "Observing the Quantization of Zero Mass Carriers in Graphene," *Science*, vol. 324, pp. 924–927, May 2009.

[38] R. Deacon, K. C. Chuang, R. Nicholas, K. Novoselov, and A. Geim, "Cyclotron resonance study of the electron and hole velocity in graphene monolayers," *Physical Review B*, vol. 76, pp. 081406+, Aug. 2007.

[39] R. Gillen and J. Robertson, "Density functional theory screened-exchange approach for investigating electronical properties of graphene-related materials," *Physical Review B*, vol. 82, no. 12, 2010.

[40] J. Cai, P. Ruffieux, R. Jaafar, M. Bieri, T. Braun, S. Blankenburg, M. Muoth, A. P. Seitsonen, M. Saleh, X. Feng, K. Müllen, and R. Fasel, "Atomically precise bottom-up fabrication of graphene nanoribbons," *Nature*, vol. 466, pp. 470–473, July 2010.

[41] D. V. Kosynkin, A. L. Higginbotham, A. Sinitskii, J. R. Lomeda, A. Dimiev, B. K. Price, and J. M. Tour, "Longitudinal unzipping of carbon nanotubes to form graphene nanoribbons," *Nature*, vol. 458, no. 7240, pp. 872–876, 2009.

[42] M. Y. Han, B. Özyilmaz, Y. Zhang, and P. Kim, "Energy Band-Gap Engineering of Graphene Nanoribbons," *Physical Review Letters*, vol. 98, pp. 206805+, 2007.

[43] Y.-W. Son, M. L. Cohen, and S. G. Louie, "Energy gaps in graphene nanoribbons," *Phys. Rev. Lett.*, vol. 97, p. 216803, 2006.

[44] G. Z. Magda, X. Jin, I. Hagymási, P. Vancsó, Z. Osváth, P. Nemes-Incze, C. Hwang, L. P. Biró, and L. Tapasztó, "Room-temperature magnetic order on zigzag edges of narrow

graphene nanoribbons," *Nature*, vol. 514, no. 7524, pp. 608–611, 2014.

[45] L. Landau and E. Lifshitz, *Quantim Mechanics. Non-relativistic theory*, vol. 3. Pergamon Press, London, 2nd edition, 1965.

[46] I. Rabi, "Das freie elektron im homogenen magnetfeld nach der diracschen theorie," *Zeitschrift f. Physik A*, vol. 49, pp. 507+, 1928.

[47] G. Li and E. Y. Andrei, "Observation of Landau levels of Dirac fermions in graphite," *Nature Physics*, vol. 3, no. 9, pp. 623–627, 2007.

[48] A. Iyengar, J. Wang, H. Fertig, and L. Brey, "Excitations from filled landau levels in graphene," *Phys. Rev. B*, vol. 75, p. 125430, Mar 2007.

[49] R. Peierls, "Zur theorie des diamagnetismus von leitungselektronen," *Zeitschrift f. Physik*, vol. 80, p. 763, 1933.

[50] D. Ferry and S. Goodnick, *Transport in nanostructures.* Cambridge University Press, Cambridge, 1997.

[51] S. Datta, *Electronic transport in mesoscopic systems.* Cambridge University Press, Cambridge, 1995.

[52] S. Datta, *Quantum Transport: Atom to Transistor.* Cambridge University Press, Cambridge, 2005.

[53] D. S. Fisher and P. A. Lee, "Relation between conductivity and transmission matrix," *Phys. Rev. B*, vol. 23, pp. 6851–6854, Jun 1981.

[54] F. Banhart, J. Kotakoski, and A. Krasheninnikov, "Structural defects in graphene," *ACS Nano*, vol. 5, no. 1, pp. 26–41, 2011.

[55] J. Martin, N. Akerman, G. Ulbricht, T. Lohmann, J. H. Smet, K. von Klitzing, and A. Yacoby, "Observation of electronhole puddles in graphene using a scanning single-electron transistor," *Nature Physics*, vol. 4, pp. 144–148, Nov. 2007.

[56] K. Suenaga and M. Koshino, "Atom-by-atom spectroscopy at graphene edge," *Nature*, vol. 468, no. 7327, pp. 1088–1090, 2010.

[57] C. Stampfer, E. Schurtenberger, F. Molitor, J. Güttinger, T. Ihn, and K. Ensslin, "Tunable Graphene Single Electron Transistor," *Nano Lett.*, vol. 8, pp. 2378–2383, July 2008.

[58] W. Jones and N. March, *Theoretical solid state physics: Perfect lattices in Equilibrium*, vol. 1. Dover Publications, Inc., New Yourk, 2nd edition, 1987.

[59] V. Geringer, M. Liebmann, T. Echtermeyer, S. Runte, M. Schmidt, R. Rückamp, M. C. Lemme, and M. Morgenstern, "Intrinsic and extrinsic corrugation of monolayer graphene deposited on SiO2," *Physical Review Letters*, vol. 102, pp. 076102+, Feb. 2009.

[60] J. Baringhaus, M. Ruan, F. Edler, A. Tejeda, M. Sicot, A. Taleb-Ibrahimi, A.-P. Li, Z. Jiang, E. H. Conrad, C. Berger, C. Tegenkamp, and W. A. de Heer, "Exceptional ballistic transport in epitaxial graphene nanoribbons," *Nature*, vol. 506, pp. 349–354, Feb. 2014.

[61] N. Tombros, A. Veligura, J. Junesch, M. H. D. Guimarães, I. J. Vera-Marun, H. T. Jonkman, and B. J. van Wees, "Quantized conductance of a suspended graphene nanoconstriction," *Nature Physics*, vol. 7, no. 9, pp. 697–700, 2011.

[62] B. J. van Wees, H. van Houten, C. W. J. Beenakker, J. G. Williamson, L. P. Kouwenhoven, D. van der Marel, and C. T. Foxon, "Quantized conductance of point contacts in a two-dimensional electron gas," *Phys. Rev. Lett.*, vol. 60, pp. 848–850, Feb 1988.

[63] S. Engels, A. Epping, C. Volk, S. Korte, B. Voigtländer, K. Watanabe, T. Taniguchi, S. Trellenkamp, and C. Stampfer, "Etched graphene quantum dots on hexagonal boron nitride," *Applied Physics Letters*, vol. 103, no. 7, pp. 073113+, 2013.

[64] D. Bischoff, F. Libisch, J. Burgdörfer, T. Ihn, and K. Ensslin, “Characterizing wave functions in graphene nanodevices: Electronic transport through ultrashort graphene constrictions on a boron nitride substrate,” *Phys. Rev. B*, vol. 90, p. 115405, Sep 2014.

[65] Y.-M. Lin, V. Perebeinos, Z. Chen, and P. Avouris, “Electrical observation of subband formation in graphene nanoribbons,” *Phys. Rev. B*, vol. 78, p. 161409, Oct 2008.

[66] T. O. Wehling, S. Yuan, A. I. Lichtenstein, A. K. Geim, and M. I. Katsnelson, “Resonant scattering by realistic impurities in graphene,” *Phys. Rev. Lett.*, vol. 105, p. 056802, Jul 2010.

[67] J. Wurm, M. Wimmer, and K. Richter, “Symmetries and the conductance of graphene nanoribbons with long-range disorder,” *Phys. Rev. B*, vol. 85, p. 245418, Jun 2012.

[68] K. Wakabayashi, Y. Takane, M. Yamamoto, and M. Sigrist, “Edge effect on electronic transport properties of graphene nanoribbons and presence of perfectly conducting channel,” *Carbon*, vol. 47, pp. 124–137, Jan. 2009.

[69] E. N. Voloshina, E. Fertitta, A. Garhofer, F. Mittendorfer, M. Fonin, A. Thissen, and Y. Dedkov, “Electronic structure and imaging contrast of graphene moiré on metals,” *Scientific Reports*, vol. 3, Jan. 2013.

[70] D. Subramaniam, F. Libisch, Y. Li, C. Pauly, V. Geringer, R. Reiter, T. Machoff, M. Liebmann, J. Burgdörfer, C. Busse, T. Michely, T. Mazzarello, M. Pratzer, and M. Morgenstern, “Wave-function mapping of graphene quantum dots with soft confinement.,” *Physical Review Letters*, vol. 108, pp. 046801+, 2012.

[71] S. Marchini, S. Günther, and J. Wintterlin, “Scanning tunneling microscopy of graphene on Ru(0001),” *Physical Review B*, vol. 76, pp. 075429+, Aug. 2007.

[72] G. Li, A. Luican, and E. Y. Andrei, “Scanning tunneling spectroscopy of graphene on graphite,” *Phys. Rev. Lett.*, vol. 102, p. 176804, Apr 2009.

[73] C. R. Dean, A. F. Young, I. Meric, C. Lee, L. Wang, S. Sorgenfrei, K. Watanabe, T. Taniguchi, P. Kim, K. L. Shepard, and J. Hone, “Boron nitride substrates for high-quality graphene electronics,” *Nature Nanotechnology*, vol. 5, no. 10, pp. 722–726, 2010.

[74] I. Pletikosić, M. Kralj, P. Pervan, R. Brako, J. Coraux, A. T. N’Diaye, C. Busse, and T. Michely, “Dirac Cones and Minigaps for Graphene on Ir(111),” *Physical Review Letters*, vol. 102, pp. 056808+, Feb. 2009.

[75] C.-H. Park, L. Yang, Y.-W. Son, M. Cohen, and S. Louie, “New Generation of Massless Dirac Fermions in Graphene under External Periodic Potentials,” *Physical Review Letters*, vol. 101, pp. 126804+, Sept. 2008.

[76] J. C. Meyer, C. O. Girit, M. F. Crommie, and A. Zettl, “Hydrocarbon lithography on graphene membranes,” *Applied Physics Letters*, vol. 92, no. 12, pp. 123110+, 2008.

[77] R. Bistritzer and A. H. MacDonald, “Moiré butterflies in twisted bilayer graphene,” *Physical Review B*, vol. 84, pp. 035440+, July 2011.

[78] P. Moon and M. Koshino, “Optical properties of the Hofstadter butterfly in the moiré superlattice,” *Physical Review B*, vol. 88, Dec. 2013.

[79] B. Sachs, T. O. Wehling, M. I. Katsnelson, and A. I. Lichtenstein, “Adhesion and electronic structure of graphene on hexagonal boron nitride substrates,” *Physical Review B*, vol. 84, pp. 195414+, Nov. 2011.

[80] R. Martinez-Gordillo, S. Roche, F. Ortmann, and M. Pruneda, “Transport fingerprints at graphene superlattice dirac points induced by a boron nitride substrate,” *Phys. Rev. B*, vol. 89, p. 161401, Apr 2014.

[81] M. Koshino and T. Ando, “Hall plateau diagram for the Hofstadter butterfly energy spectrum,” *Phys. Rev. B*, vol. 73, pp. 155304+, 2006.

[82] D. R. Hofstadter, “Energy levels and wave functions of bloch electrons in rational and irrational magnetic fields,” *Phys. Rev. B*, vol. 14, pp. 2239–2249, Sep 1976.

[83] J. R. Wallbank, A. A. Patel, M. Mucha-Kruczyński, A. K. Geim, and V. I. Fal’ko, “Generic miniband structure of graphene on a hexagonal substrate,” *Phys. Rev. B*, vol. 87, p. 245408, Jun 2013.

[84] C. Faugeras, S. Berciaud, P. Leszczynski, Y. Henni, K. Nogajewski, M. Orlita, T. Taniguchi, K. Watanabe, C. Forsythe, P. Kim, R. Jalil, A. K. Geim, D. M. Basko, and M. Potemski, “Landau level spectroscopy of electron-electron interactions in graphene,” Nov. 2014.

[85] C. Neumann, S. Reichardt, M. Drögeler, B. Terrés, K. Watanabe, T. Taniguchi, B. Beschoten, S. V. Rotkin, and C. Stampfer, “Low B Field Magneto-Phonon Resonances in Single-Layer and Bilayer Graphene,” *Nano Lett.*, Feb. 2015.

[86] M. V. Berry and R. Mondragon, “Neutrino billiard: time-reversal symmetry breaking without magnetic field,” *Proc. R Soc. Lond. A*, vol. 412, p. 53, 1987.

[87] A. F. Young, C. R. Dean, L. Wang, H. Ren, P. Cadden-Zimansky, K. Watanabe, T. Taniguchi, J. Hone, K. L. Shepard, and P. Kim, “Spin and valley quantum Hall ferromagnetism ingraphene,” *Nature Physics*, vol. 8, pp. 550–556, May 2012.

[88] D. A. Abanin, B. E. Feldman, A. Yacoby, and B. I. Halperin, “Fractional and integer quantum Hall effects in the zeroth Landau level in graphene,” *Physical Review B*, vol. 88, Sept. 2013.

[89] K. Nomura and A. H. MacDonald, “Quantum hall ferromagnetism in graphene,” *Phys. Rev. Lett.*, vol. 96, p. 256602, Jun 2006.

[90] J.-N. Fuchs and P. Lederer, “Spontaneous parity breaking of graphene in the quantum hall regime,” *Phys. Rev. Lett.*, vol. 98, p. 016803, Jan 2007.

[91] M. C. Geisler, J. H. Smet, V. Umansky, K. von Klitzing, B. Naundorf, R. Ketzmerick, and H. Schweizer, “Detection of a Landau Band-Coupling-Induced Rearrangement of the Hofstadter Butterfly,” *Physical Review Letters*, vol. 92, pp. 256801+, June 2004.

[92] C.-H. Park, L. Yang, Y.-W. Son, M. L. Cohen, and S. G. Louie, “Anisotropic behaviours of massless Diracfermions in graphene under periodicpotentials,” *Nature Physics*, vol. 4, no. 3, pp. 213–217, 2008.

[93] F. Libisch, S. Rotter, J. Güttinger, C. Stampfer, and J. Burgdörfer, “Transition to Landau levels in graphene quantum dots,” *Phys. Rev. B*, vol. 81, pp. 245411+, 2010.

[94] M. Sadowski, G. Martinez, M. Potemski, C. Berger, and W. de Heer, “Landau level spectroscopy of ultrathin graphite layers,” *Phys. Rev. Lett.*, vol. 97, p. 266405, Dec 2006.

[95] Y. Bychkov and G. Martinez, “Magnetoplasmon excitations in graphene for filling factors $\nu \leq 6$,” *Phys. Rev. B*, vol. 77, p. 125417, Mar 2008.

[96] J. Alicea and M. P. A. Fisher, “Graphene integer quantum hall effect in the ferromagnetic and paramagnetic regimes,” *Phys. Rev. B*, vol. 74, p. 075422, Aug 2006.

[97] H. Haug and S. W. Koch, *Quantum theory of the optical and electronic properties of semiconductors.* World Scientific Publishing Co. Pte. Ltd., Singapore, 3rd edition, 1994.

[98] C. Kallin and B. I. Halperin, “Excitations from a filled landau level in the two-dimensional electron gas,” *Phys. Rev. B*, vol. 30, pp. 5655–5668, Nov 1984.

[99] K. Shizuya, “Many-body corrections to cyclotron resonance in monolayer and bilayer

graphene," *Physical Review B*, vol. 81, Feb. 2010.

[100] L. Yang, M. Cohen, and S. Louie, "Magnetic edge-state excitons in zigzag graphene nanoribbons," *Phys. Rev. Lett.*, vol. 101, p. 186401, Oct 2008.

[101] C. R. Woods, L. Britnell, A. Eckmann, R. S. Ma, J. C. Lu, H. M. Guo, X. Lin, G. L. Yu, Y. Cao, R. V. Gorbachev, A. V. Kretinin, J. Park, L. A. Ponomarenko, M. I. Katsnelson, Y. Gornostyrev, K. Watanabe, T. Taniguchi, C. Casiraghi, H. J. Gao, A. K. Geim, and K. S. Novoselov, "Commensurateincommensurate transition in graphene on hexagonal boron nitride," *Nature Physics*, vol. 10, no. 6, pp. 451–456, 2014.

[102] M. M. van Wijk, A. Schuring, M. I. Katsnelson, and A. Fasolino, "Moiré patterns as a probe of interplanar interactions for graphene on h-bn," *Phys. Rev. Lett.*, vol. 113, p. 135504, Sep 2014.

[103] T. Ribic, "A Density Functional Theory based Tight Binding description of stretched graphene," 2014.

[104] I. Al-Naib, M. Poschmann, and M. M. Dignam, "Optimizing third-harmonic generation at terahertz frequencies in graphene," *Phys. Rev. B*, vol. 91, p. 205407, May 2015.

[105] S. A. Mikhailov and K. Ziegler, "Nonlinear electromagnetic response of graphene: frequency multiplication and the self-consistent-field effects," *Journal of Physics: Condensed Matter*, vol. 20, pp. 384204+, Sept. 2008.

[106] K. L. Ishikawa, "Nonlinear optical response of graphene in time domain," *Physical Review B*, vol. 82, pp. 201402+, 2010.

[107] A. Y. Bykov, T. V. Murzina, M. G. Rybin, and E. D. Obraztsova, "Second harmonic generation in multilayer graphene induced by direct electric current," *Phys. Rev. B*, vol. 85, p. 121413, Mar 2012.

[108] E. Hendry, P. J. Hale, J. Moger, A. K. Savchenko, and S. A. Mikhailov, "Coherent nonlinear optical response of graphene," *Phys. Rev. Lett.*, vol. 105, p. 097401, Aug 2010.

[109] J. Maysonnave, S. Huppert, F. Wang, S. Maero, C. Berger, W. de Heer, T. B. Norris, L. A. De Vaulchier, S. Dhillon, J. Tignon, R. Ferreira, and J. Mangeney, "Terahertz generation by dynamical photon drag effect in graphene excited by femtosecond optical pulses," *Nano Letters*, vol. 14, no. 10, pp. 5797–5802, 2014.

[110] H. A. Hafez, I. Al-Naib, M. M. Dignam, Y. Sekine, K. Oguri, F. m. c. Blanchard, D. G. Cooke, S. Tanaka, F. Komori, H. Hibino, and T. Ozaki, "Nonlinear terahertz field-induced carrier dynamics in photoexcited epitaxial monolayer graphene," *Phys. Rev. B*, vol. 91, p. 035422, Jan 2015.

[111] L. Prechtel, L. Song, D. Schuh, P. Ajayan, W. Wegscheider, and A. Holleitner, "Time-resolved ultrafast photocurrents and terahertz generation in freely suspended graphene," *Natur Communication*, vol. 3, - 2012/01/31/online.

[112] M. J. Paul, Y. C. Chang, Z. J. Thompson, A. Stickel, J. Wardini, H. Choi, E. D. Minot, T. B. Norris, and Y.-S. Lee, "High-field terahertz response of graphene," *New Journal of Physics*, vol. 15, p. 085019, Aug. 2013.

[113] T. T. Luu, M. Garg, Kruchinin, A. Moulet, Hassan, and E. Goulielmakis, "Extreme ultraviolet high-harmonic spectroscopy of solids," *Nature*, vol. 521, no. 7553, pp. 498–502, 2015.

[114] K. L. Ishikawa, "Electronic response of graphene to an ultrashort intense terahertz radiation pulse," *New Journal of Physics*, vol. 15, pp. 055021+, 2013.

[115] C. Zener, "A theory of the electrical breakdown of solid dielectrics," *Proc. R. Soc. Lond., Ser. A*, vol. 145, p. 523, 1934.

[116] D. J. Tannor, *Introduction to quantum mechanics: a time-dependent perspective.* University Science Books, Sausalito, California, 2007.

[117] I. Maeng, S. Lim, S. J. Chae, Y. H. Lee, H. Choi, and J.-H. Son, "Gate-Controlled Nonlinear Conductivity of Dirac Fermion in Graphene Field-Effect Transistors Measured by Terahertz Time-Domain Spectroscopy," *Nano Letters*, vol. 12, pp. 551–555, 2012.

[118] M. M. Glazov and S. D. Ganichev, "High frequency electric field induced nonlinear effects in graphene," *Physics Reports*, vol. 535, pp. 101–138, Feb. 2014.

[119] G. Wachter, S. Sato, C. Lemell, X.-M. Tong, K. Yabana, and J. Burgdrfer, "Controlling ultrafast currents by the non-linear photogalvanic effect," *arXiv:1503.06146*, 2015.

[120] D. Golde, T. Meier, and S. W. Koch, "High harmonics generated in semiconductor nanostructures by the coupled dynamics of optical inter- and intraband excitations," *Phys. Rev. B*, vol. 77, p. 075330, Feb 2008.

[121] G. Vampa, C. R. McDonald, G. Orlando, D. D. Klug, P. B. Corkum, and T. Brabec, "Theoretical analysis of high-harmonic generation in solids," *Phys. Rev. Lett.*, vol. 113, p. 073901, Aug 2014.

[122] G. Vampa, C. R. McDonald, G. Orlando, P. B. Corkum, and T. Brabec, "Semiclassical analysis of high harmonic generation in bulk crystals," *Phys. Rev. B*, vol. 91, p. 064302, Feb 2015.

[123] P. G. Hawkins, M. Y. Ivanov, and V. S. Yakovlev, "Effect of multiple conduction bands on high-harmonic emission from dielectrics," *Phys. Rev. A*, vol. 91, p. 013405, Jan 2015.

[124] S. Ghimire, A. D. DiChiara, E. Sistrunk, G. Ndabashimiye, U. B. Szafruga, A. Mohammad, P. Agostini, L. F. DiMauro, and D. A. Reis, "Generation and propagation of high-order harmonics in crystals," *Phys. Rev. A*, vol. 85, p. 043836, Apr 2012.

[125] T. Higuchi, M. I. Stockman, and P. Hommelhoff, "Strong-field perspective on high-harmonic radiation from bulk solids," *Phys. Rev. Lett.*, vol. 113, p. 213901, Nov 2014.

[126] P. Gibbon, *Short Pulse Laser Interactions with Matter: an introduction.* Imerial College Press, London, 2005.

[127] A. K. Geim and I. V. Grigorieva, "Van der waals heterostructures," *Nature*, vol. 499, no. 7459, pp. 419–425, 2013.

[128] C. Dean, A. F. Young, L. Wang, I. Meric, G. H. Lee, K. Watanabe, T. Taniguchi, K. Shepard, P. Kim, and J. Hone, "Graphene based heterostructures," *Solid State Communications*, vol. 152, no. 15, pp. 1275–1282, 2012.

[129] F. Withers, O. Del Pozo-Zamudio, A. Mishchenko, A. P. Rooney, A. Gholinia, K. Watanabe, T. Taniguchi, S. J. Haigh, A. K. Geim, A. I. Tartakovskii, and K. S. Novoselov, "Light-emitting diodes by band-structure engineering in van der Waals heterostructures," *Nature Materials*, vol. 14, no. 3, pp. 301–306, 2015.

[130] M. Diez, J. Dahlhaus, M. Wimmer, and C. Beenakker, "Emergence of massless dirac fermions in graphene's hofstadter butterfly at switches of the quantum hall phase connectivity," *Phys. Rev. Lett.*, vol. 112, p. 196602, May 2014.

[131] G. Kaiser, *A friendly guide to Wavelets.* Modern Birkhäuser Classics, 2011.

[132] D. Tannor, *Introduction to quantum mechanics. A time-dependent perspective*, vol. 3. University science book, Sausalito, California, 2007.

Acknowledgements

My way to phD is over. It would not have been possible without many people, who I want to acknowledge here. My moving to Vienna and stay in Austria would not have been so smooth without the help and support of my colleges and friends.

First of all, I would like to express my deep gratitude to my thesis advisor Joachim Burgdörfer, who gave me a chance to study physics in his group and who guided me through many hurdles on my way.

Next, I would like to thank my co-advisor Florian Libisch for his patience and encouragement on my work. His enthusiasm and assistance helped me a lot to overcome all the difficulties I experienced in my phD research.

I would like to offer my special thanks to Stefan Rotter, who gave me an opportunity to investigate the interesting phenomena of nonlinear dynamics of ultracold neutrons. This project won me a project student Gregor Wautischer, who was asking difficult questions.

I am deeply grateful to Christoph Stampfer and Bernat Terrés for many discussions leading us to a deeper knowledge and understanding of several experiments. Their comments and suggestions were invaluable.

I owe a very important debt to Mikhail Katsnelson, who agreed to review my thesis and to be my examiner at the thesis defense.

I would also like to express my gratitude to TU Wien (DK-CMS) and FWF (DK-Solids4Fun) for their financial support.

My moving to Austria would not have been possible without a support from my closest friends in Russia: Tanya R., Ira K., Lena D., Dasha E., Nadya K., Maxim K., and Sergey K. I heartily thank my former advisor Alexander Malyshev from the NNSU for the interesting discussions.

I would like to thank all my friends and colleges in Austria. Especially, my bureau mate Renate P. and my group colleges. I have greatly benefited from the Doctorate school Solids4Fun, where I met a lot of young and motivated scientists. Their feedback on my work and the discussions of their projects helped to boost my knowledge of different scientific topics.

I also owe special thanks to Sandro M. and friends who enjoy playing jazz with me in Big Peter's Band and in APB. I am proud of the APB music project and acknowledge the contributing musicians (mostly physicists): Florian A., Georg W., Shuhei Y. and Markus O.

Finally, I would like to thank my parents, Paul and Paul's family who showered me with their love and support at every step of my way.